Research Performance Progress Report (RPPR) – Final Scientific/Technical Report

Project Title: Investigation of Gas Solid Fluidized Bed Dynamics with Non-Spherical Particles

Grant No: DE-FE0003742

Agency: National Energy Technology Laboratory, Department of Energy

DOE Project Manager:
Robie Lewis
Project Manager (Capture Work)
National Energy Technology Laboratory
3610 Collins Ferry Road
P.O. Box 880
Morgantown, WV 26507-0880
304-285-4445
robie.lewis@netl.doe.gov

Project Period: 07/01/10 - 06/30/13

Reporting Period: 30-SEP-13
Reporting Frequency: Final – One Time

Principal Investigator:
Ahsan R. Choudhuri, PhD
Professor and Chair, Department of Mechanical Engineering
Director, Center for Space Exploration Technology Research
The University of Texas at El Paso
500 W. University, ENG. Annex Suite A126
El Paso, TX 79968
Tel: 915 747 6905 Fax: 915 747 5019
E-mail: ahsan@utep.edu

Signature of Submitting Official: ______________________________.

Submitting Institution: The University of Texas at El Paso
DUNS: 132051285

Submission Date: 09/30/13

Disclaimer:

Abstract

One of the largest challenges for 21^{st} century is to fulfill global energy demand while also reducing detrimental impacts of energy generation and use on the environment. Gasification is a promising technology to meet the requirement of reduced emissions without compromising performance. Coal gasification is not an incinerating process; rather than burning coal completely a partial combustion takes place in the presence of steam and limited amounts of oxygen. In this controlled environment, a chemical reaction takes place to produce a mixture of clean synthetic gas. Gas-solid fluidized bed is one such type of gasification technology. During gasification, the mixing behavior of solid (coal) and gas and their flow patterns can be very complicated to understand. Many attempts have taken place in laboratory scale to understand bed hydrodynamics with spherical particles though in actual applications with coal, the particles are non-spherical.

This issue drove the documented attempt presented here to investigate fluidized bed behavior using different ranges of non-spherical particles, as well as spherical. For this investigation, various parameters are controlled that included particle size, bed height, bed diameter and particle shape. Particles ranged from 355 µm to 1180 µm, bed diameter varied from 2 cm to 7 cm, two fluidized beds with diameters of 3.4 cm and 12.4 cm, for the spherical and non-spherical shaped particles that were taken into consideration. Pressure drop was measured with increasing superficial gas velocity. The velocity required in order to start to fluidize the particle is called the minimum fluidization velocity, which is one of the most important parameters to design and optimize within a gas-solid fluidized bed. This minimum fluidization velocity was monitored during investigation while observing variables factors and their effect on this velocity. From our investigation, it has been found that minimum fluidization velocity is independent of bed height for both spherical and non-spherical particles. Further, it decrease with decreasing particle size and decreases with decreasing bed diameter. Shadow sizing, a non-intrusive imaging and diagnostic technology, was also used to visualize flow fields inside fluidized beds for both spherical and non-spherical particles and to detect the particle sizes.

Table of Contents

List of Tables

List of Figures

Chapter 1: Introduction

1.1 OVERVIEW

For a long period of time liquid and gaseous fuels played an important role on worldwide industrial and technological development. Research and development is also going on other alternative energy source like coal and other solid fuels combustion (1). Where our modern life is fully depending on energy, it is mandatory to produce clean and climate friendly energy technology. Combustion of coal generally exposes its constituents like sulfur, nitrogen, carbon to oxidation processes and leads to unwanted pollutant emissions. Producing necessary energy and at the same time reducing unwanted pollutant emissions is the biggest energy challenge for the 21st century. Coal gasification is a promising technology that can produce energy and reduce some emissions without sacrificing its performance. Fluidized bed technology is one method to convert coal or other feedstock into synthetic gas (CO-H2). This method breaks the solid fuel down at the molecular level and removes impurities and ash. The U.S. Department of Energy is emphasizing coal gasification with enhanced reliability and efficiency (2). Significant development in coal burning technology, such as fluidized beds, has been observed in the last quarter century. In many cases, the most popular choice of fluidization, particularly with coal particles, is gas-solid fluidization. Flow pattern and solid mixing in fluidized beds are an important design parameter. Moreover multiple scales with interaction gas-solid phase fluidized beds are difficult to access (3). The characterization of the fluidized bed's minimum fluidization velocity is of critical importance and as such, many factors influencing minimum fluidization velocity are described in literature review section that follows.

Experimental data is required to get detail information of gas-solid fluidized bed behavior. To understand gas-solid fluidized bed behavior, this effort constructed a laboratory scale fluidized bed. Borosilicate gas beads were used as test particles and a supply of air to test particles served as gasifying agent. Different particle size ranges and different shapes were used to observe effect of particle size and shape. Pressure drop measurements with increasing superficial gas velocity were the experimental data points to investigate fluidized bed behavior. High speed imaging and shadow sizing technology was also used to observe flow field inside fluidized bed. Shadow sizing technology is a non-intrusive method to visualize flow field and it can also detect the particle size and particles velocity over size.

1.2 RESEARCH OBJECTIVES

The purpose of this study is to investigate fluidized bed behavior with different variables parameter and then investigate effects on key design parameters. Minimum fluidization velocity is one of the main design factors of a fluidized bed that is affected by changing different parameters, e.g. particle size, shape, bed height, bed diameter. This report outlines the following objectives:

1) Hydrodynamic behavior of fluidized bed with spherical and non-spherical particles
2) Flow field visualization for spherical and non-spherical particles using a non-intrusive imaging and diagnostic technology
3) Numerically model the minimum fluidization velocities, drag, particle, and fluid flows of non-spherical particles in the fluidized bed, based on the experimental work via the determination of drag force FD =f (CD, Re, Q, ρg, ρs, ϕ, etc.) using multiphase computational code MFIX.

1.3 REPORT ORGANIZATION

Chapter 1 summarizes the importance of coal gasification and one coal gasification via the method of fluidized bed. Research objectives and available facilities are also described in this chapter. Chapter 2 summarizes the literature review regarding available gasification technologies, their uses, and different types of fluidized beds, which includes different types of particle densities, sizes, shapes and bed diameters. Chapter 3 describes the experimental setup, design parameters, particles selection and production method, the test matrices, experimental measurement methods and technical considerations to compare theoretical findings and experimental results. Chapter 4 provides the experimental results, a discussion about findings and a comparison with theoretical explanation. Lastly, chapter 5 summarizes the experimental findings with conclusions about our research and recommended future efforts.

1.4 FACILITIES

All the analysis and experimental testing were performed in Center for Space Exploration Technology Research (cSETR) laboratory in Mechanical Engineering Department at The University of Texas at El Paso (UTEP). The lab is fully equipped with wide range of instruments with 5 HP blower, hydraulic compressor, high speed camera, sieve shaker, microscopic camera, flow meter, differential manometer etc. to perform experimental measurement.

Chapter 2: Literature Review

2.1 GASIFICATION

Gasification is a technology that converts carbonaceous materials into synthetic gas. Within this process, low value feedstock (carbonaceous materials) turns into a high value product (synthetic gas). In a chemical reactor, the carbonaceous materials are subjected to limited amounts of steam and oxygen. With this controlled environment a chemical reaction takes place to produce a mixture of gas containing carbon monoxide (CO), hydrogen (H_2) and other gaseous compounds. This mixture of gas is termed "Synthetic Gas". Although synthetic gas has lower heating value than natural gas, it can still be used for high-efficiency combined cycle electric power plants or to make many products presently made from natural gas, e.g. ammonia fertilizer, methanol derived chemicals. (3)

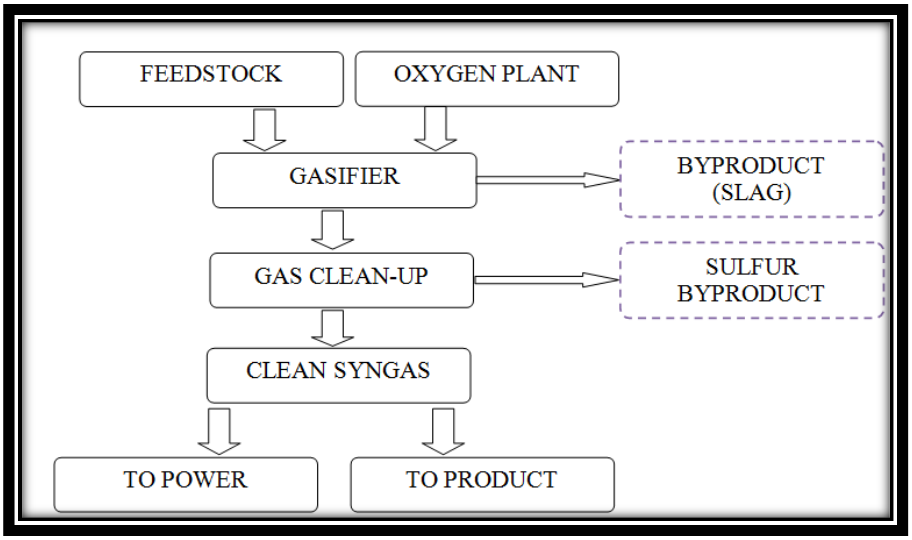

Figure 2.1: The Gasification Process

Figure 2.1 shows the steps of the gasification process. For gasifiers, a wide range of feedstock can be used that includes coal, oil refineries liquid residuals and waste of chemical plants and biomass. Gaseous and liquid feedstock feed into gasifier directly and on the other hand solid feedstock breaks down into very small particles and then feed into gasifier. Glass like byproduct slag produced from solid and liquid feed gasifier is non-hazardous. Slag can be used in road construction and for roofing materials. From most gasification plants, 99% of sulfur is removed and recovered as elemental sulfur or sulfuric acid. Sulfur, mercury, uncovered carbon, trace minerals, particulates are removed by processes common to the chemical and refining industries. Finally, clean syngas is combusted into high-efficient combined cycle electric power plants to make products like substitute natural gas, chemicals, fertilizers, transportation fuels and hydrogen. (4)

2.1.1 Combustion vs. Gasification

Combustion is a complete oxidation process to produce thermal energy. The hazardous byproducts produce for complete combustion or burning of coal. Solid wastes, NOx, SO_2, and CO_2 have the most detrimental impact on our environment. Furthermore, burning coal is dirty, while controlling and capturing of CO_2 is difficult.

On the other hand gasification is called partial oxidation. Gasification process burns the carbonaceous materials partially instead of burning it completely. This process converts carbonaceous materials into synthetic gas, which can be used to produce electricity and high value products that include fertilizers, chemicals, hydrogen and transportation fuels. Furthermore, it produces non-hazardous byproducts and low emissions. (5)

2.1.2 Chemistry in Gasification

The carbonaceous materials go through different processes during gasification in a gasifier. The chemical reaction takes place with help of steam and limited amount of oxygen. When feedstock feeds into gasifier dehydration process occurs at temperature reaches up to 100^0 C. At this point the moisture contents from feedstock drives out in the form of gas. When temperature goes up to 200-300^0C pyrolysis or devolatilization process occurs. As temperature increases the feedstock goes through decomposition process and release volatiles contents in the form of gas.. At this point feedstock (for coal) losses its weight up to 70% due to release of volatile contents and the remaining is called char. Volatile contents are tars, H_2, CH_4. (6)

The released gas form has higher sulfur, hydrogen and oxygen contents than feedstock. On the other hand remaining char is mixture of carbon-rich organics.

Released volatile contents and remaining char react with oxygen to produce carbon dioxide (CO_2) and heat. This continuous generation of heat energy is required for pyrolysis and gasification reactions further. (6)

The basic reactions are

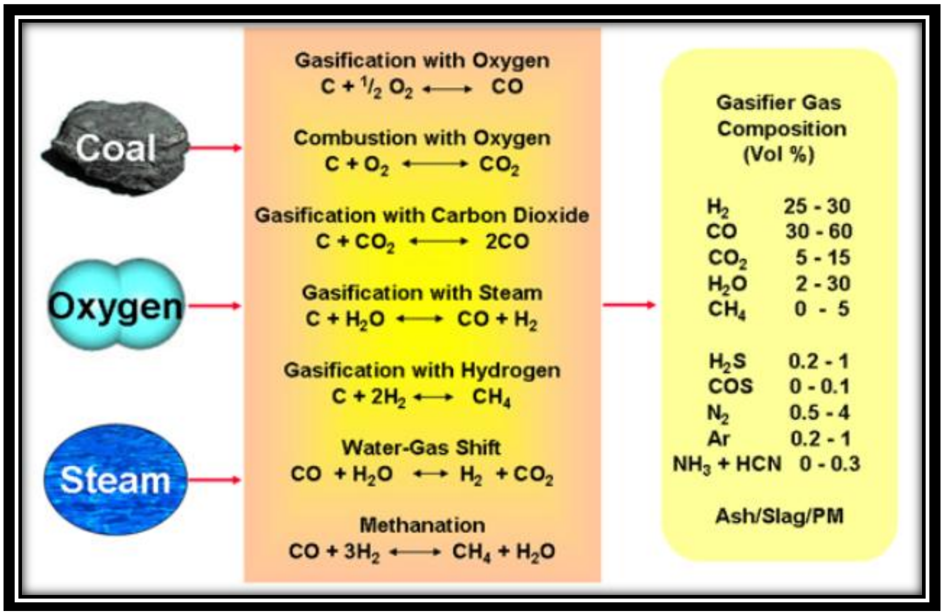

Figure 2.2: Gasification Reactions (7)

2.1.3 History of Gasification

In early-1800s gasification technology was invented but in last 50 years it has gone rapid transformation. Rapid changes of gasification can be categorized into following five stages. (3)

1850-1940: Before the development of natural gas all gas for fuel and light were produced by gasification of coal. This gas was called ‘Town Gas’.

1940-1975: During World War II gasification technology was used to produce synthetic gas by German Engineers. Later this technology was exported to South Africa (1950) where it was developed further to produce chemicals and liquid fuels.

1975-1990: For pursuing energy crisis the U.S. government started financial support for several proof-of concept gasification projects like Integrated Gasification Combined Cycle (IGCC) electric power plant.

1990-2000: At this stage government agencies of United States and Europe started providing financial support for four medium sized (≈ 250MWe) projects to demonstrate the feasibility of IGCC process.

2000-present: New IGCC power plants started by commercial developers without government subsidies. These new facilities are adjacent to refineries where hydrocarbons and petroleum coke are available.

2.2 GASIFICATION TECHNOLOGIES

Gasification technologies can be sorted into three general categories depending on flow of the gasifying agents, namely Fixed or Moving Bed Gasifiers, Entrained Bed, and Fluidized Bed.

2.2.1 Fixed or Moving Bed Gasifiers

Figure 2.3 shows a diagram of a generic moving bed. In moving beds, feedstock and gasifying agents interact with counter flow. Feedstock feeds from the top of the bed and steam/oxygen are introduced from the bottom of the bed. Before using feedstock they are made into coarse particles for better permeability and to avoid excess pressure drop and chemical burning. As the feedstock moves down, it goes through a different gasification stage, leaving only syngas and a dry or molten ash. Ash goes out from the bottom of bed. Movieng bed runs in dry-ash mode and in slugging mode. In dry-ash mode temperature is controlled under ash slagging tempureature with excess steam. Excess steam cooled the ash and make solid ash. On the other hand in slagging mode less steam is provided to get higher temperature. This high temperature melts the ash and produce solid slag (8)

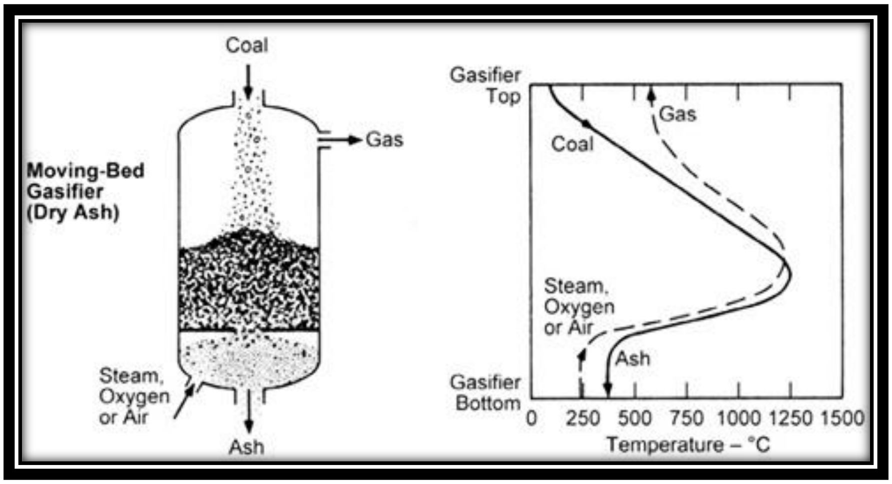

Figure 2.3: Moving Bed Gasifier (8)

2.2.2 Entrained Bed

With this type of bed, feedstock and gasifying agents are fed together from the top of bed.

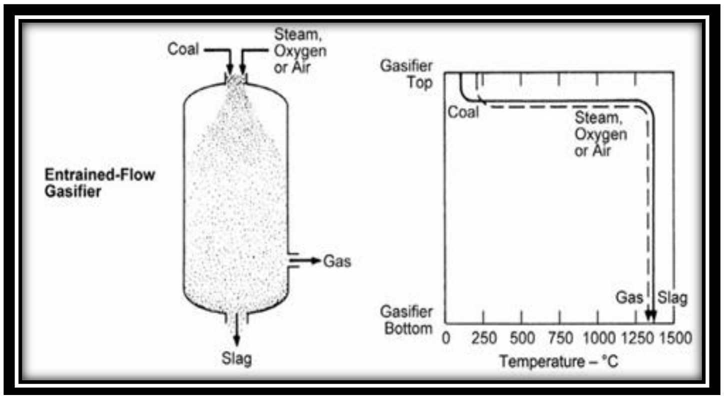

Figure 2.4: Entrained Flow Gasifier (9)

Feedstock and gasifying agents move in the same direction and the gasifying agent surrounds the coal particles as they flow and pass different stages of gasification. This type of bed is operated at high temperatures to melt the ash into slag. Furthermore entrained beds can use dry or wet feedstock. They can handle nearly any coal feedstock and can produce more tar free, clean syngas than other forms (9).

2.2.3 Fluidized Bed

In this type of bed, high velocity upward flow of gasifying agents are introduced to the feedstock. Upward flow makes the feedstock suspend and various stages of gasification then take place. This type of bed provides back mixing and mixes the new feed coal with undergoing gasification coal. Less than 6 mm particle size used to maintain suspension of particles into the bed. It operates at significant high temperature for acceptable carbon conversion rate but less than ash fusion temperature to avoid clinker and de-fluidization of bed. This type of gasifier is suitable for coal and other type of fuel like biomass (10).

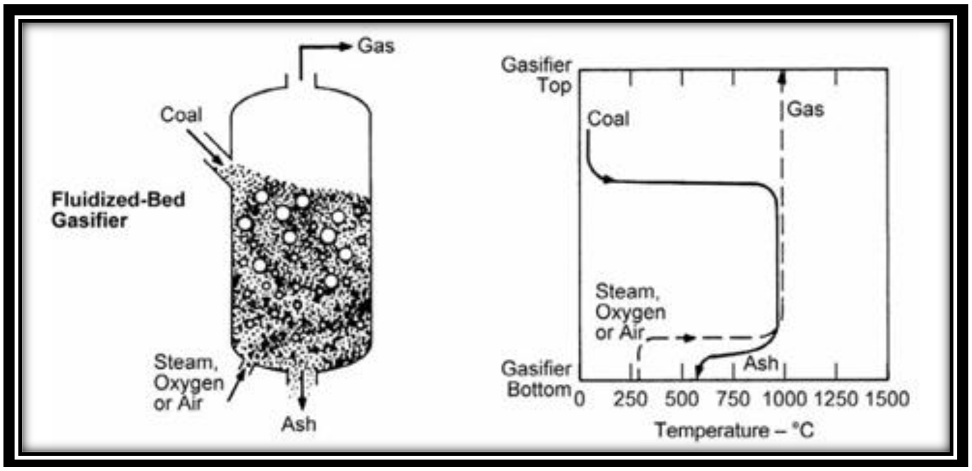

Figure 2.5: Fluidized Bed (10)

2.3 MULTIPHASE FLOW

Generally, a phase is identified by solid, liquid or gaseous state. A flow is referred to as a multiphase flow when the flow contains mixture of two or more of the identified phases with different volume fraction. Disperse flows and Separated flows are two identified topologies of multiphase flow. Dispersed flow contains discrete elements distributed as a connected volume in a continuous phase like bubbles in liquid and droplets in gas. Separated flows contain two or more phases of different fluid separated by a line of contact. (11)

2.3.1 Types of Multiphase Flow

Most widely used multiphase flows are two-phase flows: Gas-liquid flows, liquid-solid flow, gas-solid flows. **Gas-liquid flows** contain gas bubbles in liquid flow or liquid droplets in gaseous flow. Process industries are often interested in using this type of flow. Formation of droplets of combustible liquid fuel is very important for internal combustion engines, spray formation with droplets for processing materials and this flow is often used in heat exchange applications. **Liquid-solid flows** contain solid particles in liquid phase, also called slurry flows. This type of flow is mainly used for transportation of solid particles. **Gas-solid Flows** contain suspended solid particles via gas buoyancy. Gasification is a perfect example of gas-solid flows. In fossil fuel power plants, the combustion of coal depends on coal particle burning and suspension of coal particles via gasifying agents. Cyclone separator and electrostatic precipitators also use the principle of gas-solid flow. Moreover, gas-solid flows are also used for pneumatic transportation. (11)

2.4 FLUIDIZED BED REACTORS

In modern society most of our energy comes from the source of carbonaceous fuel. This carbonaceous fuel can be found in solid form or in liquid form which required more processing than natural gas considering environmental impact. Fluidized bed reactors are simple chemical reactor for combustion, heat transfer process, steam generation, power plant and chemical synreport. Moreover, this technology is really a breakthrough technology that can reduce significant amount of emission after partially burning carbonaceous fuels. Coal and biomass are the major source of carbonaceous fuels. Because of effectiveness of this technology concerning about environmental issue currently a great industrial interest has been found. (12)

Based on flow behavior of carbonaceous particles and gasifying agent fluidized bed reactor can be classified within the following types: (13)

Stationary or Bubbling Fluidized Beds: these beds run with low gas velocity attempting to balance the weight of particles. At this point, particles suspend on the gasifying agent as their weight is balanced by low gas velocity. The particles behave like boiling liquid depending on certain particle characteristics like size and density. Particles remain on the surface except some fine particles that entrained.

Vibratory Fluidized Bed is like a stationary fluidized bed that includes an external source of vibration introduced for better excitement and improving mixing properties of particles and a gasifying agent.

Circulating Fluidized Beds run with relatively high velocities that expand the solid particles beyond their suspension. High velocity particles from bed are separated from gas by cyclone separators and re-enter the bed closed loop. Moreover, an internal circulation also takes place for those particles that are not entrained out from the bed with high velocity.

Transport or Flash Reactor Bed with higher gas velocity than the circulating fluidized bed. Velocity difference of gas and particle decreased more than the circulating fluidized bed. Particle velocity reaches near the velocity of gas. Only some selected application used this reactor where solid retention times are significantly sufficient.

In Annular Fluidized Beds a central nozzle is introduced at the middle of bed with additional gasifying agents. A good intense mixing zone achieved above the nozzle compare to external loop of circulating fluidized bed. Moreover, annular fluidized bed can be connected with other fluidized bed.

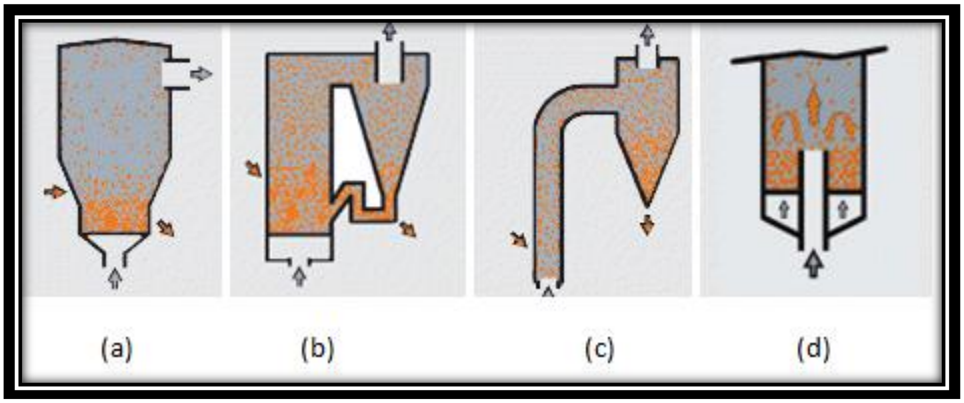

Figure 2.6: (a) Bubbling Bed (b) Circulating Bed (c) Transport Bed (d) Annular Bed (13)

2.4.1 Gas-Solid Fluidization

Gas-solid fluidization follows a simple principle. Upward flow of gasifying agent (steam/air) introduced into a packed solid bed. As a result a pressure drop occurs within the bed. This pressure drop goes as high as equal to weight of the solid particles. Characteristics of fluidization depend on different factors. Properties of solid particle are the important factor on which behavior of fluidization depends. Fluidization behavior also depends on solid particle size, particle density, their cohesiveness etc. In 1973 Geldart suggested four classified types of particles range as follows (based on density and size) depending on what fluidization behavior can be categorized. (14)

Group A composed with small particle size with low density less than 1400 kg/m^3. Bubbles appear after the minimum fluidization velocity and also the bed expand after minimum fluidization velocity. A smooth fluidization occurs with low velocity. Cracking catalyst powder is in group A.

Group B composed with particle size range between 40 μm to 500 μm and density between 1400 kg/m^3 to 4000 kg/m^3. Bubbling appears at minimum fluidization velocity and these bubbles do not depend on particle size. Sand like powder is in group B.

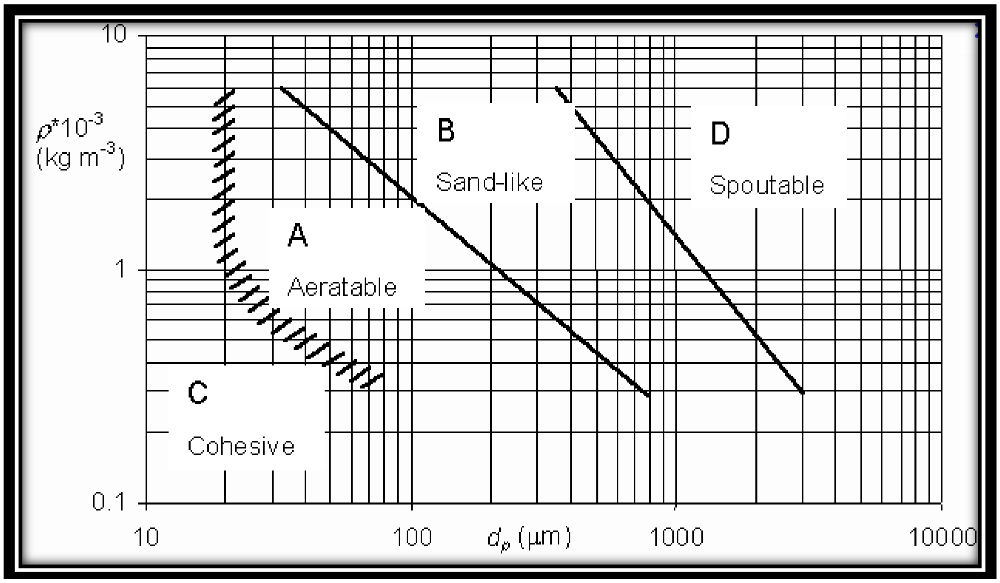

Figure 2.7: Geldart's Classification of Powder according to fluidization properties.

Group C composed with all cohesive powder. Particles of this group are extremely fine and very much difficult to fluidize because there highly cohesive property. To fluidize the group C particles it is recommended to use stirrers or vibration to break the inter-particle forces. Flour, cement are example of this group.

Group D composed with relatively large or dense particles and easily spout. During fluidization large bubble or channeling occurs for this group of particles.

2.4.2. Fluidization Regimes

There are at least five fluidization states have found in gas-solid flow. The transition of these different fluidization regimes depends on gas-solid system properties. All fluidization regimes can be categories into two sections – particulate (smooth) and aggregative (bubbling).

Before particulate fluidization the particles are fixed until minimum fluidization. The superficial gas velocity (u) is less than minimum fluidization velocity ($0 \leq u < u_{mf}$ (minimum fluidization velocity). This state is referred as fixed bed.

When superficial gas velocity reaches up to minimum fluidization velocity (u_{mf}) the fixed bed begins expand smoothly with low pressure fluctuation. At this point small-scale of particles motion and tendency to aggregate observed. This state is referred as particulate fluidization where $u_{mf} \leq u < u_{mb}$ (superficial velocity at onset of bubbling). It is also called homogeneous fluidization.

From the point of onset bubbling fluidization bubble appears near at distributor. These bubbles coalescence and rise to top of the bed surface. The top surface is well identified as the bubbles break at top surface. In bubbling fluidization pressure fluctuation is irregular and at this point superficial gas velocity is between $u_{mb} \leq u < u_{ms}$ (slugging velocity)

For increase of superficial gas velocity after bubbling fluidization the bubbles mostly fill the bed column and rises the top surface with collapse of large bubbles. This state is referred as slugging fluidization and gas velocity is between $u_{ms} \leq u < u_k$ (velocity at transition to turbulent regimes).

At turbulent regimes the particles cluster moves and fro to with low amplitude pressure fluctuation and top surface can barely identified. At this point the gas velocity is between $u_k \leq u < u_{tr}$ (vertical transport velocity)

In fast fluidization particles transport from top of the bed column and there is no upper bed surface. The bed getting empty for transport of particles and should add more particles by near bottom of the bed.

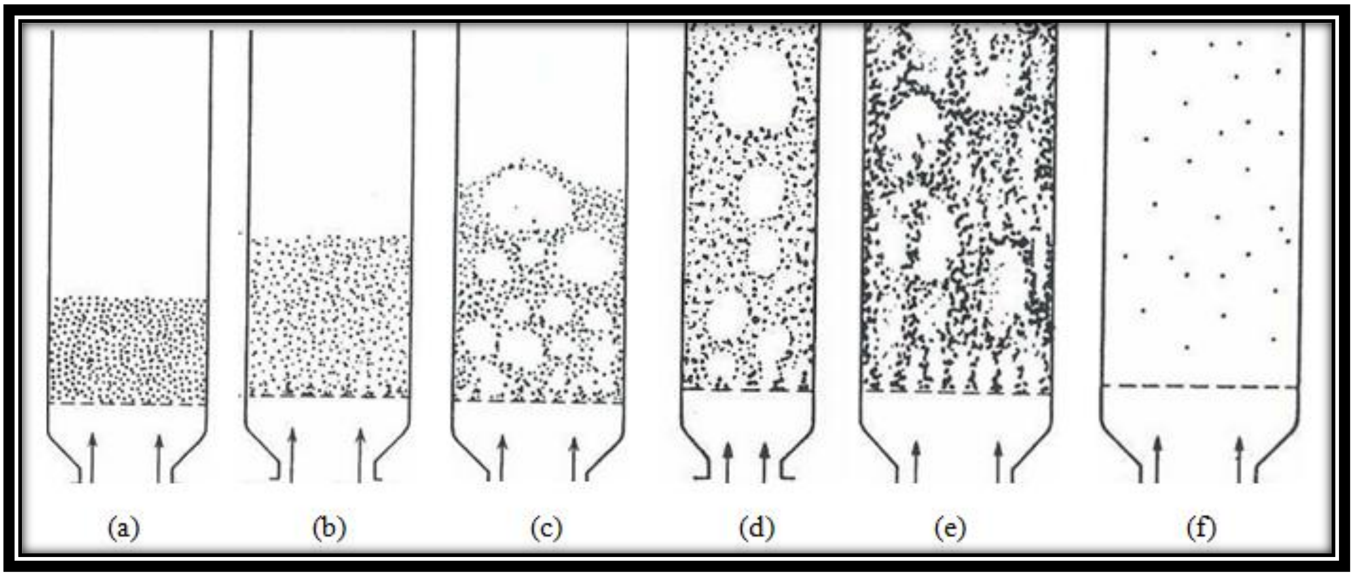

Figure 2.8: (a) Fixed Bed (b) Particulate Fluidization (c) Bubbling Fluidization (d) Slugging Fluidization (e) Turbulent Fluidization (f) Fast Fluidization

All the above fluidization regimes do not happened for any particular fluidized bed because transition point depends on different features. Minimum fluidization and bubbling velocity depends on gas-solid properties. Slugging velocity depends on bed height and bed column diameter and turbulent velocity depends on feeding rate of particles to the bed. (15)

2.5 GAS-SOLID FLUIDIZED BED CHARACTERISTICS

Petroleum industries make extensive use of fluidization, for instance when applied to gas-solid reactions, catalytic processes, and acrylonitrile synreport. As with previous, pressure drops and minimum fluidization velocity are the most important parameters to characterize the gas-solid fluidized bed.

2.5.1 Pressure Drop

Typically a fluidized bed filled with small solid particles. Flow of gasifying agent passes through the packed bed and the gas flow experienced a resistance. This resistance is the resultant of drag force exerted by the solid particles in bed. For passing the flow at a specified flow rate through bed for proper mixing both gas and solid phase a pressure drop is required. This pressure drop through bed is commonly measured from the total drag force exerted by the solid particles. (16)

To measure the bed pressure drop Sabri Ergun in 1952 expressed bed frictional factor as a function of Reynolds number. (17)

$$f_p = \frac{150}{R_e} + 1.75 \qquad (1)$$

Where,

$$f_p = \left(\frac{\Delta P}{L}\right)\left(\frac{Dp}{\rho {V_s}^2}\right)\left(\frac{\varepsilon^3}{1-\varepsilon}\right) \qquad (2)$$

$$R_e = \frac{D_p\, V_s \rho}{(1-\epsilon)\mu} \qquad (3)$$

Here,

$\Delta P = Pressure\ Drop$

$L = Length\ of\ the\ Bed$

$D_p = Diameter\ for\ spherical\ particles$

$\rho = Fluid\ density$

$\mu = Dynamic\ Viscosity\ of\ Fluid$

$\varepsilon = Void\ Fraction$

$V_S = Superfical\ Gas\ Velocity$

Putting the value of frictional factor and Reynolds number from equation (2) and (3) in equation (1), the bed pressure drop comes as follows,

$$\Delta P = \frac{150(1-\varepsilon)^2\mu}{{D_p}^2\varepsilon^3} L V_S + \frac{1.75\rho(1-\varepsilon)}{D_p\varepsilon^3} L {V_S}^2 \qquad (4)$$

Changing in pressure drop in equation (4) is subjected to solid particles equivalent diameter (D_P) and void fraction of the bed (ϵ).

On the other hand, Ergun equation (equation 4) is not straight forward for non-spherical particles. In equation 4, D_p is the diameter of spherical particles which is straight forward. But for non-spherical particles, their equivalent diameter was used where$D_{eq} = \varphi \times D_{sd}$. Here D_{sd} is the Sauter-mean diameter (18). For non-spherical particles the bed pressure drop equation will be,

$$\Delta \mathrm{P} = \frac{150(1-\varepsilon)^2 \mu}{\mathrm{D}_{eq}{}^2 \varepsilon^3} \mathrm{L} V_S + \frac{1.75\rho(1-\varepsilon)}{D_{eq}\varepsilon^3} \mathrm{L} V_s{}^2 \tag{5}$$

2.5.2 Minimum Fluidization Velocity

At the onset of fluidization or minimum fluidization velocity the upward force by flow is equal to the gravitational force exerted by bed particles. In other way, pressure drop across bed is equal to total weight of bed particle per unit area of cross section. (16)

Minimum fluidization velocity can be calculated by balancing net weight of bed particle by upward flow force of gasifying agent.

Upward force = $\Delta P \times A$

For a fixed bed height (L) with void fraction (ϵ), volume of particles = $(1-\epsilon)A \times L$

Net weight of particles = $(1-\epsilon) \times (\rho_p - \rho_f)A \times L \times g$

Here,

ρ_p, ρ_f, g are density of particles, gasifying agent and gravitational force respectively.

By balancing net weight of particles and upward force

$\Delta P = (1-\epsilon) \times (\rho_p - \rho_f)L \times g$

Using the value of pressure drop ΔP in equation (4)

$$1.75 D_p \rho_f V_{mf}{}^2 + 150(1-\varepsilon)\mu V_{mf} = (\rho_p - \rho_t) D_p{}^2 g \varepsilon^3 \tag{5}$$

At the balancing point of total bed weight and upward force the superficial gas velocity (V_s) is referred as minimum fluidization velocity (V_{mf}).

2.5.3 Void Fraction

Packing characteristics are required to understand the design and operation of a packed bed. During our experiment the bed is made densely packed. After pouring the particles into the bed and shaking it for several minutes the bed is made densely packed. Several authors ranged the voidage 0.37 to 0.39 for dense packed bed of monosized spherical particles (12).

For complexity of defining the voidage for non-spherical particles, very little theoretical and experimental work has been performed. It is suggested by Brown in 1966 (12), packing void fraction depends on particles sphericity and based on experiment it has shown the voidage can relate to the sphericity as below table.

Table 2.1: Voidage of Randomly Packed Beds with uniformly sized Particles Larger than 500 µm. (Packing of Non-Spherical particles) (12)

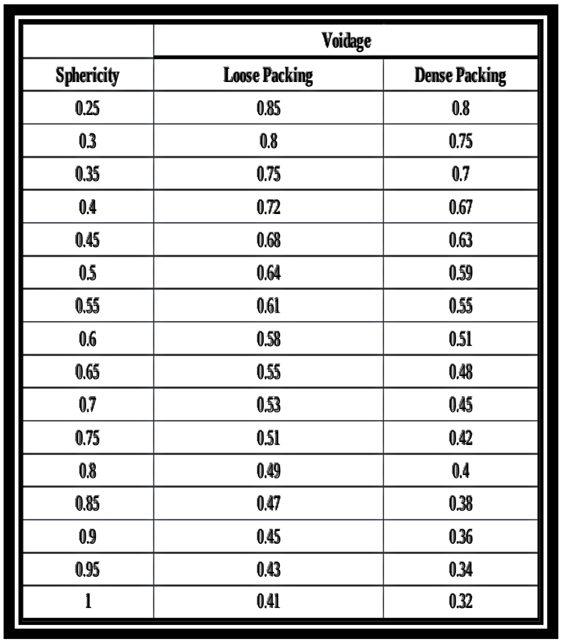

	Voidage	
Sphericity	Loose Packing	Dense Packing
0.25	0.85	0.8
0.3	0.8	0.75
0.35	0.75	0.7
0.4	0.72	0.67
0.45	0.68	0.63
0.5	0.64	0.59
0.55	0.61	0.55
0.6	0.58	0.51
0.65	0.55	0.48
0.7	0.53	0.45
0.75	0.51	0.42
0.8	0.49	0.4
0.85	0.47	0.38
0.9	0.45	0.36
0.95	0.43	0.34
1	0.41	0.32

2.5.4 Hydrodynamics Behavior of Fluidized Bed

Operation of fluidized beds has many applications in industry and for this reason many references have been found in literature. In industrial applications, bed diameter, particles size, particles shapes, bed height play very important parts. Many works based on particles size, bed diameter, bed height, particles shape exist in literature. In a cylindrical shape fluidized bed, the effect of particles diameter and bed height on minimum fluidization velocity was investigated by Gunn et al. (19). They found no significant effect on minimum fluidization velocity for bed height. Both rectangular bed (2D) and cylindrical bed (3D) was used by Geldart el al. ((20). Six different bed heights were used for both 2D and 3D fluidized bed and it has been found that there is no effect on minimum fluidization velocity on increasing bed height for cylindrical fluidized bed. On the other hand, minimum fluidization velocity increased for increased bed height for rectangular shape fluidized bed.

Two fluidized bed with different diameter size (0.29 m and 0.089 m) were investigated by Hilal et al. (21) and they found decreased minimum fluidization velocity with increased bed diameter. A rectangular fluidized bed with 1×0.2×0.012 m dimension and a range of particles from 160-700 µm was used by Ramos el al. (22). They used different bed height and bed widths and concluded their investigation that minimum fluidization velocity decrease with increased bed width and increase with increased bed height and particles diameter. Geldart Type-D particles were used with different bed height in a 300×300 mm shape rectangular fluidized bed by Zhong el al. (23). They also concluded increasing minimum fluidization velocity with increasing 2D bed size. A conical tapered fluidized bed with various bed heights was investigated by Sau et al. (24). Their investigation found no significant effect on minimum fluidization velocity with increasing bed height for tapered fluidized bed but minimum fluidization velocity increase with increasing tapered angle. Zhon et al. (25) investigated a 0.4×0.4 m rectangular bed with chips, mung, beans, millet, corn stalks and cotton stalks to study the effect of particles size, shape and density on minimum fluidization velocity. Their investigation concluded increasing minimum fluidization velocities with increasing length to diameter ratio of fluidized bed. Two fluidized bed column with 1.6 and 2.4 cm diameter were investigated by Rao et al. (26). Glass beads (100-600µm) with 2500 kg/m^3 and polystyrene beads (250-354µm) with 1250 kg/m^3 were used in their investigation. They found in their investigation that minimum fluidization velocity influenced by bed height and bed diameter. The effect of bed height and material density on minimum fluidization velocity in a cylindrical bed with glass beads, ground corncob and ground walnut shells at different bed heights was investigated by Escudero et al. (27). Their investigation found that each type of particle has no influence in minimum fluidization velocity with increasing height and minimum fluidization velocity influenced by particles density. It increases with increase of particle density.

Chapter 3: Experimental Setup & Technical Approach

This section describes the laboratory scale fluidized bed system with different apparatus used to study the hydrodynamics of gas-solid fluidized bed system. Experimental procedure, technical approach and theoretical considerations are also presented in this chapter. Section 3.1 describes the design parameter of 12.4 cm diameter fluidized bed reactor and air supply, control procedure. Section 3.2 describe about test particles selection, preparation and different parameter of particles. Section 3.3 describes about experimental measurement procedures.

3.1 EXPERIMENTAL SETUP

Figure 3.1 is the diagram of our laboratory scale fluidized bed. From the figure, one can note the high-pressure blower with 3730 KW and 34 m^3/min flow rate has been used to supply the gasifying agent (air) to the test section. The air was supplied to the test section by 300 cm long and 12.7 m diameter sheet metal pipe with three elbows.

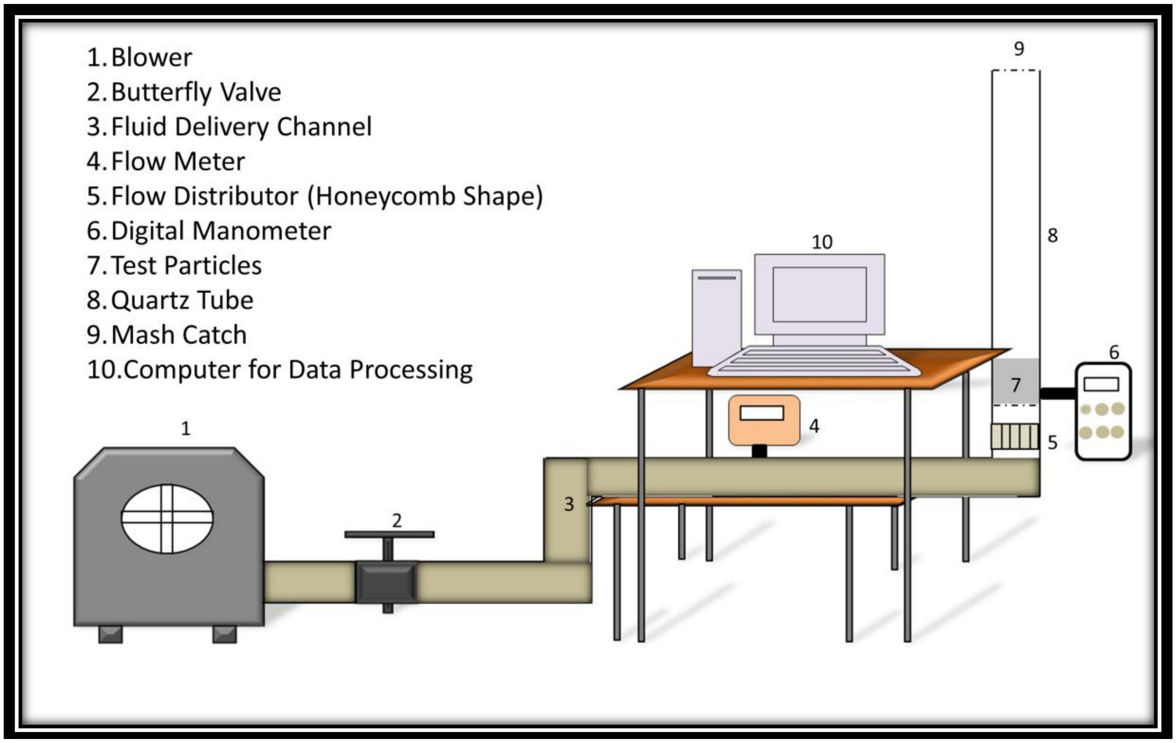

Figure 3.1: Schematic Diagram of Laboratory Scale Fluidized Bed

This length of pipe and elbows were used to allow for the flow measurement as was recommended by the flow meter manufacturer to get the proper flow rate reading through the cross section of sheet metal pipe. The blower has a rectangular shaped outlet. For this reason, a duct reducer with 12.7 × 17.8 cm rectangular to 10.2 cm circular duct was used and connected from blower outlet to sheet metal pipe inlet.

To control the flow rate to the test section a wafer style butterfly valve with 12.7 cm diameter and 5.7 cm thickness was used and connected between the blower and first elbow among three. This butterfly control valve was rated for 200 PSI. For measuring flow rate across the bed a thermal mass flow meter was used between second and third elbow. Distance between elbows and flow meter was maintained as flow meter manufacturer requirement.

The bottom part of test section was by made of plexi glass tube with 12.7 cm outer diameter and 3.18 m wall thickness. Also a quartz tube with 12 cm outer diameter and 0.318 cm wall thickness was inserted into plexi glass tube. This quartz tube will assist to attain better optical access for particle image velocimetry (PIV) and also for shadow sizing analysis for dilute part of test section during experiment.

A mesh made of brass with 53 micron was installed into the test section to hold particles. Another mash with same type was also installed at top part of bed column section to hold the particle from falling out of the bed column. To measure the pressure drop across the bed a small opening was made at 1.5 cm above from bottom of test section. A tygon tube from digital manometer was connected to that small opening. Also a small part of mesh with 53 micron was attached to that small opening to restrain the particle entering into tube. For uniform distribution of gasifying agent (air) to the test section a honeycomb shape distributor was inserted 8 cm below from test section. An external power supply was used for thermal mass flow meter.

3.1.1 Previous Experimental Setup

Before the use of the laboratory scale fluidized bed, a pilot scale fluidized bed was made with 3.8 cm outer diameter, 0.318 cm wall thickness and 183 cm height. This compared against the later experimental setup with a quartz tube bed column with 0.124 m inner diameter. Experimental data of both setups will be compared in the result section with contrast on the effect of bed column diameter. Figure 3.4 shows the pilot scale fluidized bed with 3.8 cm outer thickness.

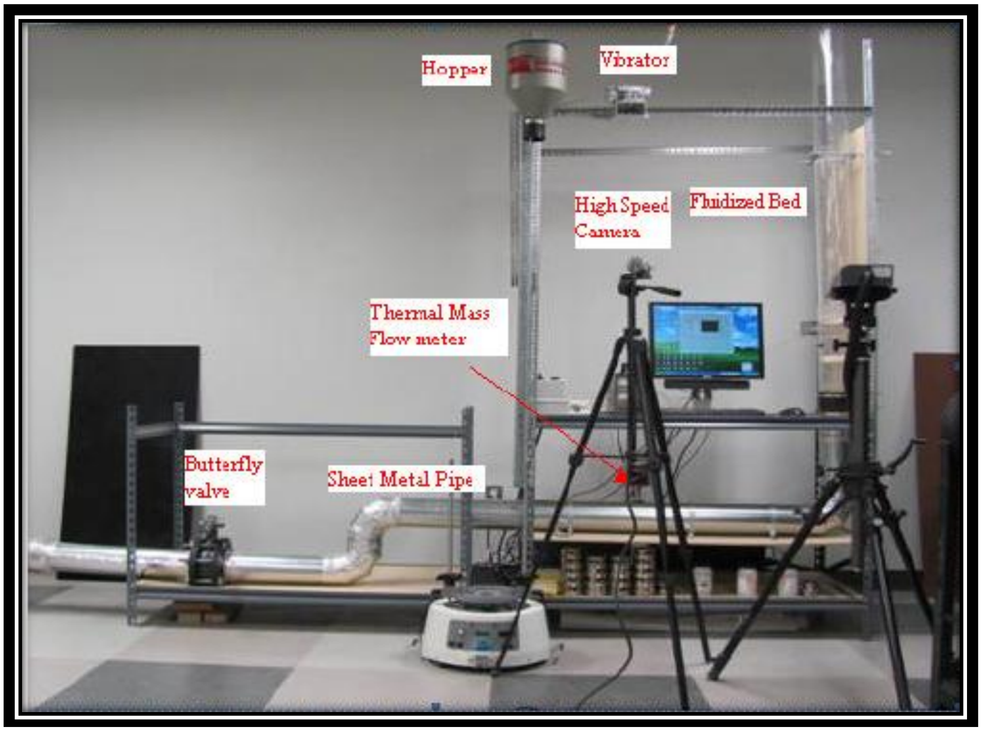

Figure 3.2: Laboratory Scale Fluidized Bed

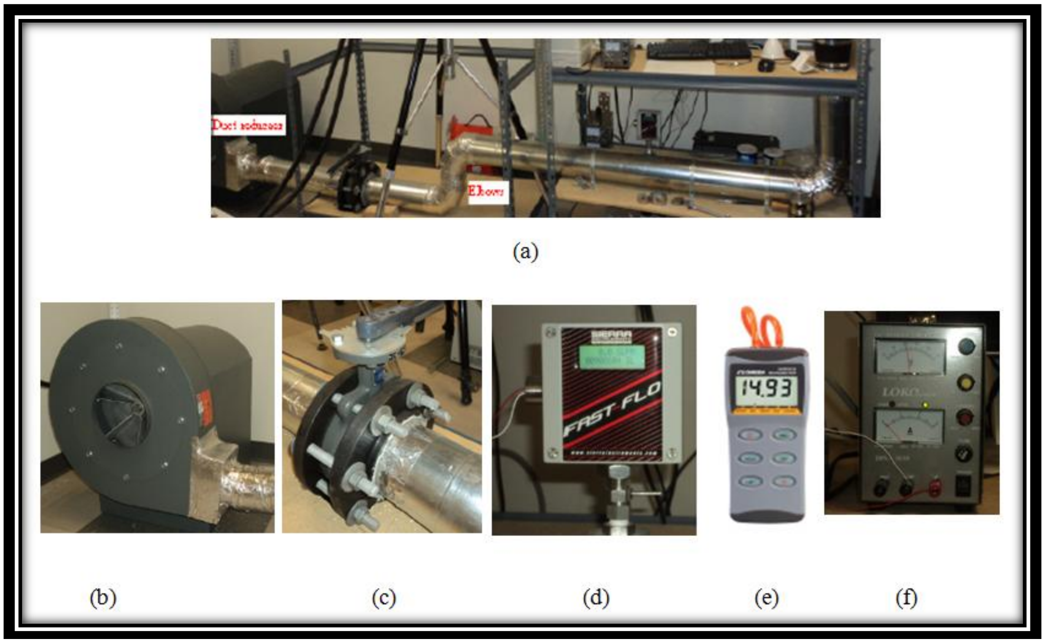

(a)

(b) (c) (d) (e) (f)

Figure 3.3: Air Delivery System (b) High Pressure Blower (c) Butterfly Valve (d) Thermal Mass Flow Meter (e) Digital Differential Manometer (d) External Power Supply

Figure 3.4: Pilot Scale Fluidized Bed

3.2 TEST MATERIAL

To investigate fluidized bed internal hydrodynamics and bed behavior, borosilicate glass beads with density 2230 kg/m^3 were selected as test materials. Two shapes of glass beads were selected for experiment, spherical and non-spherical. In many cases investigation on laboratory scale fluidized bed spherical particles were chosen. But in real coal gasification plant, coal particles are non-spherical. In our experiment we selected both spherical and non-spherical particles. For spherical 1 mm borosilicate glass beads were chosen with density 2230 kg/m^3. Figure 3.5 shows sample image of spherical particles.

3.2.1 Production of Non-Spherical Particles

To produce non spherical particles, 6 mm borosilicate glass beads were crashed by a CRAVER 3851 hydraulic compressor. A die and punch system with 5.08 cm diameter was used to put the spherical particles and then crushed into hydraulic compressor. This stainless steel die and punch was capable to withstand high pressure exerted by hydraulic compressor.

Figure 3.5: Zoomed Image of 1 mm Spherical Partilces.

Crushed particles contained different ranges from few microns to large irregular shape. Crushed large particles were crushed again to get required size as our experimental requirement. To categorize these crushed particles an Octagon digital with 60 Hz, 110 volts, single phase sieve shaker was used with mounting different sieve plate into the sieve shaker to get desired particle size distribution. Ranges of sieve plates were $20\mu m$to $2000\mu m$. To measure the particle weight a precision weighing balance was used with capacity 620g and readability 0.001 g.

3.2.2 Measurement of Particle Size and Shape

There are many industrial applications for aggregate particle materials. To get optimum operation process, measurement of particle size and shape is important. For grading aggregate particle distribution, the most widely used method is mechanical sieving technology. The sieving method divides the aggregate particles into fractions where each fraction contains a certain rage of particle size. (28)

At first, the sieves are arranged by putting them one after another from lower range to higher range. The bottom of a pan was used to hold the powder like particles. After that, the staked sieve was placed into sieve shaker. Sample of aggregate particles put into top larger sieve pan and covered. Sieve shacking was carried out for specific period of time. Particles pass gradually from larger sieve aperture to lower sieve aperture. Finally, fraction of particles from each sieve was weighing by a precision balance with capacity 620 gm. and readability 0.001 gm.

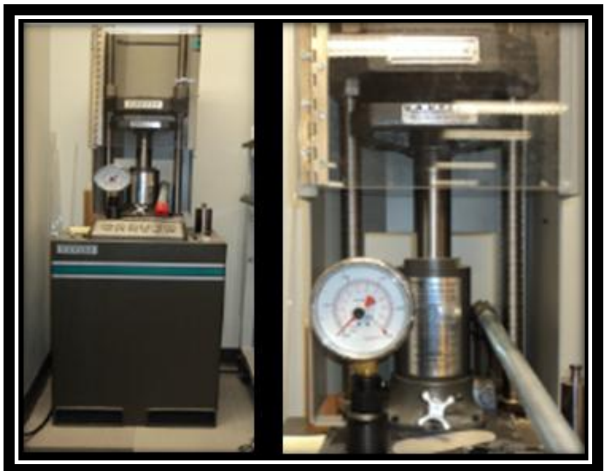

Figure 3.6: CRAVER 3851 Hydraulic Compressor

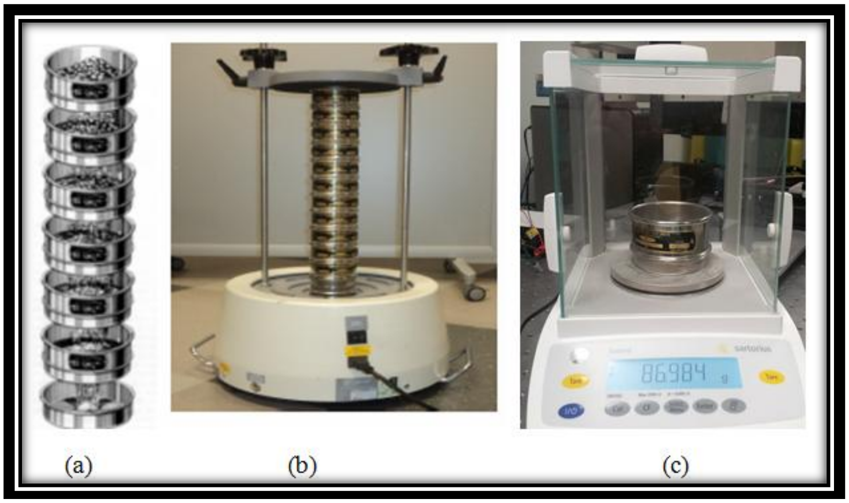

(a) (b) (c)

Figure 3.7: (a) Stake of Sieve Pan (b) Sieve Shaker (c) Precision Balance

3.2.3 Sphericity Measurement

Digital Image Processing (DIP) was used to determine particle size and sphericity. Rather than processing the digital image, DinoLite and the versatile digital microscope were used in combination. At first, the object was focused by adjusting the dial with microscope and then the image was captured. While adjusting the dial, the dial number (magnification value) was noted and put into with magnification window before play with the image to get circumscribe diameter of the particle. Before measure the circumscribe diameter of particle standard measurement ruler was used to calibrate the Dino Captured Microscope.

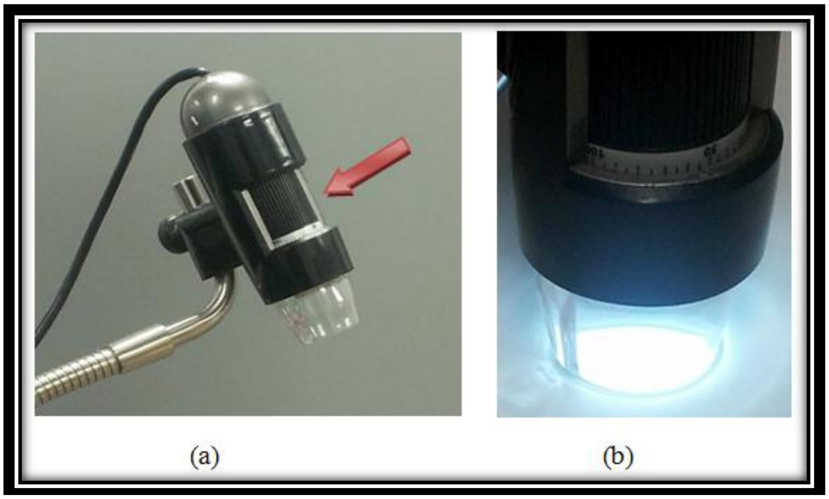

Figure 3.8: (a) Dino Capture Microscope (b) Focusing the Particles

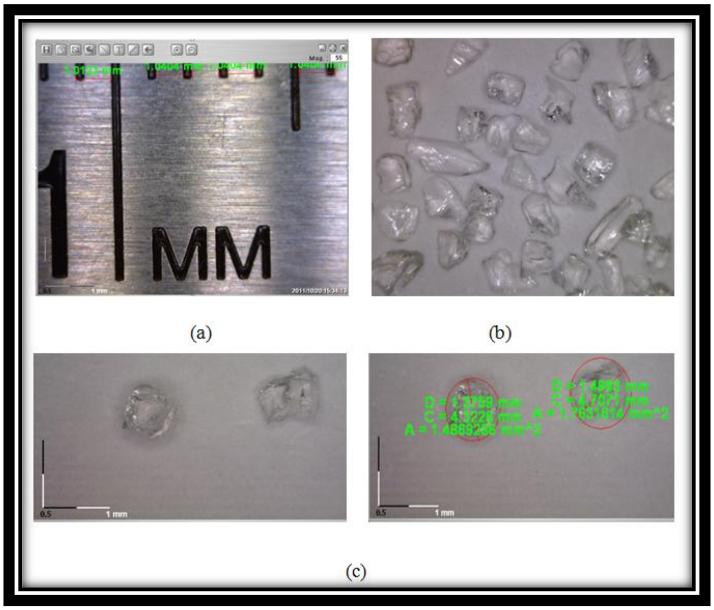

Figure 3.9: (a) Calibration Image (b) Sample Image of Non-Spherical Particle (c) Measurement of Circumscribe Diameter of Non-Spherical Particles

W.C. Krumbein (29) describes the expression for sphericity of made by Hakon Wadell (30) . According to Wadell definition sphericity (φ) is as follows,

$$\varphi = \sqrt[3]{\frac{Volume\ of\ Particle}{Volume\ of\ the\ Circumscribe\ Sphere}}$$

From the Wadell expression, particle volume has the same volume in terms of sphere and the diameter is the nominal diameter of the particle (d). From this expression the basic volume of particle is$\frac{\pi}{6}d^3$. In general, the volume of circumscribe sphere has the longest diameter (a) of the particle, so the volume of circumscribe sphere is$\frac{\pi}{6}a^3$. From these values the Wadell expression for sphericity comes as follows,

$$\varphi = \sqrt[3]{\frac{Volume\ of\ Particle}{Volume\ of\ the\ Circumscribe\ Sphere}} = \frac{\frac{\pi}{6}d^3}{\frac{\pi}{6}a^3} = \frac{d}{a}$$

Krumbein used this expression to measure the sphericity of particle where the sphericity is the ratio of nominal diameter and longest diameter of the particle. Krumbein used to measure the longest diameter of particles with slide calipers. As our test particles are crushed and they have the size of micro level, we used the digital image technology to get the longest diameter of the particles (a) and the nominal diameter was considered as the mean sieve diameter (d).

For our project work, investigating the effect of particle size in fluidized bed, we accumulate different ranges of particles. The ranges of test particle are mentioned in test matrix section 3.5. Sphericity was measured for each particle ranges between 500-2000 micrometer by random selection and the sphericity was found between 0.45 and 0.93. It is also found that mean sphericity of crushed glass particles is 0.65 (Table 2) (12)

3.3 BED PRESSURE DROP AND FLOW RATE MEASUREMENT

A digital manometer capable for measuring differential pressure and also positive or negative gauge pressure was used. To measure bed pressure drop differential pressure option was selected. A tygon tube with 5 mm inner diameter was connected from manometer to small opening in fluidized bed. This small opening was at 1.5 cm above from bottom of fluidized bed. A mash catch with 53 micron was attached to the opening to protect tube and manometer from entering test particles during experiment.

Figure 3.10 shows pressure measurement port connected with digital manometer. This manometer is capable of measuring between 0-2 psi pressure drop.

Table 3.1: Sphericity of Different Shapes, Materials and Commonly Used Packings (12).

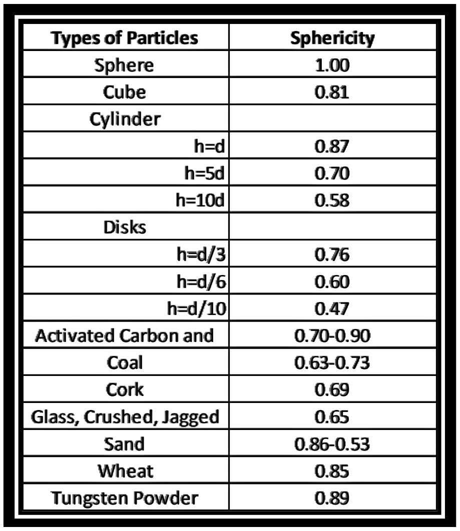

Types of Particles	Sphericity
Sphere	1.00
Cube	0.81
Cylinder	
h=d	0.87
h=5d	0.70
h=10d	0.58
Disks	
h=d/3	0.76
h=d/6	0.60
h=d/10	0.47
Activated Carbon and	0.70-0.90
Coal	0.63-0.73
Cork	0.69
Glass, Crushed, Jagged	0.65
Sand	0.86-0.53
Wheat	0.85
Tungsten Powder	0.89

Figure 3.10: Digital Manometer with RS 232 Cable

Test particles were prepared by adding static guard before experiment. Static guard was used to remove inter particle bonding. Test particles were poured into the bed from top opening of bed column and then bed column was shacked for several times. This shaking helps particles get packed. Before starting experiment it was observed to remove loosened particles. The bed was shacked repeatedly as required. The experiment was measured bed pressure drop along with increasing flow rate of gasifying agent (air). The air flow rate was increased gradually by regulating the butterfly valve until separation starts in the test particles. This is the point of minimum fluidization. Air flow rate and pressure drop was measured at this point and compared for different bed height and different sizes of test particles. At the point of minimum fluidization, a small bed height increasing observed by high speed imaging. This increasing bed height will describe in high speed visualization section. After minimum fluidization, flow rate was increased until they trapped into top mash which is connected into top part of bed column. The particles are entrained and reach the terminal velocity. By this time fluidized bed has undergone different fluidization regimes describe in section 2.4.2.

Measured value of differential pressure drop was feed into Handheld Data Logger (figure 3.11) by RS 232 cable. Both manometer and data logger gives the pressure drop reading up to 3 decimal point with ±0.3% accuracy.

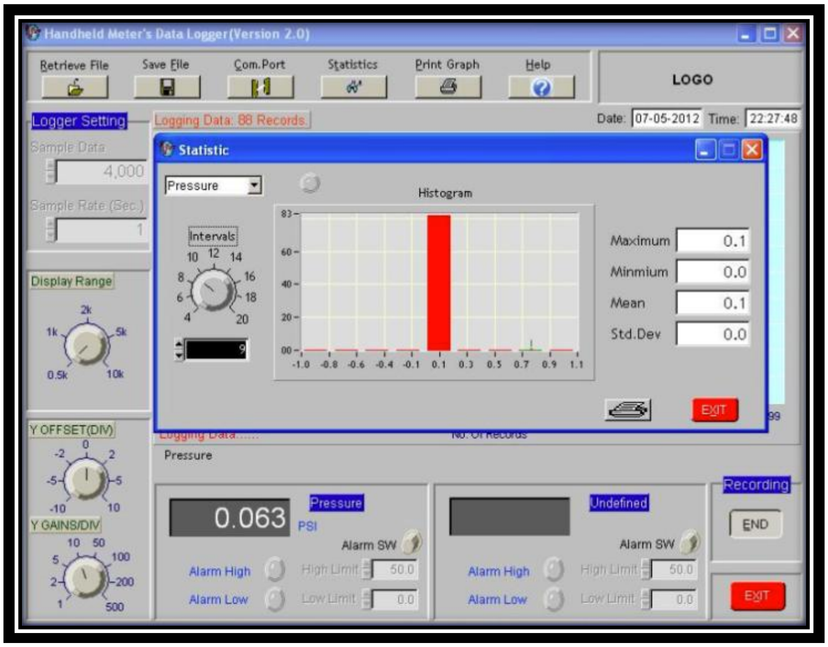
Handheld Meter's Data Logger(Version 2.0)

Date: 07-05-2012 Time: 22:27:48

Logging Data: 88 Records

Sample Data 4,000

Sample Rate (Sec.) 1

Statistic

Pressure

Intervals 9

Maximum 0.1

Minmium 0.0

Mean 0.1

Std.Dev 0.0

Pressure 0.063 PSI

Alarm High High Limit 50.0

Alarm Low Low Limit 0.0

Undefined

Alarm High High Limit 50.0

Alarm Low Low Limit 0.0

Figure 3.11: Handheld Data Logger for Digital Manometer

At the same time mass flow was measured by insertion type mass flow meter with 200 milliseconds response. The flow meter is shown in figure 3.3 (d) which was used to measure volumetric flow rate. This flow meter was also factory calibrated to range of 0 to 4000 SLPM. An external power supply with 20 VDC was also used to run the flow meter. Data from flow meter was feed into Sierra Smart Interface software provided by flow meter manufacturer. Figure 3.12 shows data logger for flow meter.

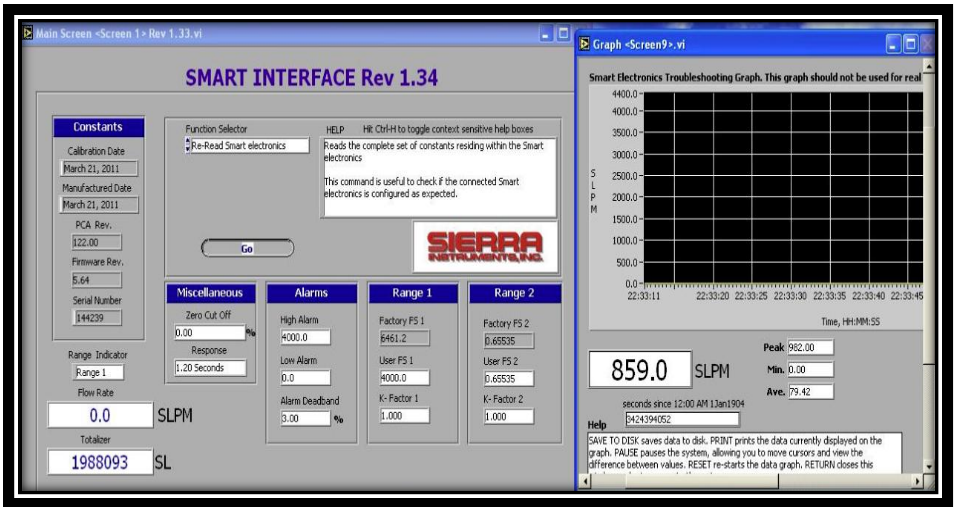

Calibration Date: March 21, 2011
Manufactured Date: March 21, 2011
PCA Rev.: 122.00
Firmware Rev.: 5.64
Serial Number: 144239
Range Indicator: Range 1
Flow Rate: 0.0 SLPM
Totalizer: 1988093 SL
Function Selector: Re-Read Smart electronics

HELP Hit Ctrl-H to toggle context sensitive help boxes

Reads the complete set of constants residing within the Smart electronics

This command is useful to check if the connected Smart electronics is configured as expected.

Zero Cut Off: 0.00 %
Response: 1.20 Seconds
High Alarm: 4000.0
Low Alarm: 0.0
Alarm Deadband: 3.00 %
Factory FS 1: 6461.2
User FS 1: 4000.0
K- Factor 1: 1.000
Factory FS 2: 0.65535
User FS 2: 0.65535
K- Factor 2: 1.000
859.0 SLPM
Peak: 982.00
Min.: 0.00
Ave.: 79.42
seconds since 12:00 AM 1Jan1904: 3424394052

SAVE TO DISK saves data to disk. PRINT prints the data currently displayed on the graph. PAUSE pauses the system, allowing you to move cursors and view the difference between values. RESET re-starts the data graph. RETURN closes this

Figure 3.12: Data Logger for Flow Meter

3.4 HIGH SPEED FLOW VISUALIZATION

In chemical engineering like combustion process, mineral processing, pharmaceutical production, etc, concentrated gas-solid multiphase flows plays an important role. Numerous investigations cite the importance of multiphase flow with their complicated flow structures (31). In our current experiment, an attempt was taken to observe the flow structure in a dilute section while the fluidized bed is fully fluidized. The test section constituted the area 210 mm above from the top surface of test particles (5.5 cm bed height). At this section collapsing of bubbles were visible. Both spherical and non-spherical particles (1 mm nominal diameter) were taken as test particles.

To get particles velocity and particle size the Dynamic Studio Shadow Sizer measurement technique was used. By using backlit and shadow image analysis software this technology can measure size, shape, and velocity including wide range of particle types like bubbles, liquid droplets, solid particles and particles with well-defined contour (32).

3.4.1 Shadow Sizing Measurement Principle

A camera and a light source are required for shadow sizing. A ground glass diffuser plate is also placed between the light source and the test section. This ground glass diffuser helps to take the images of test particles as a shadow. Figure 3.13 shows the schematic diagram of shadow sizing technology.

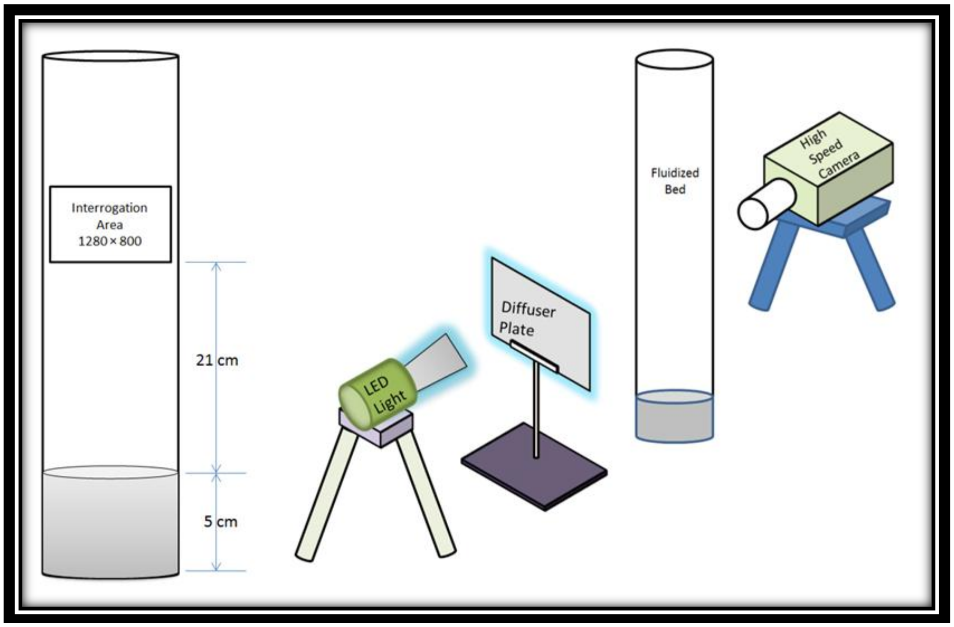

Figure 3.13: Schematic Diagram of Shadow Sizing

For a light source, an LED based honeycomb and constellation illuminator was used to deliver lower to higher luminosity as required to get a shadow image of the test section. Figure 3.14 shows the LED based light source.

Figure 3.14: LED Constellation System

To capture the image a Phantom high speed camera with 5 KHz was used. Image triggering rate can be change by using dynamic studio software. For the current experiment all the images have taken with 1000 Hz. Figure 15 shows the Dantec high speed camera.

Figure 3.15: Dantec High Speed Camera

Both camera and LED light source are synchronized by a timer box. While the particles flows through the test section a light flash acquires and at the same time camera capture the image with help of synchronization device and freeze the particles motions. After acquiring the images shadow sizing software use advanced edge detection algorithm to detect the particles and their shape. To find out the velocity shadow sizing uses two consecutive images with very short interval and particle tracking algorithm.

Figure 3.16: Shadow Sizing

Again without using the backlit light source (LED light), only the high speed camera was used to visualize the fluidized bed test particles behavior. Two state of fluidization were observed for both spherical and non-spherical particles. 1) Incipient of minimum fluidization. 2) Bubbling Fluidization. These two observations will give a fundamental idea about particles behavior for a respective flow velocity of gasifying agent (air).

3.4.2 Calibration

Before processing the images it is required to capture a calibration image. A scale factor can be measured from that calibration image. Images taken by high speed camera are in pixel units. To get physical parameter of particles and their velocities in metric units, it is necessary to convert image units from pixel to metric. A ruler scale is placed in the test section and the calibration image is taken. From the measured scale factor window in dynamic studio software, two points are selected and their numeric distance put in as required in metric units. Figure 3.17 shows a calibration image taken from dynamic studio software.

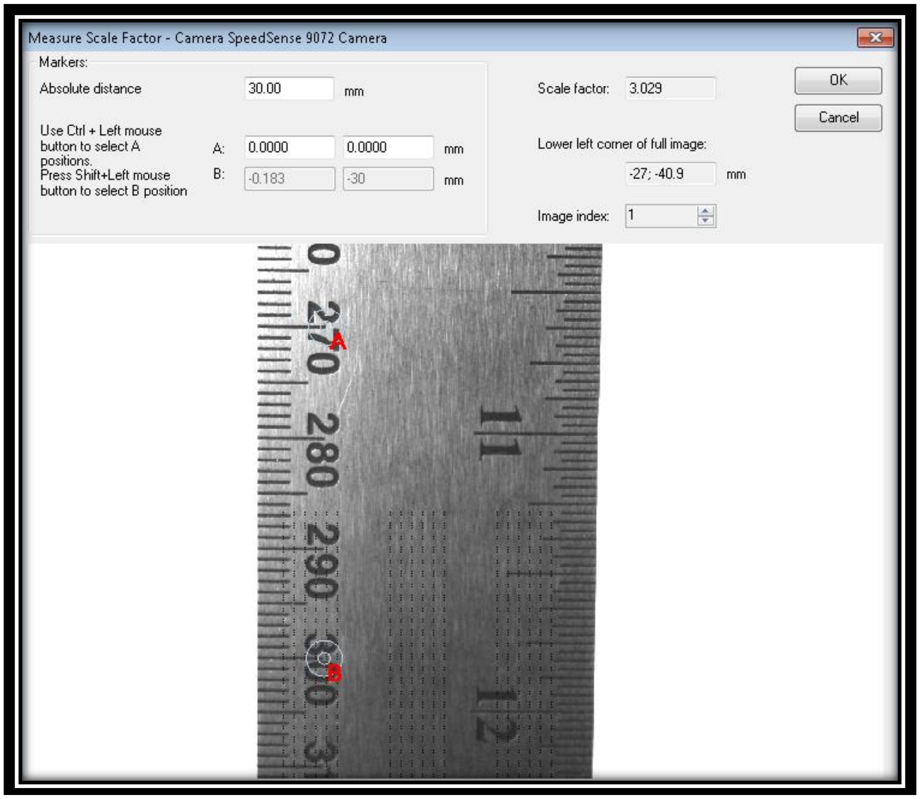

Markers:

Absolute distance 30.00 mm

Use Ctrl + Left mouse button to select A positions.
Press Shift+Left mouse button to select B position

A: 0.0000 0.0000 mm
B: -0.183 -30 mm

Scale factor: 3.029

Lower left corner of full image: -27; -40.9 mm

Image index: 1

Figure 3.17: Calibration Image

3.4.3 Shadow Sizer Processing

According to shadow principle shadow sizer processing acquires data of particle size, shape, velocity, their position. Because of shadow principle there is no limitation of particle size and shape (32). Images were taken from test section with single frame and 1000 Hz. Later single frame images were converted into double frame images. Double frame images were required to get particles velocity. The particle was selected by shadow assistant with their contour and statistical information that includes particle pixel depth and edge gradients. Figure 3.18 shows a selection method of particle with the help of shadow assistant.

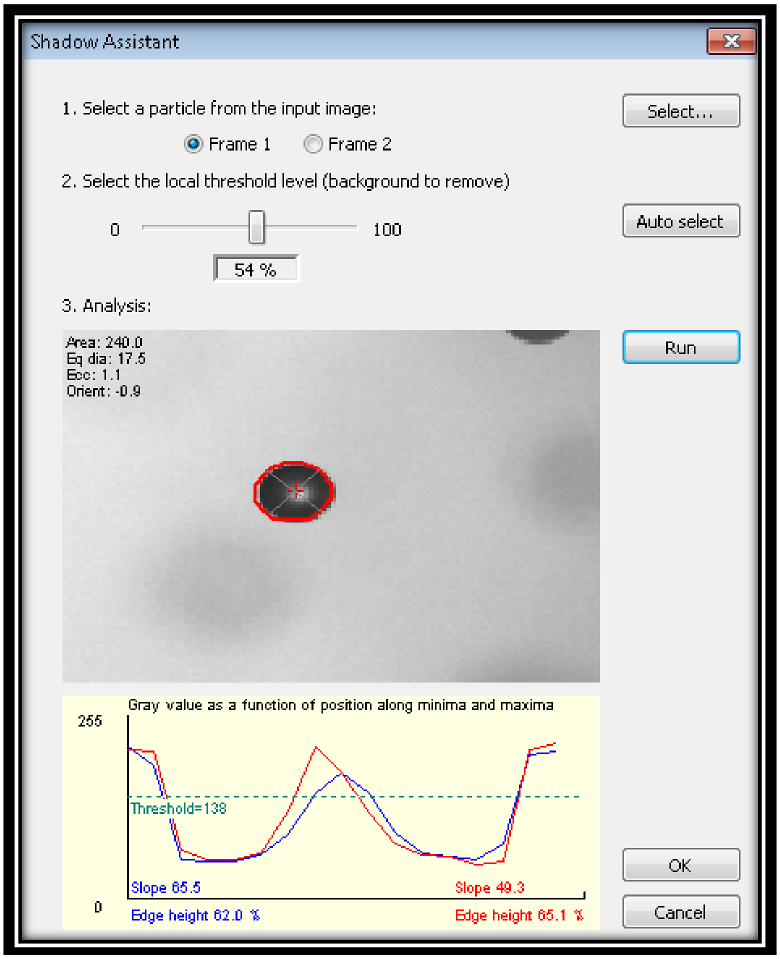

Shadow Assistant

1. Select a particle from the input image:

◉ Frame 1 ○ Frame 2

2. Select the local threshold level (background to remove)

0 100

54 %

3. Analysis:

Area: 240.0
Eq dia: 17.5
Ecc: 1.1
Orient: -0.9

Figure 3.18: Particle Selection with its Contour

After shadow sizer processing, it can detect the particles, their contour, their velocity with direction and also their mean diameter. Figure 3.19 shows a sample of double frame image and figure 3.20 shows its shadow processed results.

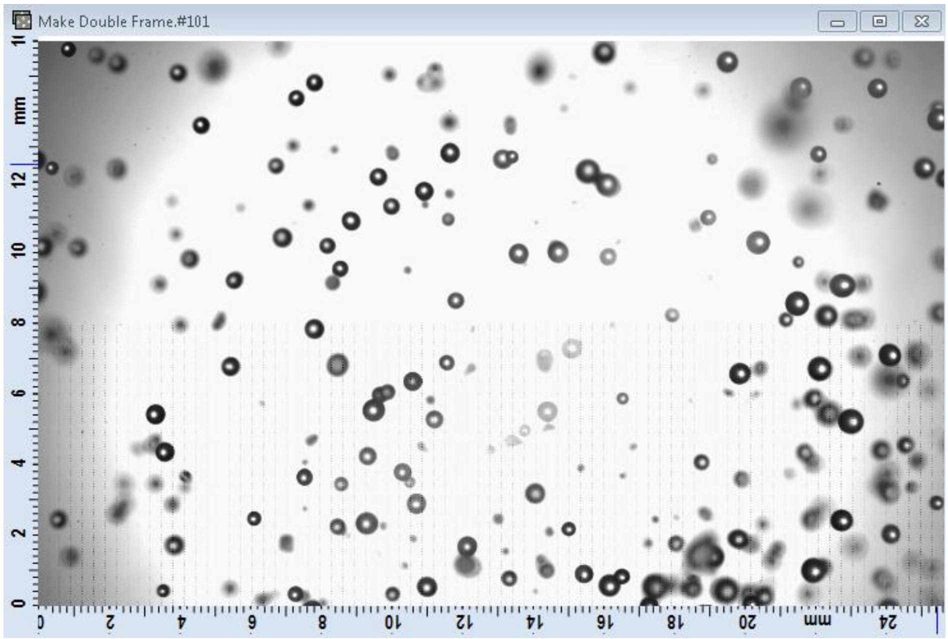

Figure 3.19: Shadow Image of Test Particles

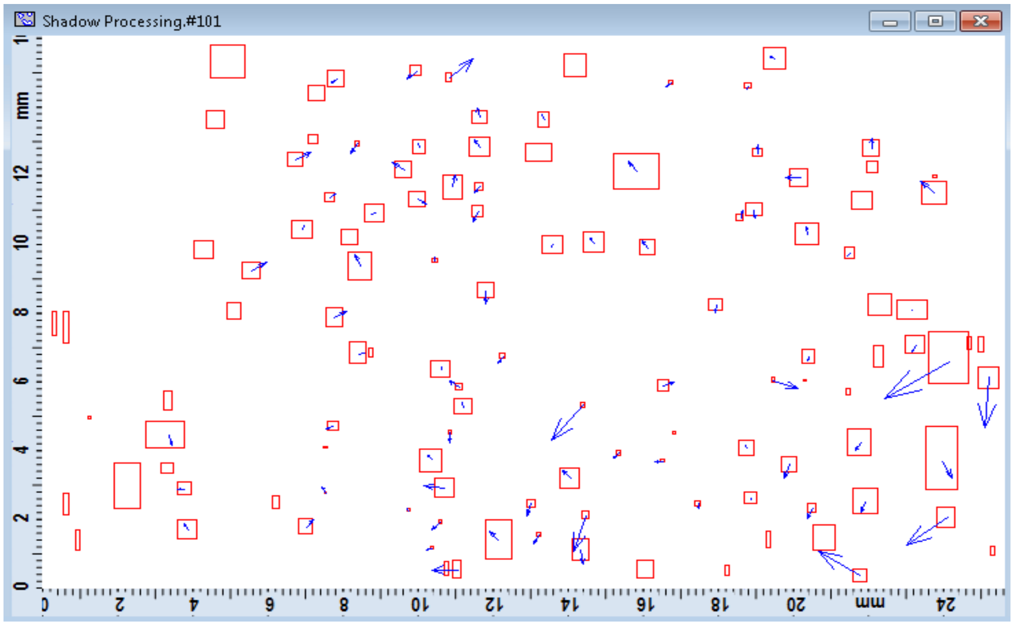

Figure 3.20: Example of Shadow Sizer Processed Result

3.5 TEST MATRIX

Test objectives:

1) Hydrodynamics behavior of fluidized bed with spherical and non-spherical particles
2) High speed flow visualization for spherical and non-spherical particles at incipient fluidization and bubbling fluidization regimes

3) Flow field visualization for spherical and non-spherical particles with shadowgraphy.

A test matrix is shown below of an experiment to observe the hydrodynamics of the laboratory fluidized bed.

Table 3.2: Test Matrix to Observe Bed Hydrodynamics

Fluidized Bed	Particle	Particle Size (mm)	Bed Height (cm)
12.4 cm Bed Diameter	Spherical	1.0 mm	2.0, 2.5, 3.0, 4.0, 5.0, 5.5, 6.0, 6.5, 7.0
	Non-Spherical	1.0-1.18	2.5, 3.0, 4.0, 5.0, 5.5
		0.85-1.0	2.5, 3.0, 4.0, 5.0, 5.5
		0.85-1.18	2.0, 2.5, 3.0, 4.0, 5.0, 5.5
		0.71-0.85	3.0, 4.0, 5.0, 5.5
		0.6.0.71	3.0, 4.0, 5.0, 5.5
		0.50-0.60	3.0, 4.0, 4.5
		0.355-0.50	3.0, 4.0, 5.0, 5.5
		0.155-0.355	3.0, 4.0, 5.0, 5.5
3.5 cm Bed Diameter	Spherical	1.0 mm	3.0, 5.0

Table 3.3: Test Matrix for High Speed Flow Visualization

Particle Size (mm)	Shape	Fluidization State
1.0	Spherical	Incipient & Bubbling Fluidization
0.85-1.0	Non-Spherical	
0.355-0.50		

Table 3.4: Test Matrix for Shadowgraphy

Particle Size (mm)	Shape	Fluidization State
1.0	Spherical	Full Fluidization & Bubbling Fluidization
0.85-1.18	Non-Spherical	
0.355-0.50		
0.155-0.355		

3.6 STATISTICAL ANALYSIS OF EXPERIMENTAL DATA

There is some inherent randomness in each measurement. This randomness is mainly caused by uncontrolled variables and precision variance of measuring instruments. This randomness necessitates statistical analysis for data and drawing conclusions. Table 3.4 shows 29 data points of pressure drop (unit=Pa) taken with constant flow velocity .073 m/sec.

Table 3.5: Experimental data set of pressure drop at 0.73 m/sec flow velocity

506.07342	499.8682	503.3155	515.726	515.726	511.5892
512.27868	494.3524	509.5208	494.4903	510.8997	516.4155
496.42079	516.4155	506.7629	512.9682	517.7945	528.1366
502.62605	499.1787	508.1418	499.1787	512.2787	507.4524
507.45237	515.726	499.8682	526.0681	529.5155	

These measurements were taken for non-spherical particles ranges from 355-500 µm. 1 minute interval were taken before taking each data. Basic statistics of measured data has shown in table 3.5

Table 3.6: Statistical Description of Measured Data

Number of Measured Data	Minimum Value	Maximum Value	Mean Value	Median	Standard Deviation
29	494.35	529.52	509.53	509.52	9.4

From statistical analysis it is found that standard deviation is 9.4 Pa. Standard deviations are considered as statistically significant – normal random error (34). Because of some error in measurement a constant value is always needed to add up to the measured value. That added value was 6.89 Pa. This value is referred as bias error. Table 3.6 shows a statistical analysis of measured data.

Table 3.7: Statistical Analysis of Pressure Drop with .073 m/sec Flow Velocity

Mean Pressure	Random Error	Bias Error
509.53 Pa	9.40 Pa	6.89 Pa
Error in Percentage	1.84%	1.35%

On the other hand figure 21 shows a statistical histogram of pressure drop with din width range 5 Pa.

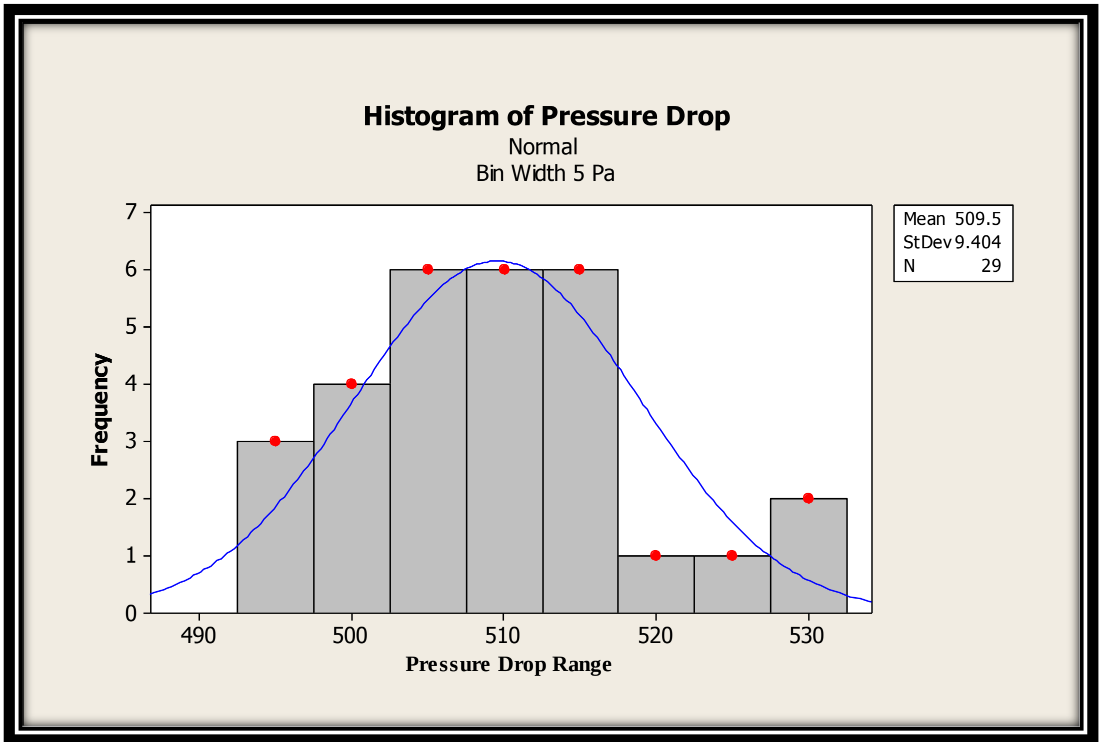

Figure 3.21: Histogram of Pressure Drop

95 % Confidence interval was also calculated by using t-distribution table. From the measured data, the degree of freedom is 28. For 95% confidence interval and degree freedom 28 our required value from t-distribution table is 2.048. Finally, from standard procedure our lower and upper ranges were found. The ranges are 505.47 to 513.09.

Chapter 4: Results and Discussions

This section presents experimental results of hydrodynamic behavior of bed for spherical and non-spherical particles. Also high speed flow visualization at different flow regimes and flow field visualization using shadow sizing technology.

Minimum fluidization velocity and bed pressure drop are the most important parameters to characterize fluidized bed. From experimental results of hydrodynamic behavior the following section has described which has the effect on minimum fluidization velocity and bed pressure drop.

1) Effect of bed height for spherical and non-spherical particles.
2) Effect of bed diameter for spherical and non-spherical particles.
3) Effect of particle size on minimum fluidization

On the other hand visualization at two fluidization regimes also observed with high speed camera. At the state of incipient minimum fluidization and bubbling fluidization regimes this high speed visualization has observed for both spherical and non-spherical particles. Again to observed flow field at full fluidization region for both spherical and non-spherical particles with different size was also observed with shadow sizing technology. Shadow sizing technology is described in section 3.4.

4.1 EFFECT OF BED HEIGHT FOR SPHERICAL PARTICLES

Pressure drop and minimum fluidization velocity were measured across the bed with increasing superficial gas velocity. Spherical and non-spherical test particles with 1 mm nominal diameter were used to observe the effect of bed height. Figure 4.1 shows effect of bed height from 3 to 6 cm for spherical particles for 12.4 cm bed diameter.

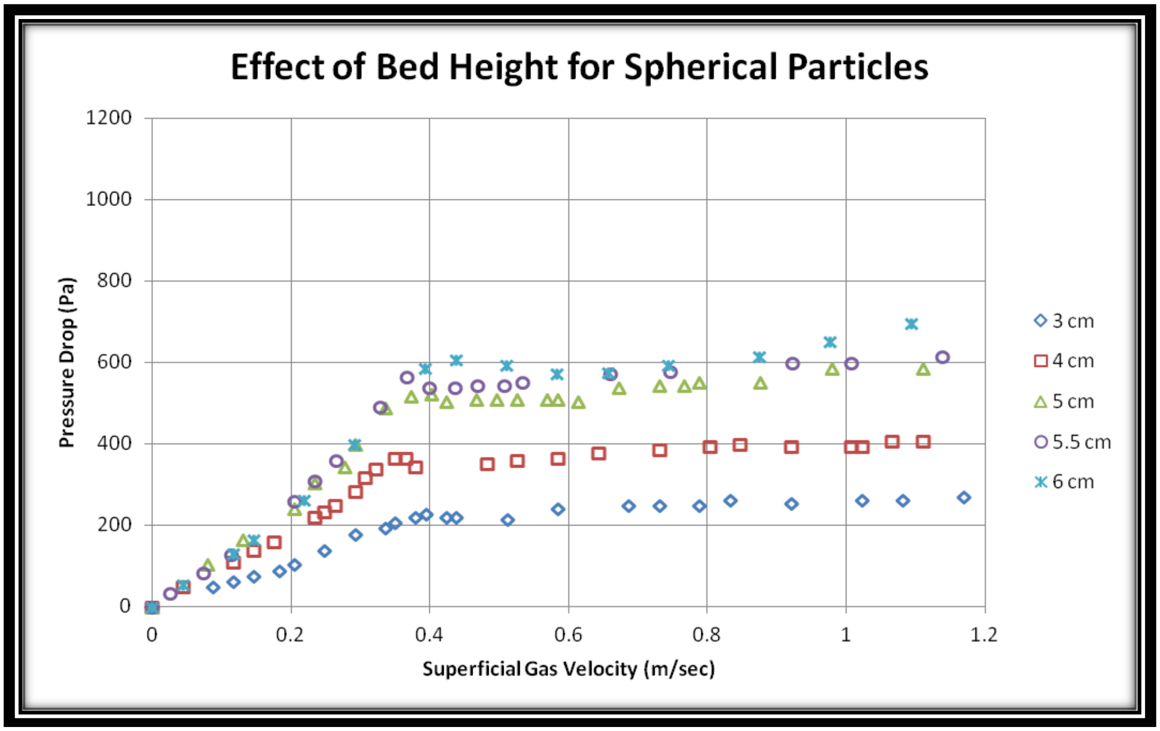

Figure 4.1: Effect of Bed Height for Spherical Particles

Table 4.1: Analytical and Experimental Pressure Drop for 1 mm Spherical Particles

Bed Height (cm)	Analytical Minimum Fluidization Velocity,(m/sec)	Experimental Minimum Fluidization Velocity, Vs (m/sec)	Analytical Pressure Drop (Pa)	Experimental Pressure Drop (Pa)	Deviation in Pressure Drop	Ratio of Bed Height and Bed Diameter (H/D)
2.00	0.40	0.42	273.24	130.00	52.42%	0.16
2.50	0.40	0.40	341.53	193.00	43.49%	0.20
3.00	0.40	0.39	409.83	227.52	44.48%	0.24
4.00	0.40	0.36	546.44	365.42	33.13%	0.32
5.00	0.40	0.40	683.00	524.00	23.28%	0.40
5.50	0.40	0.40	751.36	565.36	24.76%	0.44
6.00	0.40	0.43	819.00	606.00	26.01%	0.48
6.50	0.40	0.36	887.00	682.00	23.11%	0.52
7.00	0.40	0.40	956.00	737.00	22.91%	0.56

Analytical pressure drop was calculated from Ergun equation (eq^{n} 4) which is a function of particle diameter, bed height, superficial gas velocity, particle density, gas density and void fraction. Table 4.1 shows the list of analytical and experimental measurement of pressure drop for different height ranges from 2 to 7 cm. Comparatively large deviation between analytical and experimental pressure drop found in 2 cm bed height. This deviation gradually decreases with the increase of bed height. On other way it can be say that while the ratio of bed height and bed diameter (H/D) increases the deviation between analytical and experimental pressure drop decreases. Moreover this deviation became constant while the H/D ratio is in range from 0.4 to 0.56.

A graphical representation of deviation between analytical and experimental pressure drop for spherical particles (1mm) is presented in figure 4.2 for a particular bed height 5.5 cm.

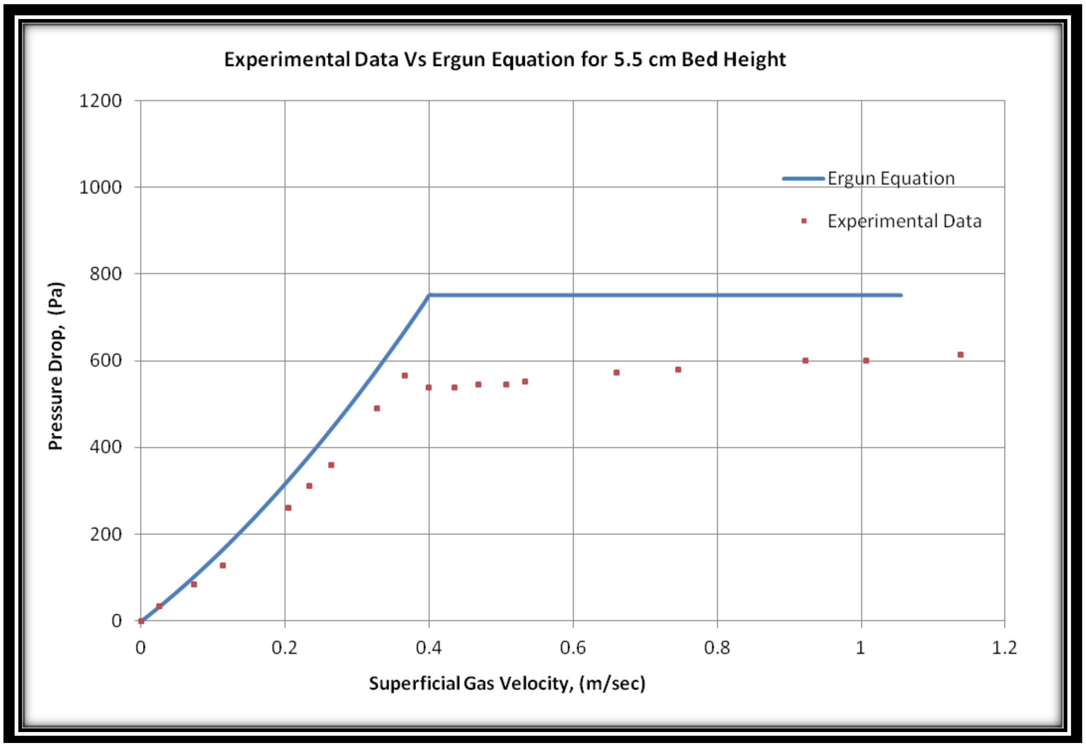

Figure 4.2: Analytical Vs. Experimental Pressure Drop for Spherical Particles.

The analytical result is derived from Ergun equation (equation 4) which is a function of particle diameter, bed diameter, densities, superficial gas velocities and void fraction. In experimental result all the parameter is taken same as analytical. But in experimental result the minimum fluidization occurs much early than analytical. This deviation comes out for void fraction changing during experiment. Changing of void fraction is observed by high speed imaging system. From the static bed situation when superficial gas velocity is zero imaging was taken with high speed camera and superficial gas velocity was increased gradually. A small increase in bed height is observed just before minimum fluidization which indicates the changing in void fraction. Because of increasing in void fraction, minimum fluidization happens early in experiment. For analytical, void fraction remain constant. Figure 4.3 shows the increased bed height just before minimum fluidization.

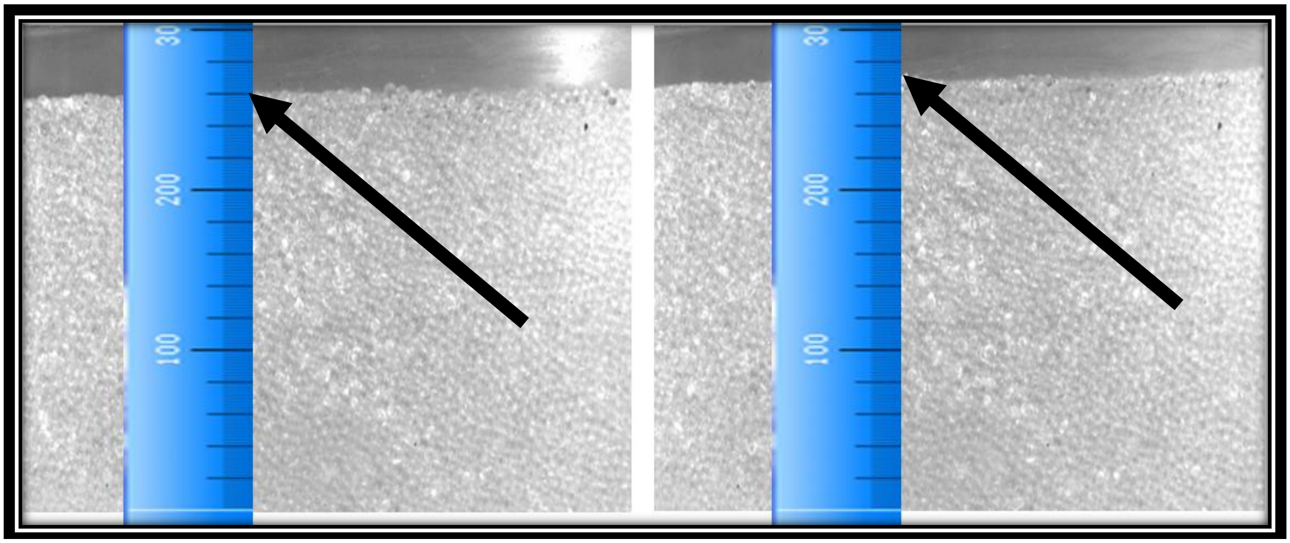

Figure 4.3: Increased Bed Height before Minimum Fluidization for Spherical Particles

As minimum fluidization velocity is an important parameter for fluidized bed, figure 4.4 is plotted to find out the effect of bed height on minimum fluidization velocity.

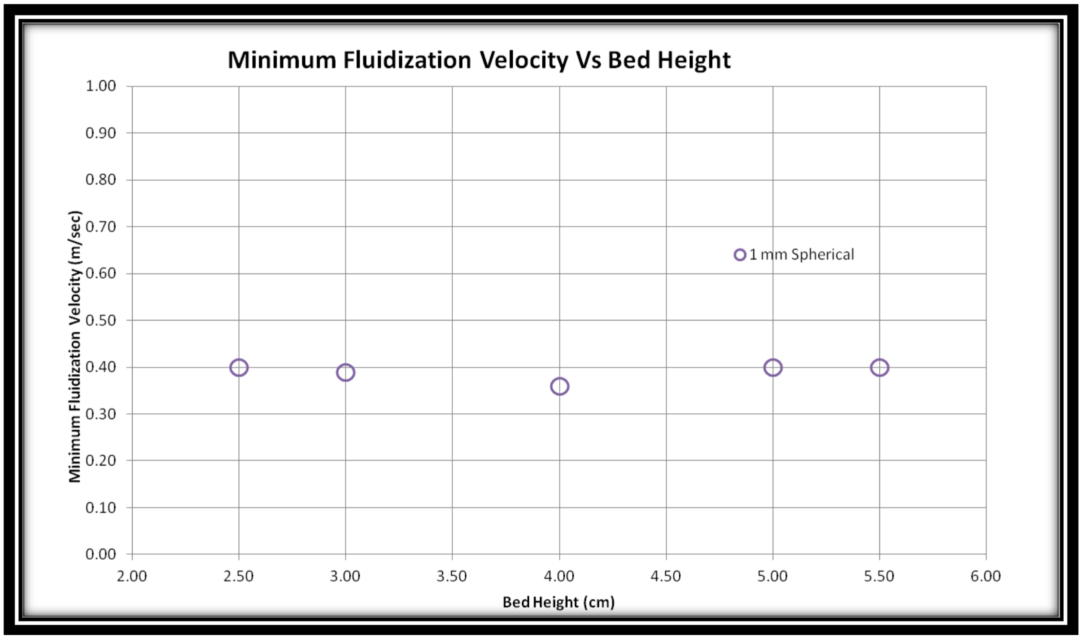

Figure 4.4: Minimum Fluidization velocity vs. Bed Height for Spherical Particles

From figure 4.4 it is shown that minimum fluidization velocity following nearly a constant line for increasing bed height and it can be concluded that minimum fluidization velocity is independent on bed height.

4.2 EFFECT OF BED HEIGHT FOR NON-SPHERICAL PARTICLES

The effect of bed height was also investigated for non-spherical particles. This section will describe about one range of non-spherical particles with 850-1000 µm. Experiment was done as like spherical particle. At first particles were filled with desired height and shacked the bed column for couple of times. Pressure drop was measured with increasing superficial gas velocities. Figure 4.5 shows the experimental results of pressure drop vs. superficial gas velocities for non-spherical particles. A clear description of figure 4.5 will be found in table 4.2 for non-spherical particles with different bed height ranges from 2.5 cm to 5.5 cm bed height

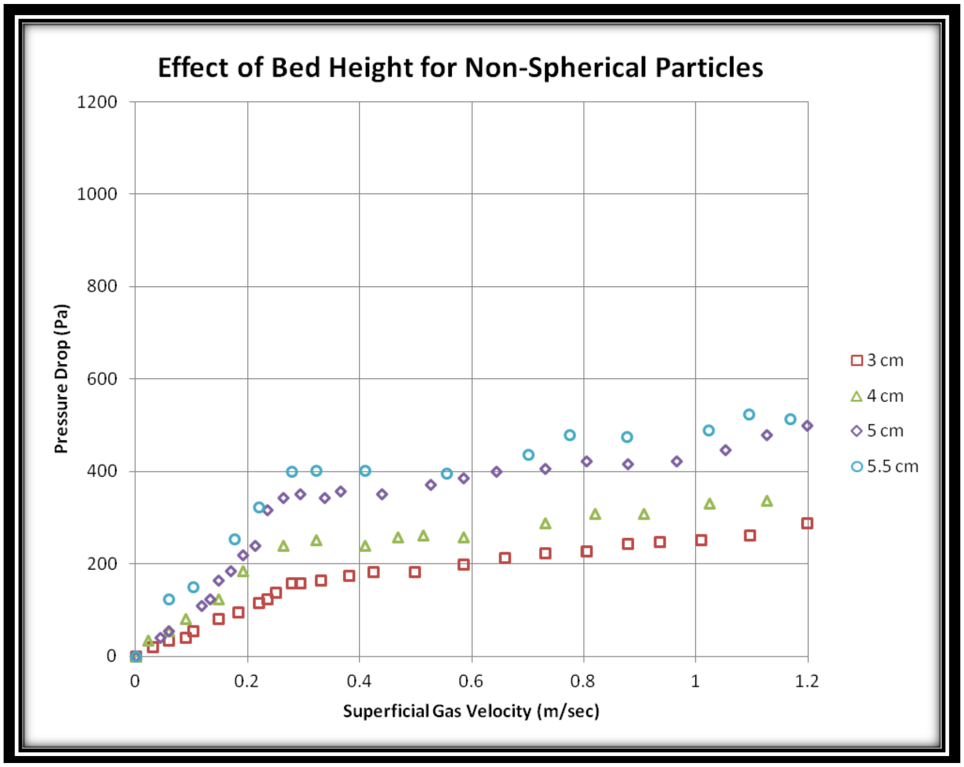

Figure 4.5: Effect of Bed Height for Non-Spherical Particles (850-1000µm)

Table 4.2: Analytical and Experimental Pressure Drop for Non-Spherical Particles (850-1000µm)

Bed Height (cm)	Analytical Min. fluidization velocity, m/sec	Exp. Min. Fluidization Velocity (m/sec)	analytical pressure drop	Exp. Pressure Drop/Pa	Deviation
2.5	0.34	0.29	258	110.31	57.24%
3	0.34	0.32	309	165.5	46.44%
4	0.34	0.32	412	251	39.08%
5	0.34	0.29	516	351.6	31.86%
5.5	0.34	0.32	567	403	28.92%

From Table 4.1, it was shown that deviation between analytical and experimental decreases with increasing bed height. This indicates the H/D ratio also plays an important role. A graphical representation of deviation between analytical and experimental is shown in figure 4.6 for single bed height.

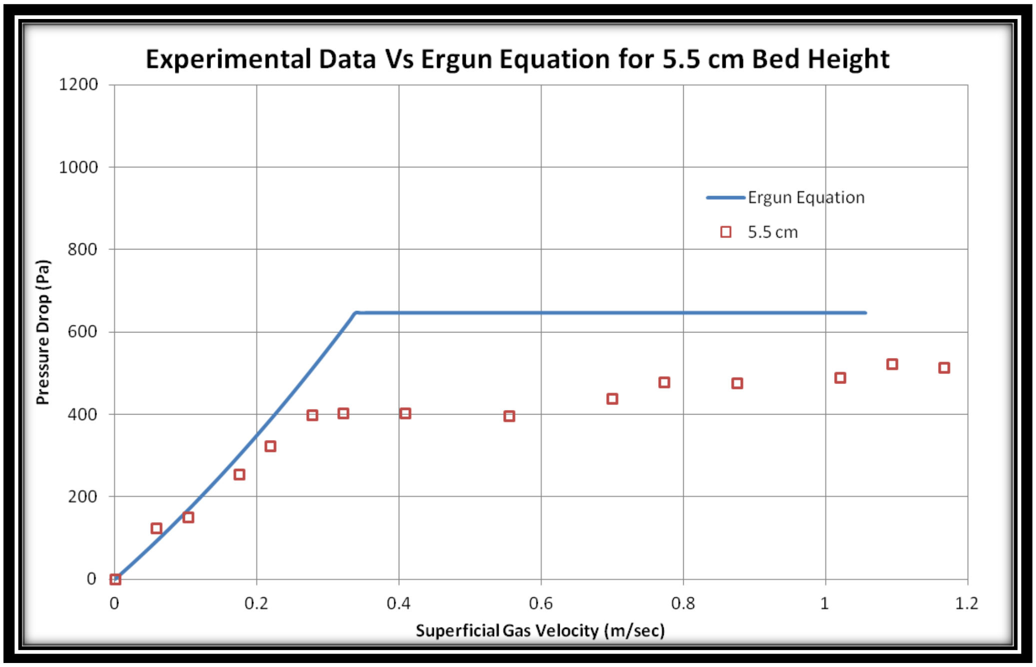

Figure 4.6: Analytical Vs. Experimental Pressure Drop for Spherical Particles.

Investigating the deviation with spherical particles was done with high speed imaging. This method was also employed for non-spherical particles. Like spherical test particles, there was no increased bed height observed before incipient minimum fluidization but channeling observed right before incipient minimum fluidization. Shape of spherical particles is uniform and they are densely packed in the fluidized bed. The shape of non-spherical particles was not uniform and not densely packed as was seen with the spherical. Instead of having increased bed height before minimum fluidization, a channeling opens where the particles are loosely packed. Thus make a change in void fraction and minimum fluidization earlier as expected.

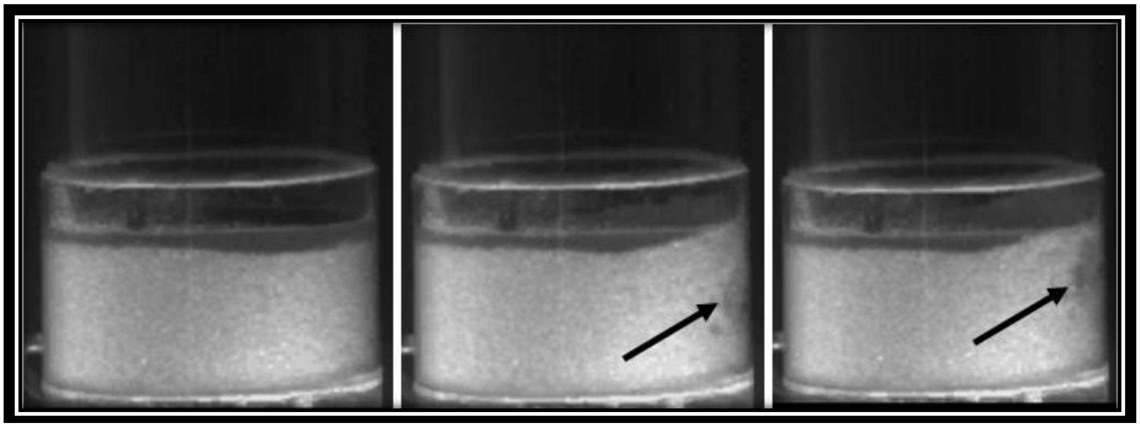

Figure 4.7: Channeling before Minimum Fluidization for Non-Spherical Particles

A graphical presentation of minimum fluidization with increasing bed height is also presented in figure 4.8 for non-spherical test particles.

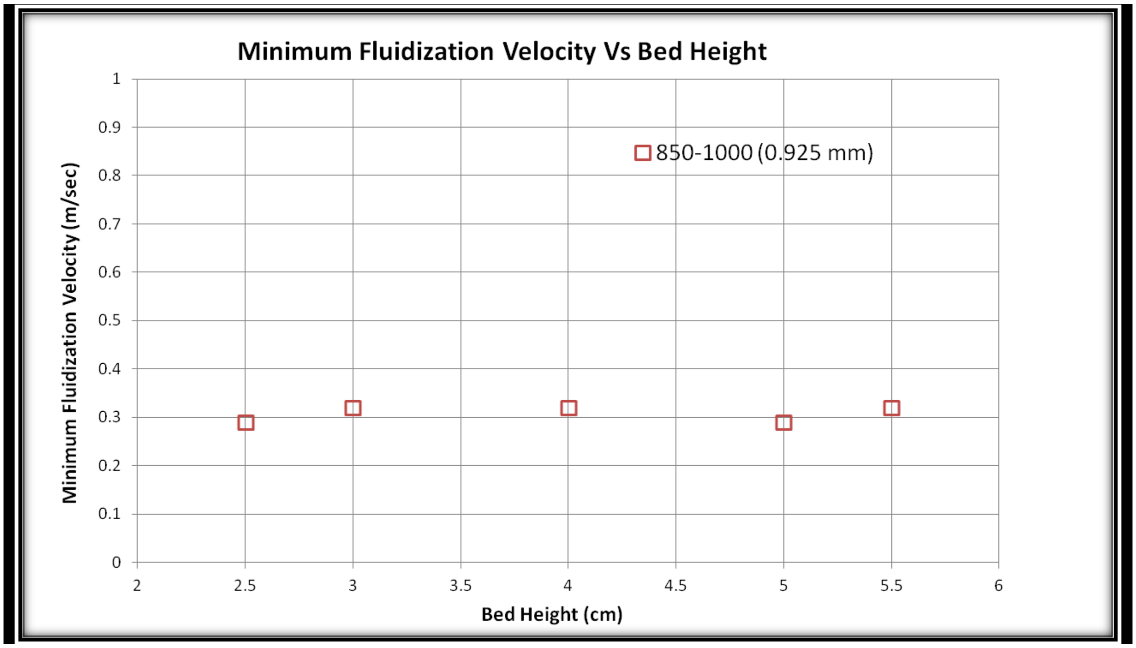

Figure 4.8: Minimum Fluidization velocity vs. Bed Height for Non-Spherical Particles

From figure 4.8 it is shown that minimum fluidization velocities remain nearly same with increasing bed height. It can be concluded that like spherical particles non-spherical particles are independent on increasing or decreasing bed heights.

4.3 EFFECT OF PARTICLE SHAPE

To investigate the effect of particle shape, a specific range of non-spherical test particles were made by mixing two ranges of particles. Bidisperse test particles were made by mixing 0.85-1.0 mm and 1.0 -1.18 mm ranges particles where the mean diameter of this bidisperse particles 1.01 mm. This attempt was done to investigate the effect of spherical and non-spherical particles with same size. By making a comparison between spherical and non-spherical particles with same size we will find out the effect of particle shape where the effect of particle size is negligible. Table 4.3 shows the experimental measurement for both shapes at different bed height.

Table 4.3: Experimental Results for Spherical and Non-Spherical Particles with Same Size

		Spherical (1 mm)		Non-Spherical (≈ 1 mm)	
SL	Bed Height	Min. Fluidizatoin velocity for Spherical	Bed Pressure Drop for Spherical	Min. Fluidizatoin velocity for Non-Spherical	Bed Pressure Drop for Non-Spherical
1	2.5	0.40	193.00	0.25	151
2	3	0.39	227.00	0.26	241
3	4	0.36	365.42	0.26	344
4	5	0.40	524.00	0.29	427.47
5	5.5	0.40	537.80	0.26	544

From table 4.3, it can be seen that although both test particles have the same size, there is a difference between minimum fluidization velocity and also in bed pressure drop for different bed height. A graphical plot also presented in figure 4.9 for a specific bed height 5 cm.

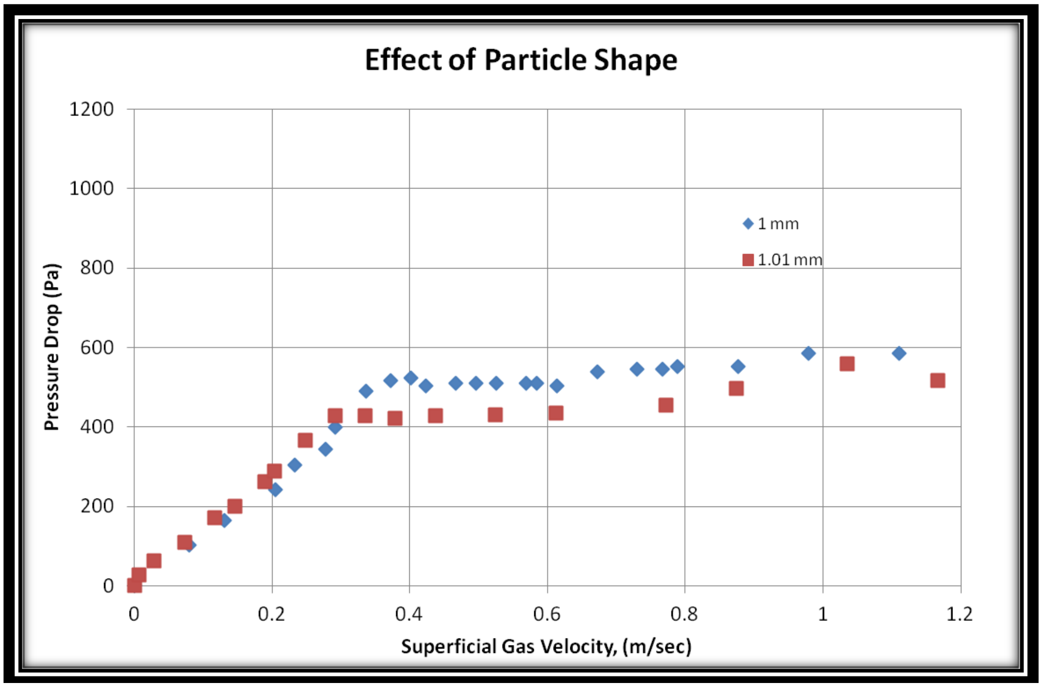

Figure 4.9: Pressure Drop vs. Gas Velocity for Spherical and Non-Spherical Particles with same size at 5 cm Bed Height

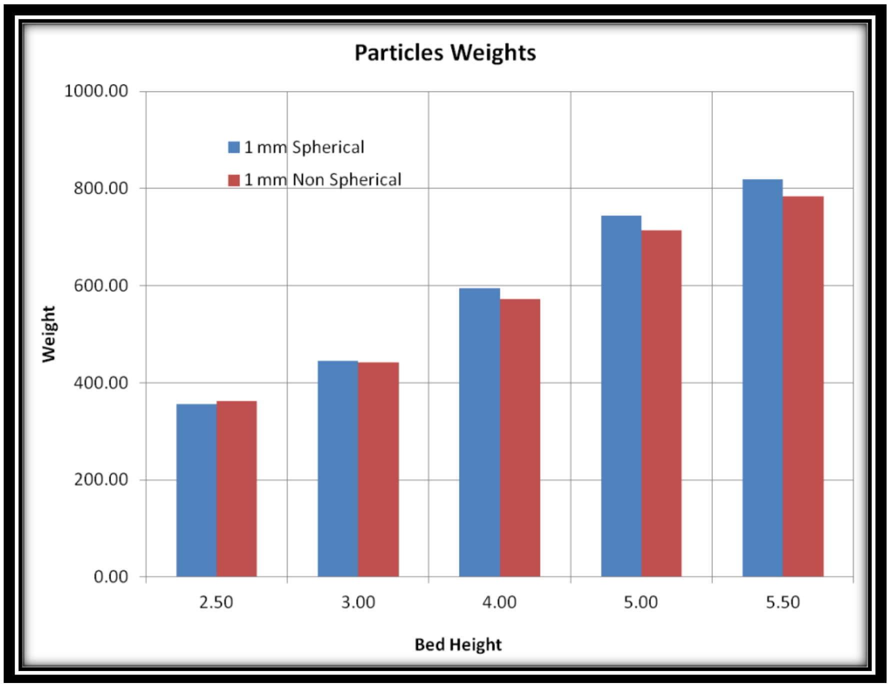

Figure 4.10: Particles Weight at Different Bed Height for Spherical and Non-Spherical Shape

Experimental measurement points of non-spherical particles follow the point with spherical particles. But minimum fluidization occurs for non-spherical much earlier than spherical particles. At all bed height from 2.5 cm to 5 cm, particles weight were measured for both shape of particles. At all height they have near same weight of particles. Figure 4.10 represents the measured weight of both particles shape at different bed height. Although both test particles have same size and same weight at each bed height a deviation has observed in minimum fluidization velocities for each bed height (Table 4.3 and figure 4.9). Minimum fluidization happens earlier for non-spherical shape. This early minimum fluidization is the result of higher void fraction. Non-spherical particles are loosely packed than spherical particles. Thus non-spherical particles have higher void fraction than spherical particles and early minimum fluidization happens for this non-spherical particles.

4.4 EFFECT OF BED DIAMETER

Before laboratory scale fluidized bed (figure) a pilot scale fluidized bed were made (figure). To observe the effect of bed diameter on fluidized bed, spherical test particles with 1 mm nominal diameter was tested in both fluidized bed. The two fluidized beds contain column diameter with 12.4 cm and 3.4 cm. Figure 4.11 shows graphical plot on effect of bed diameter at 5 cm bed height.

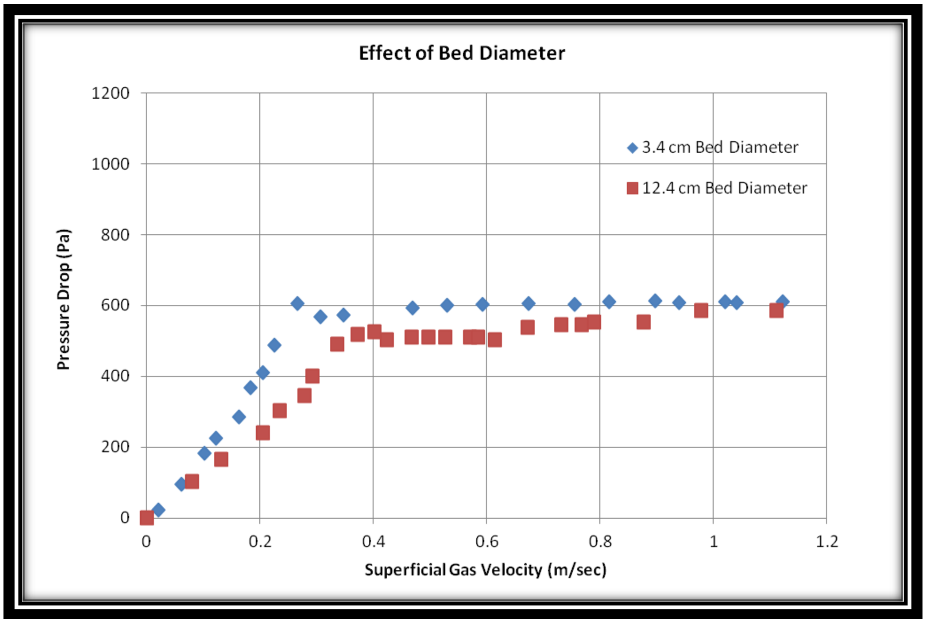

Figure 4.11: Effect of Bed Diameter at 5 cm Bed Height

From figure 4.11 it can be seen that by decreasing the bed diameter pressure drop increased and minimum fluidization velocity decreased. However, in literature it has been some different results on the effect of bed diameter. In some studies it has been found, minimum fluidization velocity increase with decreasing bed diameter. Our present experimental observation consists large particle size, variations in Sphericity, larger difference in bed diameter, larger difference in bed height over bed diameter ratio. A wide range of bed diameter with different bed height observation may reveal possible empirical correlations for fluidized bed on bed diameter.

4.5 HIGH SPEED VISUALIZATION OF FLOW REGIMES

Different fluidization regimes were described in section 2.4.2. High speed imaging technology was selected to investigate the bed behavior in different fluidization regimes. Among different regimes two regimes were selected for investigation. 1) Incipient Minimum Fluidization and 2) Bubbling Fluidization. Both spherical (1 mm) and non-spherical particles (850-1000 µm) were used as test particles. These two regimes were selected because they play an important role on hydrodynamics behavior of fluidized bed.

A high-speed digital image optical technique has been used to observe 12.4 cm bed. A high speed camera (5 KHz) with couple of fluorescent light focusing on test section was used for this high speed observation. Some consecutive images of predetermined fluidization regimes for spherical and non-spherical particles were presented bellow

4.5.1 Incipient Minimum Fluidization

This regime happens at point of minimum fluidization and at that point upward fluid drag force is equal to the total weight of the particles. Figure 4.12 and 4.13 shows consecutive images from static bed to incipient fluidization state for both spherical and non-spherical particles. Images were arranged from left to right.

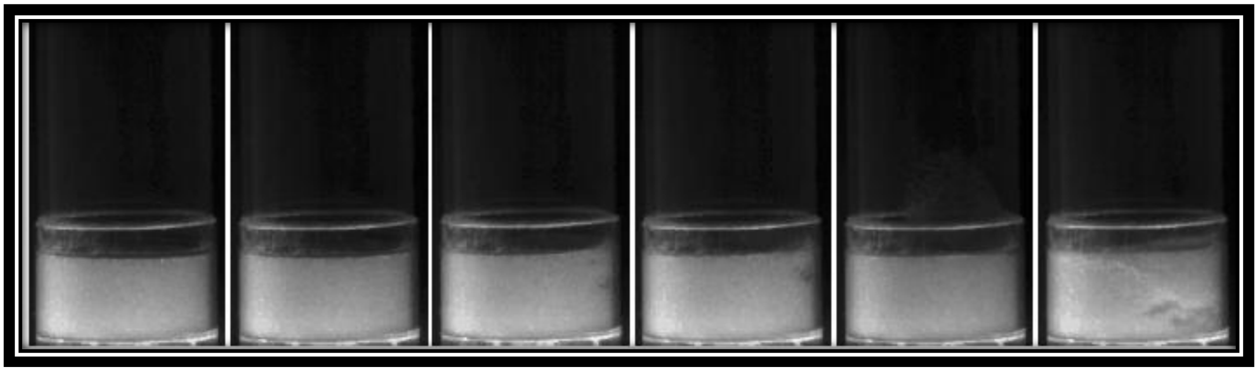

Figure 4.12: Spherical Particles (1 mm)

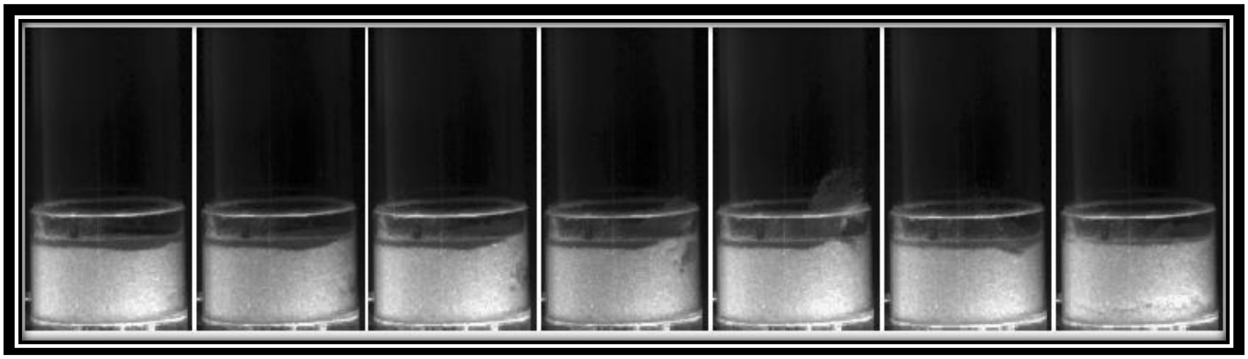

Figure 4.13: Non-Spherical Particles (850-1000 μm)

For spherical particles, a significant observable increase in bed height was found as the superficial gas velocity increased. This is due to densely packed for their uniform shape compare to non-spherical particles. For non-spherical particles no observable bed height was found. Channeling observed for both spherical and non-spherical particles. Much higher channeling observed for non-spherical particles compare to spherical particles. Because of their irregular shape they are loosely packed and much higher channeling happens near with wall.

Right after channeling for both spherical and non-spherical bubbles appears at bottom part of the bed. At this point minimum fluidization appears. From the plot of pressure drop with increasing superficial gas velocity a smooth minimum fluidization found for spherical particles for their reduced channeling.

4.5.2 Bubbling Fluidization

Bubbling fluidization happens with higher gas flow rate beyond minimum fluidization. Figure 4.14 and 4.15 shows consecutive images from minimum fluidization to bubbling fluidization for both spherical and non-spherical particles. It is observed that bubble appears at bottom and it rise from bottom to top of the bed. It is also observed that bubbles coalescence in vertical and horizontal directions. When bubbles rises up, particles weight in upper part get reduces which helps bubbles to get bigger in size by merging tailing bubbles with leading bubbles. For horizontal coalescence the bubbles merge with the adjacent bubbles.

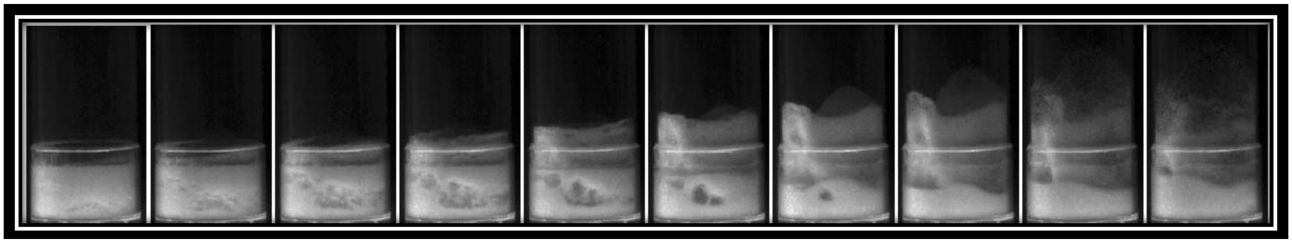

Figure 4.14: Spherical Particles

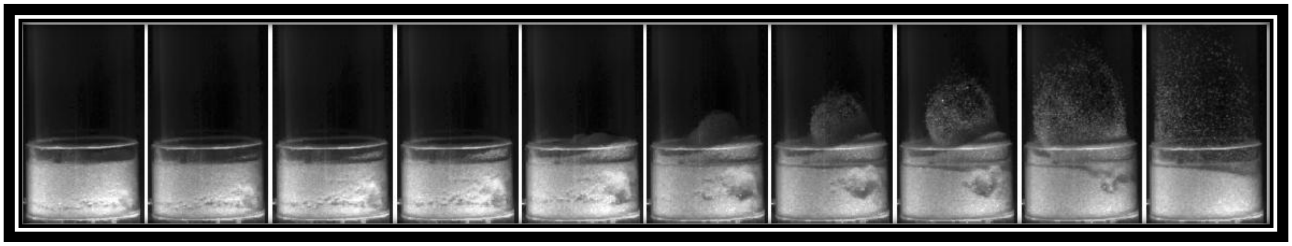

Figure 4.15: Non-Spherical Particles

4.6 FLOW FIELD VISUALIZATION WITH SHADOWGRAPHY

For qualitative visualization and quantitative measurement of flow field in fluidized bed a non-intrusive technique was used. Shadowgraphy with backlight imaging method was used for observation. Section 3.4 describes about shadow sizing technology. This technology capture shadow images of test section separated with time and finally those consecutive images are processed with commercial software DynamicStudio. This shadow sizing technology is suitable for low particle density region. Shadowgraphy was done for both spherical and non-spherical particles.

4.6.1 Shadow Sizing of Spherical Particles

1 mm spherical particles were used as test particles with 5.5 cm bed height. Two test sections were selected for this observation. One section was 21 cm above from top surface of test particles and the other one is just after top surface of test particles. Position 21 cm above from top surface of test particles was chosen to get dilute section with full fluidization. At full fluidization with higher gas velocity particles were trapped on the top mesh catch. At that regime images were taken to visualize the flow field and also to get quantitative measurements of particles flow. Figure 4.16 shows successive images were taken with triggering rate 1000 Hz.

Figure 4.16: Shadow Images for Spherical Particles in Dilute Section

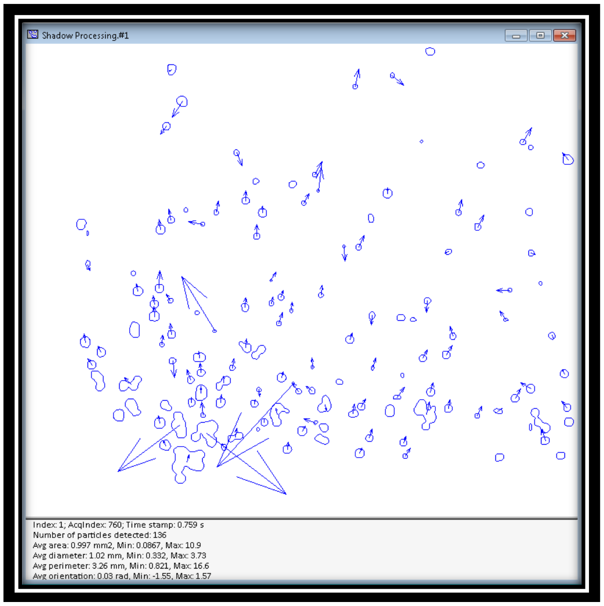

```
Index: 1; AcqIndex: 760; Time stamp: 0.759 s
Number of particles detected: 136
Avg area: 0.997 mm2, Min: 0.0867, Max: 10.9
Avg diameter: 1.02 mm, Min: 0.332, Max: 3.73
Avg perimeter: 3.26 mm, Min: 0.821, Max: 16.6
Avg orientation: 0.03 rad, Min: -1.55, Max: 1.57
```

Figure 4.17: Shadow Processed Results for Instantaneous Moment

Of thousands of images, three consecutive images are shown in figure 4.16. From these shadow images particles size, their instantaneous velocities were measured with shadow processing in DynamicStudio commercial software. Figure 4.17 shows the shadow processed results of the first image in figure 4.16. Figure 4.17 indicates particles contour with their mean diameter and velocity direction. 1 mm spherical particles were used as test particles and shadow processed result (figure 4.17) from a single double frame image shows the mean diameter 1.02 mm which indicates shadow sizing can detect particles exact size. A diameter statistics is also presented in figure from 64 shadow images in figure 4.18.

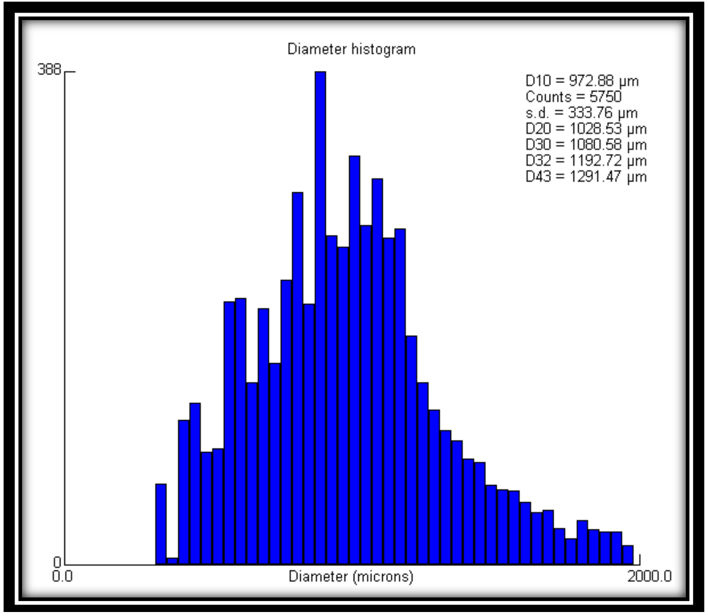

Figure 4.18: Diameter Statistics for Spherical Particles.

From figure 4.18 it has been found the mean diameter 972.88 µm with standard deviation 333 µm. While the images were taken the camera was focused in one plane. In image where the particles are out of focus they became blurred and show the diameter larger or smaller than the actual. But the amount of these blurred particles in results is less because when the intensity is less from blurred particles it will not count.

Particles are moving in horizontal and vertical directions. From numerical result of each shadow processed image it is possible to find out instantaneous average horizontal and vertical velocity magnitude. The average horizontal and vertical velocities of particles shown in figure 4.17 are 0.33 m/sec and 0.37 m/sec respectively.

Figure 4.19 also shows the size-velocity correlation from 62 shadow processed images.

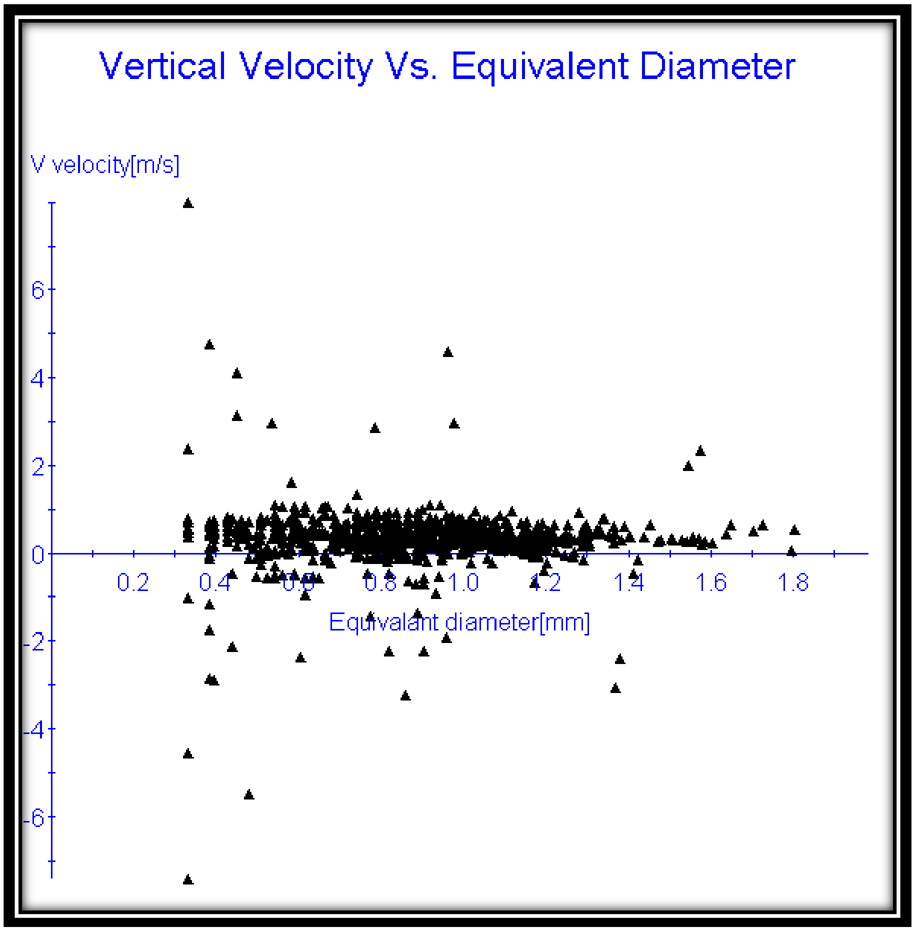

Figure 4.19: Vertical Velocities over Equivalent Diameter for Spherical

Figure 4.20 shows the particles velocity in vertical direction. Most of particles velocity region near 0.5 m/sec. Negative velocity indicates that particles are in downward direction. Figure 4.20 also shows the horizontal velocity correlation with size from 64 images. Figure 4.20 shows the particles velocities over percentage where it has been found over 42 percent particles have velocity 0.089 m/sec and over 40 percent particles have velocity 0.48 m/sec in vertical direction. Horizontal velocities over particle size are also in ranges 0.2 to 0.3 m/sec and the negative sign indicates the direction. Figure 4.21 shows the horizontal velocities over equivalent diameter. Figure 4.22 also shows the particle velocity over percentage. It has been found from figure 4.22 that over 61 percent particles have velocity 0.047 m/sec in horizontal direction.

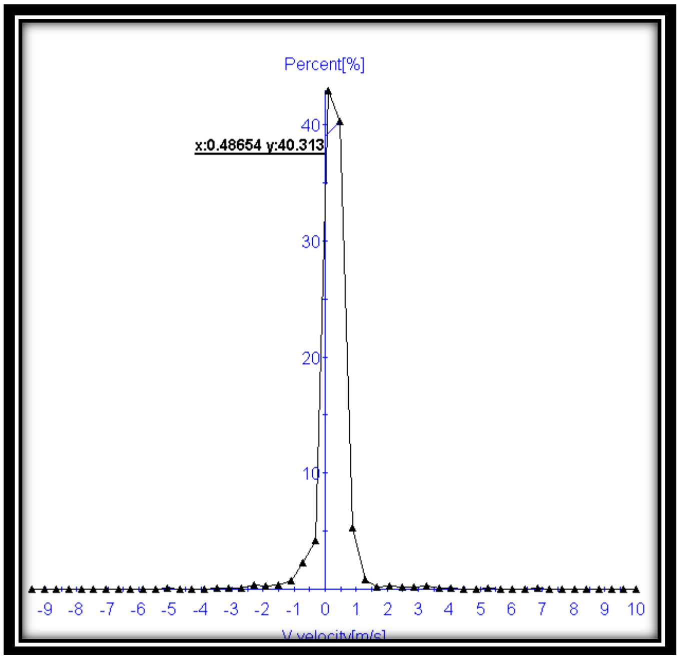

Figure 4.20: Vertical Velocity over Percentage.

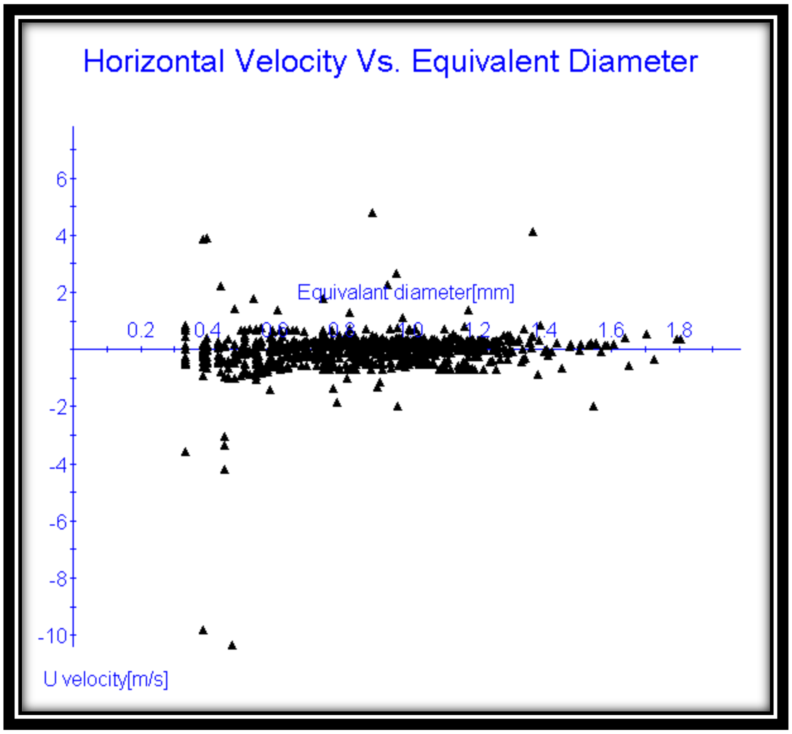

Figure 4.21: Horizontal Velocities over Equivalent Diameter for Spherical Particles

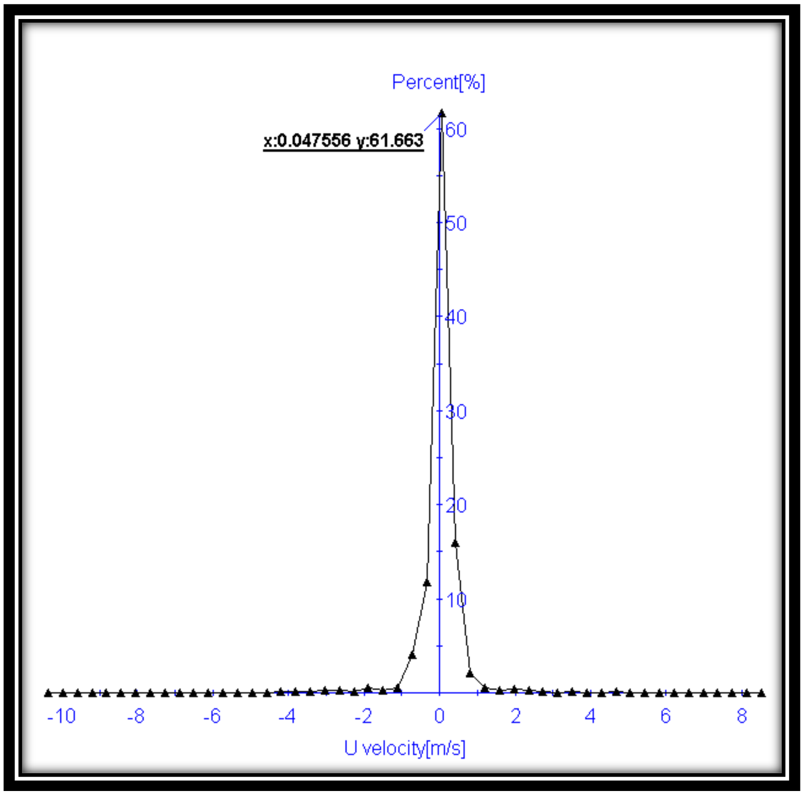

Figure 4.22: Horizontal Velocities over Percentage

4.6.2 Shadow Sizing of Non-Spherical Particles

850-1180 µm non-spherical particles with 1.01 mm nominal diameter were used as test particles. Calibration images were taken with same camera position, same focusing plane as used in spherical particles. Qualitative and quantitative measurements for non-spherical particles are presented in following figures.

Figure 4.23: Shadow Images of Non-Spherical Particles in Dilute Section

These shadow images were taken with 1000 Hz trigger rate same as used in spherical particles. Figure 4.23 shows three consecutive images with .002 sec interval. One single shadow processed image is also shown in figure 4.24 with their average mean diameter, particles contour and their velocity directions.

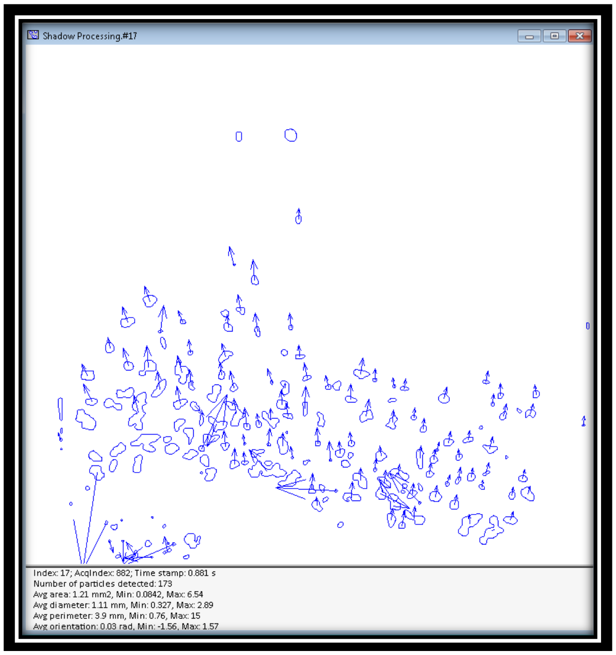

```
Index: 17; AcqIndex: 882; Time stamp: 0.881 s
Number of particles detected: 173
Avg area: 1.21 mm2, Min: 0.0842, Max: 6.54
Avg diameter: 1.11 mm, Min: 0.327, Max: 2.89
Avg perimeter: 3.9 mm, Min: 0.76, Max: 15
Avg orientation: 0.03 rad, Min: -1.56, Max: 1.57
```

Figure 4.24: Shadow Processed Results for Instantaneous Moment

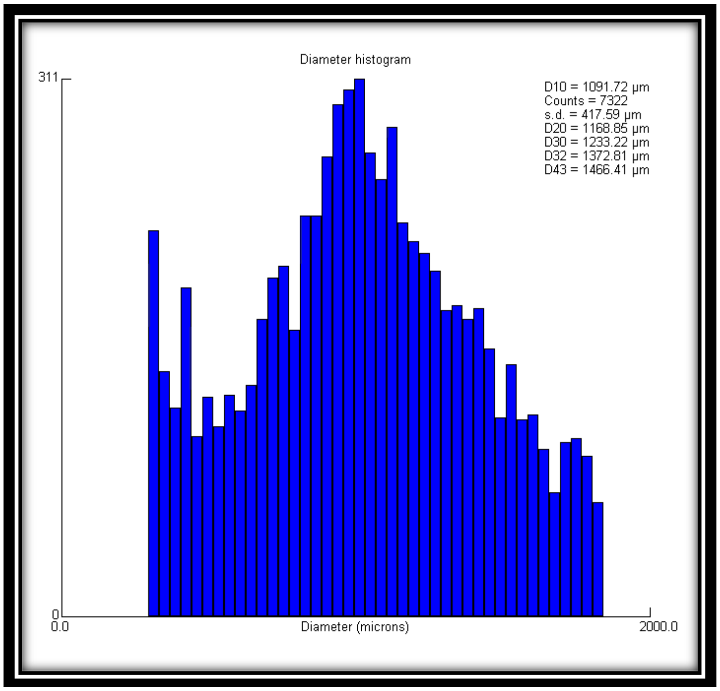

Figure 4.25: Diameter Histogram for Non-Spherical Particles

Figure 4.24 shows the shadow processed result of the third image in figure 4.21 with average mean diameter 1.11 mm. In this observation 850 -1180 μm non-spherical particles were used where the mean sieve diameter was 1.01 mm. A diameter statistics is also presented in figure 4.25. Figure 4.25 shows the diameter histogram for non-spherical particles resulting from 65 shadow processed images with particles counting, mean diameter 1091.72 μm and standard deviation 417.59 μm. Size-velocity correlation also found from shadow sizing. Figure 4.26 shows the vertical velocities over particles size.

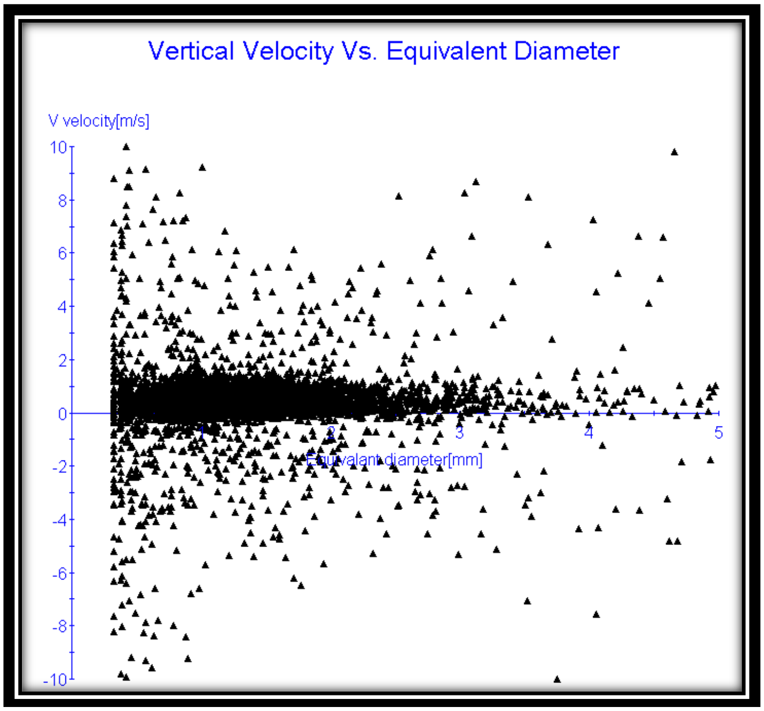

Figure 4.26: Vertical Velocities over Equivalent Diameter for Spherical

Most of the particles velocities ranges below 1 m/sec and negative velocities indicates downward direction of particles. Again more clear view will be found in figure 4.25 with velocities over percentage plot. From figure 4.27 it has found that over 46 percent particles have velocity 0.1872 m/sec in vertical direction. Figure 4.28 shows horizontal velocities over equivalent diameter and figure 4.27 shows velocities over percentage.

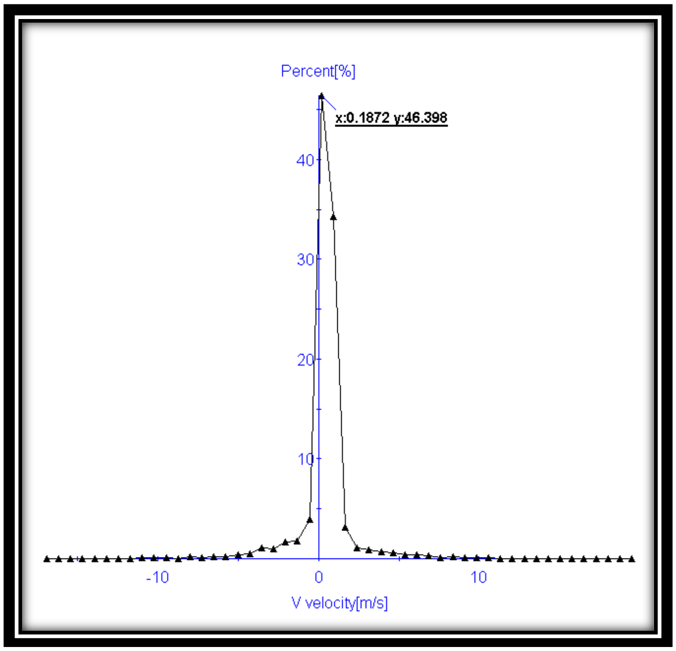

Figure 4.27: Vertical Velocities over Percentage.

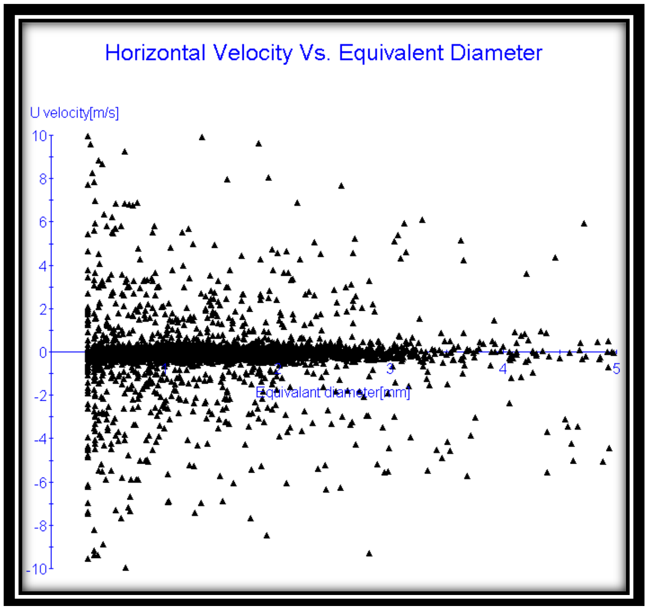

Figure 4.28: Horizontal Velocities over Equivalent Diameter for Non-Spherical Particles

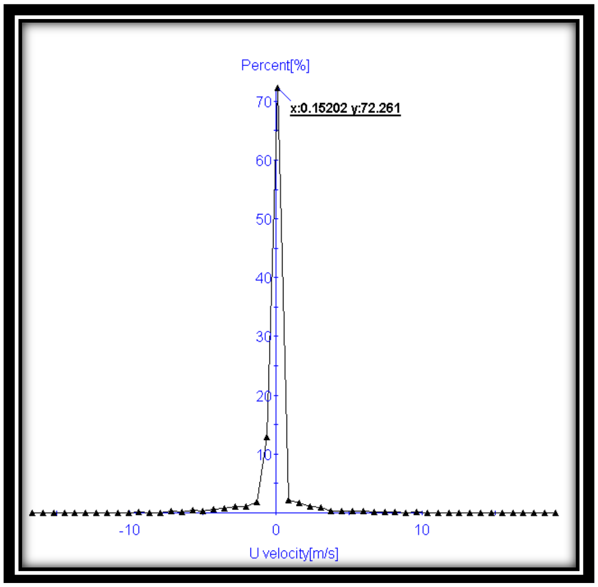

Figure 4.29: Vertical Velocities over Percentage for Non-Spherical

From figure 4.27 it has been found over 72 percent particles have velocity 0.15 m/sec in horizontal direction.

4.6.3 Bubble Collapsing in Bubbling Fluidization

After minimum fluidization with increased superficial gas velocities bubble appears at the bottom of bed, rises up and collapse for both spherical and non-spherical particles. Figure 4.30 and 4.31 shows the bubbles collapse for both spherical and non-spherical particles.

Figure 4.30: Bubble Collapsing for Spherical Particles

A bubble collapsing for spherical particles looks uniform. Before collapsing they form a half circle shape. Particles don’t scattered and they fall in a stream line. This happens because spherical particles are uniform in shape and they densely packed which prevent them to scatter while bubble collapse.

Figure 4.31: Bubble Collapsing for Non-Spherical Particles.

On the other hand when bubbles collapse in non-spherical particles they scattered randomly. Although at a moment bubbles seems like a half circle but latter the shape disappear and particles scattered. This is happen due to loosely packed. As non-spherical particles are irregular in shape they loosely packed in bed with much higher void fraction then spherical. Shadow processing of bubbles collapsing images is very hard as particles density is higher near bubbles. For shadow processing less density particles zone is required.

Chapter 5: Experimental Conclusions & Future Work

5.1 CONCLUSION

To observe hydrodynamic behavior of gas-solid fluidized beds, an investigation was done on a laboratory scale fluidized bed with different particle sizes and shapes. The laboratory fluidized bed was designed and constructed to investigate bed behavior pressure drop across the bed as measured with increasing superficial gas velocity. Pressure drops were measured for different bed height and particle size for different particle shapes. Insertion type flow meters and digital differential manometers were used with data loggers to measure flow rate and pressure drop, respectively. One mm spherical particles with different bed heights from 2 cm to 7 cm were tested. It was found that pressure drops increase with increasing superficial gas velocity until the particles are fixed into the bed. Pressured drop suddenly falls from its peak point and becomes constant with further increasing gas velocity. At the peak point, the pressure drop is equal the total weight of the particles. After this point and with increasing gas velocity, particles bonding collapse and pressure drop suddenly falls and also become constant. The same thing happens for each bed height. With measurement of each bed height plot together, it can be seen that bed pressure drop increases with increasing bed height. With increasing bed height particles, weight increase and bed pressure drop increase. On the other hand, from the plot it is clearly visible that minimum fluidization velocities remain constant with increasing bed height such that it indicates that minimum fluidization velocity is independent of bed height. Non-spherical particles were also used with different sizes ranges. The same measurements were taken with different bed height for all ranges. From pressure drop vs. superficial gas velocity plots, the results for spherical were similar. Pressure drop increases with increasing bed height and minimum fluidization velocity is independent of bed height. Minimum fluidization velocities remain constant with increasing bed heights. For changing particle size, minimum fluidization velocity and pressure drop decrease with decreasing particle size.

Experimental results were compared with theoretical results and the difference between theoretical and experimental found. High speed imaging was used to clarify the reason for this difference. Bed expansion and channeling right before minimum fluidization was found responsible for this difference. One mm spherical particles results for 3 different bed heights from laboratory scale fluidized bed were compared with another pilot scale fluidized bed with different bed diameter though same particle size and bed height thus isolating effect of bed diameter. It has been found that minimum fluidization decreases with decreasing bed diameter. Although in literature it has been found that minimum fluidization increases with decreasing bed diameter. Our bed geometry, particles parameter are different compared to literature and the larger size of particles used. A wide ranges of particle sizes and bed diameters are needed to make a correlation of minimum fluidization over bed diameter. A non-intrusive technology shadow sizing was used to visualize flow field for both spherical and non-spherical particles. With higher gas velocity at points where particles are trapped into the top mesh of bed column, shadow images were taken in regimes within the dilute section. Flow fields of instantaneous moment were found for spherical and non-spherical particles. Qualitative and quantitative were found with vertical and horizontal particle velocity. Shadow sizing technology was also used to observe bubble collapse. A difference was found during collapsing of bubbles between spherical and non-spherical particles due to variance in densely and loosely packed particles. Consolidated results are presented via a publication attached as an appendix.

5.2 FUTURE WORK

Only single particle density was considered whereas in the future particles with different density can be used to observe the effect of particle density over height and bed diameter. A cylindrical bed was used whereas different bed geometries like rectangular and cylindrical bed with conical shape bottom could be used to investigate bed hydrodynamics. Different ranges of particles with different sphericity ranges were categorized and stored in glass bottles. Shadow sizing technology can be used to measure the terminal velocity of free falling non-spherical particles per each particle range and each sphericity.

Chapter 6: Computational Modeling

6.1 IMPLEMENTATION OF DRAG MODEL INTO FLUENT AND MFIX

The computational model presented in this report was designed to test the ability of the newly proposed drag correlation to predict the hydrodynamic behavior of an actual gas-solid bed. The results from the new model are then compared to experimental data. The following sections highlight the theory and details of the computational domain used to compare the different models.

Governing Equations

In both Fluent and MFIX an Eulerian-Eulerian approach for both the fluid and the solid phase was considered for the simulations. Equations 6.1 through 4 represent the governing equations used to calculate the pressure and velocity components within a gas-solid bed. In these equations the subscript g denotes fluid (gas) and s the solid particle, ε is the volume fraction, τ is the stress tensor, and K_{drag} accounts for the momentum exchange between the fluid phase and the solid phase. Equations 6.2, 6.3 show the mass conservation equations for solid and gas flow while equations 6, 7 show the momentum conservation equations for the same flow field:

$$\frac{\partial}{\partial t}\left(\varepsilon_g \rho_g\right) + \nabla \cdot \left(\varepsilon_g \rho_g \vec{V}_g\right) = 0 \tag{6.1}$$

$$\frac{\partial}{\partial t}\left(\varepsilon_s \rho_s\right) + \nabla \cdot \left(\varepsilon_s \rho_s \vec{V}_s\right) = 0 \tag{6.2}$$

$$\frac{\partial}{\partial t}\left(\varepsilon_g \rho_g \vec{V}_g\right) + \nabla \cdot \left(\varepsilon_g \rho_g \vec{V}_g \vec{V}_g\right) = \nabla \cdot \bar{\bar{\tau}}_g - \varepsilon_g \nabla p + \varepsilon_g \rho_g \vec{g} - K_{drag}\left(\vec{V}_g - \vec{V}_s\right) \tag{6.3}$$

$$\frac{\partial}{\partial t}\left(\varepsilon_s \rho_s \vec{V}_s\right) + \nabla \cdot \left(\varepsilon_s \rho_s \vec{V}_s \vec{V}_s\right) = \nabla \cdot \bar{\bar{\tau}}_s - \varepsilon_s \nabla p - \nabla P_s + \varepsilon_s \rho_s \vec{g} + K_{drag}\left(\vec{V}_g - \vec{V}_s\right) \tag{6.4}$$

Here the gas phase stress tensor is calculated according to Newton's expression shown in Eq. (6.5).

$$\bar{\bar{\tau}}_g = \mu_g\left[\nabla \vec{V}_g + \nabla^T \vec{V}_g\right] - \frac{2}{3}\mu_g\left(\nabla \cdot \vec{V}_g\right)\bar{\bar{I}} \tag{6.5}$$

For the solid phase, the gradient of the particle pressure is represented by P_s and the particle phase stress tensor is given by equations 6.6, 7, respectively:

$$P_s = \rho_s \varepsilon_s \Theta_s + 2\rho_s \varepsilon_s^2 g_0 \Theta_s (1 + e_s) \tag{6.6}$$

$$\bar{\bar{\tau}}_s = \mu_s\left[\nabla \vec{V}_s + \nabla^T \vec{V}_s\right] + \left(\lambda_s - \frac{2}{3}\mu_s\right)\left(\nabla \cdot \vec{V}_s\right)\bar{\bar{I}} \tag{6.7}$$

Where e_s is the coefficient of restitution which was assumed as 0.9, g_o is the radial distribution function equation 6.8, and Θs is the granular temperature which is proportional to the kinetic energy of the fluctuating particle motion. The transport equation derived from kinetic theory is used to calculate the field of granular temperature. For the present model the granular temperature was initially set to a value of 1.0×10^{-5} $m^2 s^{-2}$.

$$g_0 = \left[1 - \left(\frac{\varepsilon_s}{\varepsilon_{s,max}}\right)^{1/3}\right]^{-1} \tag{6.8}$$

$$\frac{3}{2}\left[\frac{\partial}{\partial t}\left(\varepsilon_s \rho_s \Theta_s\right) + \nabla \cdot \left(\varepsilon_s \rho_s \vec{V}_s \Theta_s\right)\right] = \left(-P_s \bar{\bar{I}} + \bar{\bar{\tau}}_s\right) : \nabla \vec{V}_s + \nabla \cdot \left(\kappa_s \nabla \Theta_s\right) - \gamma_s + \Psi_{ls} \tag{6.9}$$

The maximum packing fraction ($\varepsilon_{s,max}$) was assumed to vary based on the sphericity of the particles used. The present model used values between 0.32 to 0.59 for different shapes. In equation 6.9, κ_s is the diffusion coefficient, γ_s is the collisional dissipation energy, and Ψ_{ls} represents the energy exchange between gas and solid phase. These are defined in equations 6.11 through 13:

$$\kappa_s = \frac{150\rho_s d_p\sqrt{\Theta_s\pi}}{384g_o(1+e_s)}\left[1+\frac{6}{5}g_o\varepsilon_s(1+\varepsilon_s)\right]^2 + 2\varepsilon_s^2\rho_s d_p g_o(1+e_s)\left(\frac{\Theta}{\pi}\right)^{1/2} \quad (6.11)$$

$$\gamma_s = 3(1-e_s^2)\rho_s\varepsilon_s^2 g_o\Theta_s\left[\frac{4}{d_p}\sqrt{\frac{\Theta_s}{\pi}} - \nabla\cdot\vec{V}_s\right] \quad (6.12)$$

$$\Psi_{ls} = -3K_{drag}\Theta_s \quad (6.13)$$

The solids stress tensor, equation 6.15, contains shear and bulk viscosities from particle momentum exchange due to translation and collision, equation 6.16:

$$\mu_s = \mu_{s,col} + \mu_{s,kin} \quad (6.14)$$

Where

$$\mu_{s,col} = \frac{4}{5}\varepsilon_s\rho_s d_p g_o(1+e_s)\left(\frac{\Theta_s}{\pi}\right)^{1/2} \quad (6.15)$$

and

$$\mu_{s,kin} = \frac{10\rho_s d_p\sqrt{\Theta\pi}}{96g_o(1+e_s)}\left[1+\frac{4}{5}(1+e_s)\varepsilon_s g_o\right]^2 \quad (6.16)$$

The solids bulk viscosity accounts for the resistance of the granular particles to compression and expansion, the relation is shown in equation 6.17:

$$\lambda_s = \frac{4}{3}\varepsilon_s^2\rho_s d_p g_o(1+e_s)\left(\frac{\Theta_s}{\pi}\right)^{1/2} \quad (6.17)$$

This report primarily focuses on the development of the momentum exchange (K_{drag}). Since the parameter K_{drag} depends on the drag coefficient for more dilute flows, it can be modeled a variety of ways. Some typical approximations used for the estimation of K_{drag} are shown in equations 6.18, 19.

$$K_{drag} = 150\frac{(1-\varepsilon_g)^2}{\varepsilon_g^2}\frac{\mu_g}{d_p^2} + 1.75(1-\varepsilon_g)\frac{\rho_g}{\varepsilon_g d_p}(\vec{V}_g - \vec{V}_s) \qquad \text{for} \quad \varepsilon_g \leq 0.8 \quad (6.18)$$

$$K_{drag} = \frac{3}{4}C_D\frac{(1-\varepsilon_g)\varepsilon_g}{d_p}\rho_g(\vec{V}_g - \vec{V}_s)\varepsilon_g^{-2.65} \qquad \text{for} \quad \varepsilon_g > 0.8 \quad (6.19)$$

For the current study equation 19 is modified to accommodate the newly developed C_D correlation and compared to experimental results. The modification was implemented through a user-defined function sub-routine in Ansys Fluent 14.0 code and through a DAT file in the MFIX code, both can be found in **Appendix B**.

6.2 COMPUTATIONAL DOMAIN

For the computational analysis a static bed height of 5.5 cm was selected to compare to experimental results. The fluid simulation domain consists of a three-dimensional system with the origin of the grid centered at the center of the column. A grid independence test was conducted and was determined that the grid of 35420 cells was optimal for the analysis. The working fluid was selected as isothermal air at 25 ˚C. The gas velocity was varied for each simulation run from 0 - 1 m/s in the axial direction in increments of 0.1 m/s, corresponding to experiments. The boundary conditions for the gas phase consist of no-slip, impermeable walls on the vertical sides of the bed. For the outflow boundary condition at the top of the bed, a pressure outlet set at atmospheric pressure is specified across the entire width. At the bed inlet, a velocity inlet boundary condition was specified. The developed model was then solved numerically using a finite volume technique in Fluent. The phase coupled SIMPLE algorithm was used to couple pressure and velocity and a first order upwind scheme used to solve for all terms.

Drag Correlation

The general form of the equation used to fit the data gathered from the individual particle measurements can be found in Eq. (6.20). In this equation A, B, C, and D are experimental constants found by minimizing the error from experimental and calculated values of drag coefficient. A non-linear least squares method was used in conjunction with Matlab to determine the coefficients.

$$\mathrm{C_D} = \frac{24}{\mathrm{Re}}(1 + \mathrm{ARe^B}) + \frac{\mathrm{C}}{1+\frac{\mathrm{D}}{\mathrm{Re}}} \tag{6.20}$$

The experimental coefficients were first determined for each particle sphericity. Table 1 presents some coefficients obtained after applying the values to curve fit Eq. (20) for different sphericity values. A simple least squares curve fit was then applied to these coefficients as a function of sphericity resulting in Equations (6.21 through 24).

Table 6.1: Experimental coefficients determined for different particle sphericities.

ϕ	A	B	C	D

0.47	1.95	0.006	0.95	-0.21
0.53	7.59	-0.16	0.84	1.58
0.58	1.17	0.001	1.12	-0.37
0.63	2.22	-0.002	1.02	-0.14
0.68	2.42	-0.013	0.88	0.72

$$A = \exp(-142.71 + 555.63\phi - 533.1\phi^2) \quad (6.21)$$

$$B = 0.2\phi - 0.15 \quad (6.22)$$

$$C = \exp(47.3 - 258.3\phi + 464.83\,\phi^2 - 275.72\phi^3) \quad (6.23)$$

$$D = \exp(-161.8 + 855.9\phi - 1502\phi^2 + 870.4\phi^3) \quad (6.24)$$

By substituting these four coefficients into Eq. (20) the expression for drag coefficient is obtained:

$$C_D = \frac{24}{Re}\left(1 + [\exp(-142.71 + 555.63\phi - 533.1\phi^2)]Re^{[0.2\phi - 0.15]}\right) + \frac{[\exp(47.3 - 258.3\phi + 464.83\,\phi^2 - 275.72\phi^3)]}{1 + \frac{[\exp(-161.8 + 855.9\phi - 1502\phi^2 + 870.4\phi^3)]}{Re}} \quad (6.25)$$

Drag Coefficient vs. Reynolds Number

The accuracy of the correlation to predict drag is plotted versus Reynolds number in figure 6.1. The model is compared to various others existing in literature and shows good agreement with experimental data. Although the authors believe that the relation can be used successfully up to a sphericity of 1, as shown in the next section, it is best suited for a sphericity range between 0.47 to 0.68 for a Reynolds number range between 2 and 10^3.

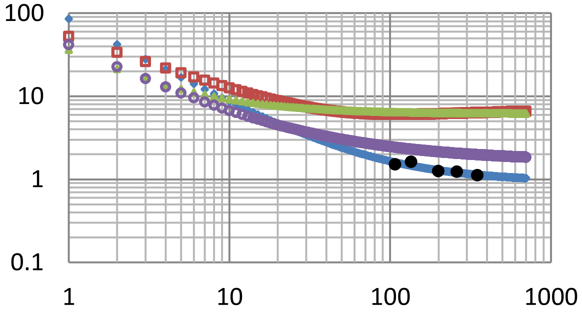

A

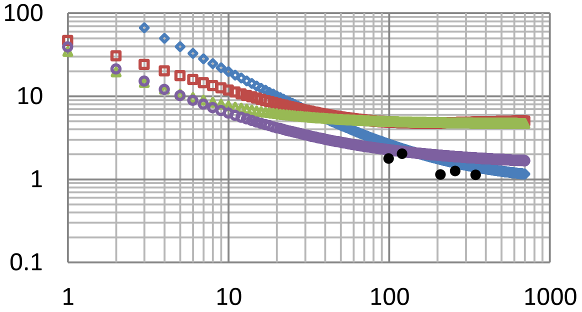

B

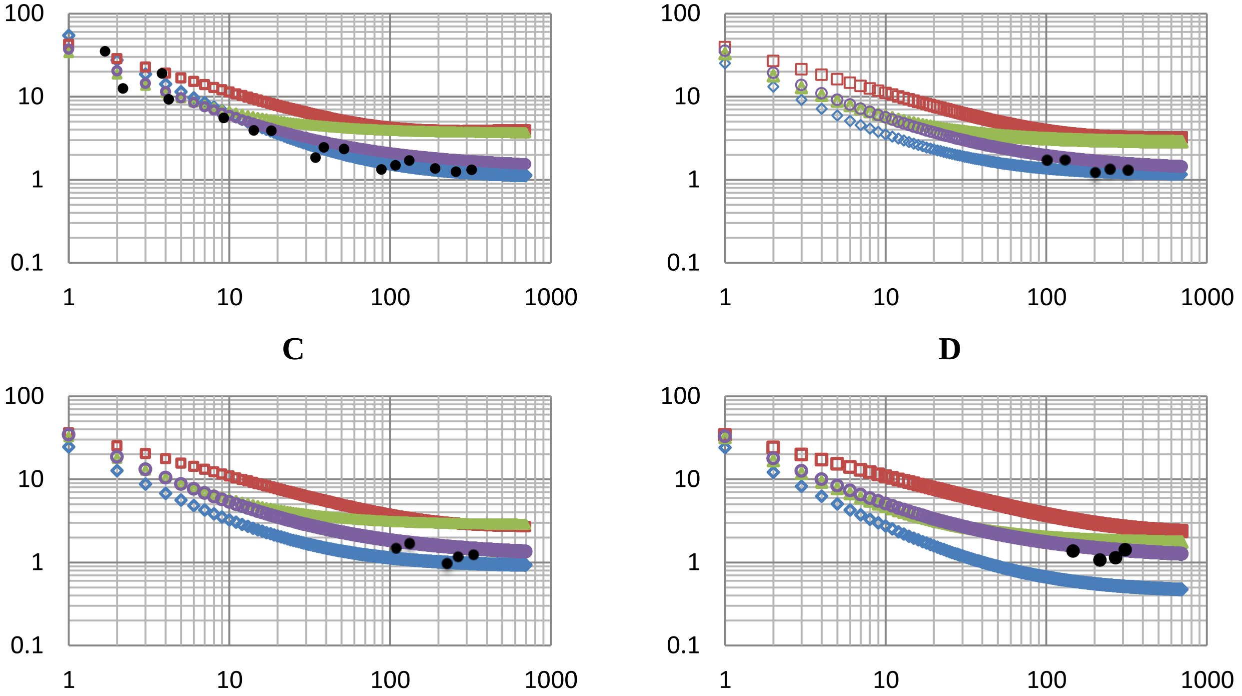

C

D

E

F

Figure 6.1: Plots of drag coefficient at various Reynolds numbers (<10^3) for different drag models including ○ = Holzer and Sommerfeld [3], □ = Haider and Levenspiel [15], Δ = Chien [26], and ◊ = newly proposed drag model. All are compared to experimental measurements ●. From top left values for sphericity (ϕ) are A) 0.475, B) 0.53, C) 0.58, D) 0.63, E) 0.68 and F) 0.73

6.3 MODEL PREDICTION OF GAS-SOLID BED HYDRODYNAMIC BEHAVIOR IN FLUENT

The model that is produced using the experimental data was first implemented in Fluent. Simulations were done for particles for three different sphericities: 0.50, 0.65 and 0.90 for a 5.5 cm bed height. This range was selected to observe the predictive behavior of the drag relationship within and outside of the tested range. The maximum percent of deviation of the simulation result from the experimental result for the sphericity of 0.50 was 11.82%, 11.39% for a 0.65 sphericity, and 9.75% for a sphericity of 0.90. The percent of deviation was within experimental uncertainty and shows considerable improvement on other models used for spherical models. Since this model incorporates sphericity, fluidized bed predictions of pressure drop and solids volume fraction are predicted with enhanced accuracy. For these models the size of time step input into the model had a significant effect on the simulation result.

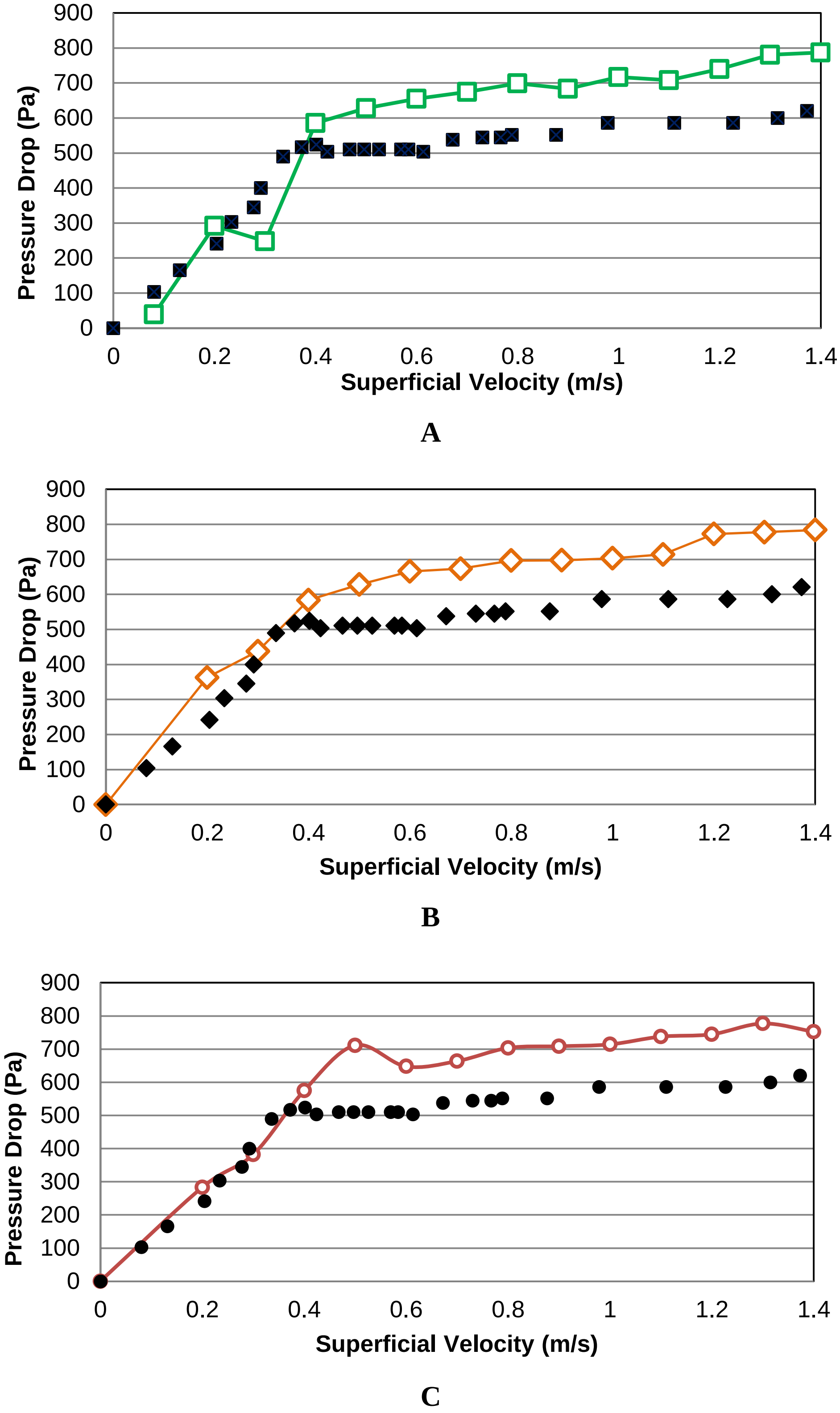

A

B

C

Figure 6.2: Comparison of Pressure Drop versus superficial velocity using new drag model for different sphericities of A) 0.5, B) 0.65, and C) 0.90 in Fluent.

6.4 COMPARISON OF FLUENT TO MFIX

This section presents the results from Fluent and MFIX and a comparison between the two codes. **Appendix B** shows an example sub-routine implemented into MFIX incorporating the drag model to predict pressure drop for different superficial velocities.

A set of simulations was performed with the same boundary conditions described previously in order to obtain results and predictions for non-spherical particles in MFIX. The pressure drop variation inside the bed as the superficial gas velocity increases using the new drag model presented earlier is shown in figure 6.3, where both numerical values for experiments and MFIX are compared. The plot describes a typical fluidized bed behavior. A linear increase of pressure with respect to superficial velocity is seen, also the pressure drop reaches a maximum pressure drop value, furthermore, this pressure drop value remains near continuous showing a relative linear trend with increasing gas velocity once the fluidization point has been reached.

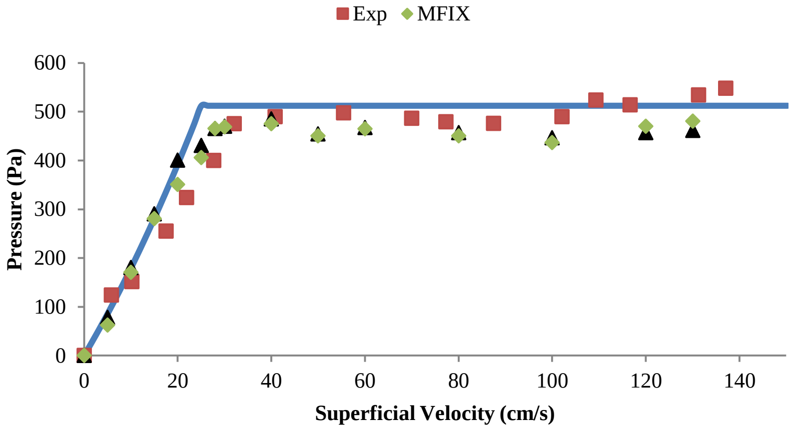

Figure 6.3: Non-spherical particles fluidization curves from simulation results

Table 6.2: Non-spherical numerical, theoretical and experimental results

FLUENT		
Drag Correlation	Min. Fluidization Velocity (cm/s)	Pressure Drop (Pa)
New Drag Model	31.0	480.2
MFIX		
Drag Correlation	Min. Fluidization Velocity (cm/s)	Pressure Drop (Pa)
New Drag Model	28.0	475.0

<table>
<tr><td colspan="4">THEORETICAL</td></tr>
<tr><td>Correlation</td><td>Min. Fluidization Velocity (cm/s)</td><td colspan="2">Pressure Drop (Pa)</td></tr>
<tr><td>Ergun</td><td>26.52</td><td colspan="2">512.0</td></tr>
<tr><td colspan="4">EXPERIMENTAL</td></tr>
<tr><td colspan="2">Min. Fluidization Velocity (cm/s)</td><td colspan="2">Pressure Drop (Pa)</td></tr>
<tr><td colspan="2">32.41</td><td colspan="2">476.0</td></tr>
</table>

In order to provide a more precise understanding about the fluidization hydrodynamics, instantaneous gas and solid flow contours were recorded from within Fluent and MFIX and compared. Flow fields of the axial component of gas velocity at simulated flow time of 1.5 s are given in figure 6.4 for spherical particles. Bubbling bed behavior is observed as the flow develops through the gas void between the solid particles, both codes show similar behavior. Also, the solid-phase velocity vectors are shown in figure 6.4 and a very good agreement between Fluent and MFIX and numerical results is appreciated. In addition, the figure below shows the solids volume fraction profile for inflow velocity of 75 cm/s at 1.5s simulation time, no significant pattern differences exist among the gas volume fraction contours shown in Fluent and MFIX. Numerical results of MFIX and Fluent are quite similar for both drag models. Lastly, the flow fields for non-spherical particles are shown in figure 6.5, good agreement is appreciated between Fluent and MFIX and non-spherical numerical results.

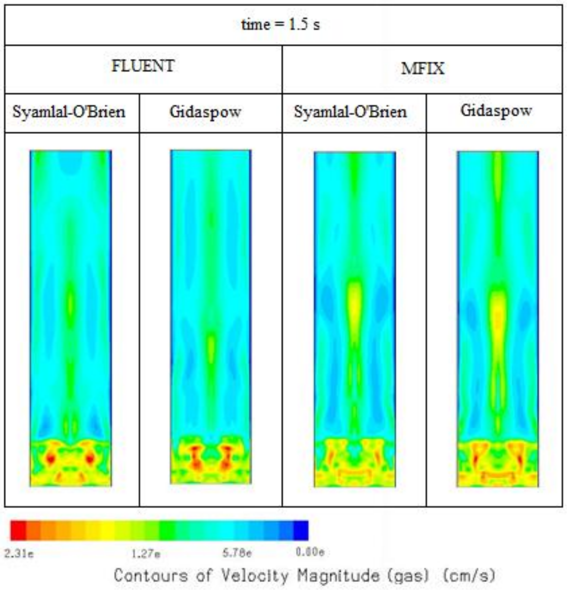

Figure 6.4: Snapshots of gas-axial velocity at 75 cm/s inflow velocity with spherical particles

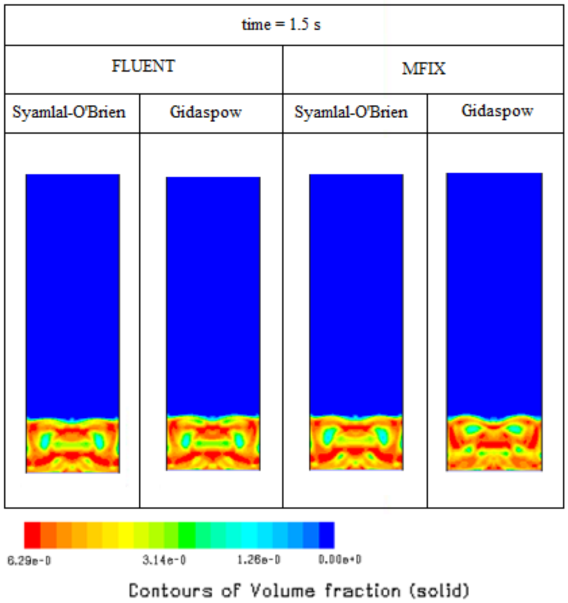

Figure 6.5: Snapshots of solid-phase vol. fraction for inflow velocity of 75 cm/s with spherical particles

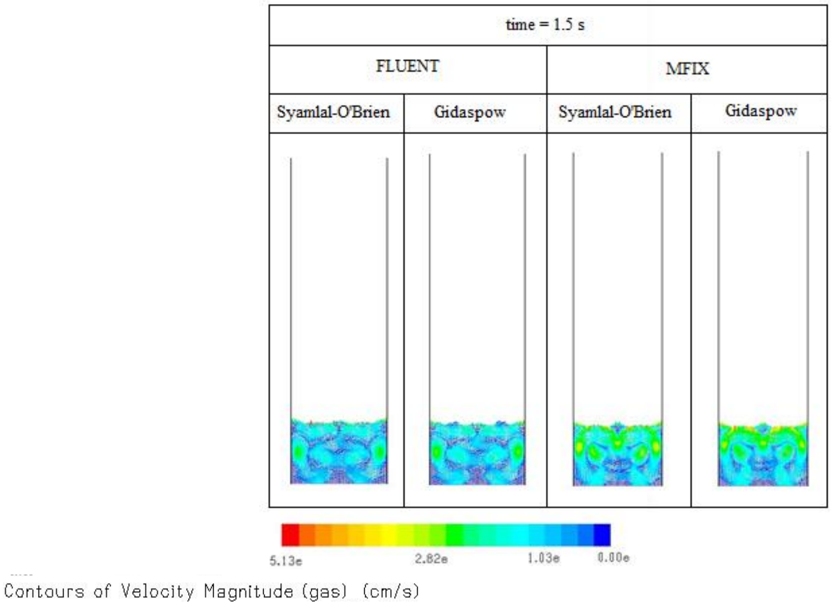

Figure 6.6: Snapshots of solids velocity vector-field for inflow velocity of 75 cm/s with spherical particles

The qualitative comparison is made in figure 6.7 by displaying some demonstrative snapshots from MFIX and compared with the experiment at different times. While in the numerical simulation snapshots is appreciated the development of colliding and collapsing bubbles as the gas is being increasingly supplied at the bottom of the bed, the colors red and light blue indicate the volume fraction of solids in the fluidization domain, being red a high fraction of solid particles, while blue is the presence of air voids and bubbles forming in the bed. The experimental snapshots present a similar bubbling behavior, showing a high accurate qualitative comparison with respect to the numerical simulations. In both experiment and simulation it is observed that, beginning from a well mixing state, a series of bubbles starting to form at the bottom of the bed and colliding at the top, the bubble formation increases with higher gas flow as time progresses. Realistic agreement between experiment and simulation can be obtained from this comparison.

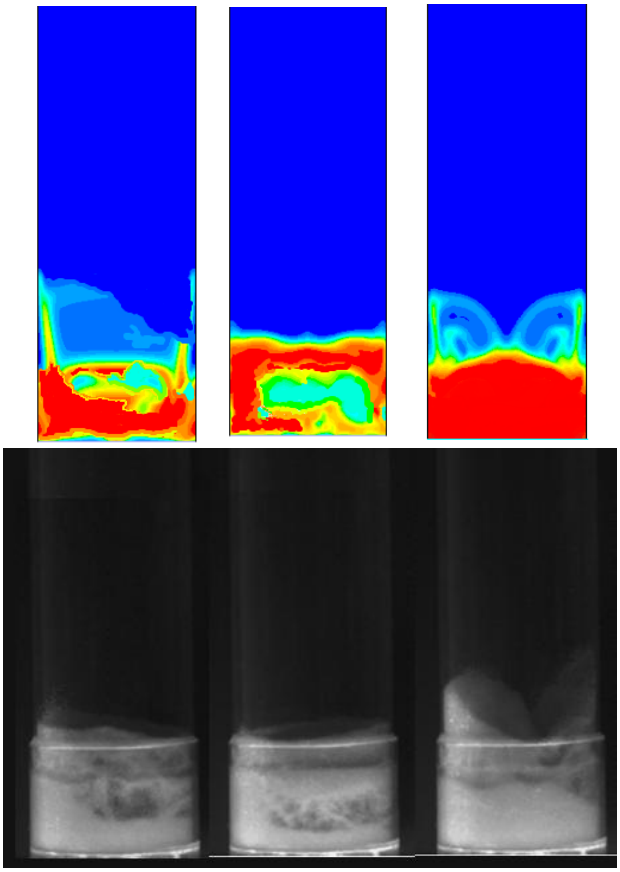

Figure 6.7: Comparison of snapshots of bubbling behavior of spherical particles among simulation (top row) and experiment (bottom row) at t= 2, 5, 7 s from left to right

BIBLIOGRAPHY

1. **Oka, Simon N.** *Fluidized Bed Combustion.* s.l. : Marcel Dekker, Inc, 2004. p. 1. ISBN: 0-8247-4699-6.

2. U.S. Department of Energy. *Gasification Technology R&D.* [Online] http://www.fossil.energy.gov/programs/powersystems/gasification/index.html.

3. Clean-Energy.US websit. *Clean Energy. US website http://www.clean-energy.us/facts/gasification.htm.* [Online] http://www.clean-energy.us/facts/gasification.htm.

4. Gasification Technologies Council. *http://www.clean-energy.us/index.htm.* [Online] http://www.gasification.org/page_1.asp?a=24&b=1&c=85.

5. "ZEEP". *Zero Emission Energy Plants.* [Online] http://www.zeep.com/zeep-technology/gasification-vs-combustion.php.

6. "Gasification". *Wikipedia, the free encyclopedia.* [Online] http://en.wikipedia.org/wiki/Gasification.

7. The National Energy Technology Laboratory (NETL). *The Energy Lab.* [Online] http://www.netl.doe.gov/technologies/coalpower/gasification/gasifipedia/4-gasifiers/index.html.

8. The National Energy Technology Laboratory (NETL) website. [Online] http://www.netl.doe.gov/technologies/coalpower/gasification/gasifipedia/4-gasifiers/4-1-1_fmb.html.

9. The National Energy Technology Laboratory (NETL) website. [Online] http://www.netl.doe.gov/technologies/coalpower/gasification/gasifipedia/4-gasifiers/4-1-2_entrainedflow.html.

10. The National Energy Technology Laboratory (NETL) website . [Online] http://www.netl.doe.gov/technologies/coalpower/gasification/gasifipedia/4-gasifiers/4-1-3_fluidizedbed.html.

11. **Crowe, Clayton T.** *Multiphase Flow Handbook.* Boca Raton, Florida : Taylor & Francis Group, 2006. 10:0-8493-1280-9.

12. **yang, Wen-Ching.** *Handbook of Fluidization and Fluid-Particle Systems.* New York : Marcel Dekker, Inc, 2003. ISBN: 0-8247-0259-X.

13. Outotec. *Outotec and More out of Ore.* [Online] 2007. http://www.outotec.com/36280.epibrw.

14. **Gidaspow, Dimitri.** *Multiphase Flow and Fluidization, Continuum and Kinetic Theory Descriptions.* 1994. ISBN 0-12-282470-9.

15. **Hetsroni, Gad.** *Handbook of Multiphase Systems.* s.l. : Hemisphere Publishing Corporation, 1982. ISBN 0-07-028460-1.

16. **Warren L. McCabe, Julian C. Smith, Peter Harriott.** *Unit Operations of Chemical Engineering.* New York : The Mcgraw-Hill Companies, Inc., 2005. ISBN 0-07-284823-5.

17. Ergun Equation. *Wikipedia, The Free Encycloedia.* [Online] April 2012. http://en.wikipedia.org/wiki/Ergun_equation.

18. *Experimental Study on the Effectice Particle Diameter of a Packed Bed with Non-Spherical Particles.* **Liangxing Li, Weimin Ma.** s.l. : Transp Porous Med(2011), 2011. DOI 10.1007/s11242-011-9757-2.

19. *The Expansion of Gas-Fluidized Beds in Bubbling Fluidization.* **D.J. Gunn, N. Hillal.** 16, s.l. : Chemical Engineering Science, 1997, Vol. 52, pp. 2811-2822.

20. *The Gas Fluidization of Large particles.* **D. Geldart, R. R. Cranfield.** s.l. : Chemical Engineering Journal, 1972, Vol. 3, pp. 211-231.

21. *Effect of Bed Diameter, Distributor and Inserts on Minimum Fluidization Velocity.* **N. Hilal, R.R. Ghannam, M.Z. Anaabtawi.** 2, s.l. : Chemical Engineering Technology, 2001, Vol. 24, pp. 161-165.

22. *Minimum Fluidization Velocities for Gas-Solid 2D Beds.* **G. Ramos, G. Ruiz, J.P. marques, G. Soler.** s.l. : Chemical Engineering and Processing, 2002, Vol. 41, pp. 760-764.
23. *Hydrodynamic Characteristics of Spout-Fluid Bed: Pressrue Drop and Minimum Spouting/Spout-Fluidization Velocity.* **W. Zhong, X. Chen, Z. Mingyao.** s.l. : Chemical Engineering Journal, 2006, Vol. 118, pp. 37-46.
24. *Minimum Fluidization velocities and Maximum Bed Pressure Drops for Gas-Solid Tapered Fluidized Beds.* **D.C. Sau, S. Mohanty, K.C. Biswal.** s.l. : Chemical Engineering Journal, 2007, Vol. 132, pp. 151-157.
25. *Fluidization of Biomass particles in a Gas-Solid Fluidized Bed.* **W. Zhon, B. Jin, Y. Zhang, X Wang and R Xiao.** s.l. : Energy and Fuels, 2008, Vol. 22, pp. 4170-4176.
26. *The effect of Column Diametr and Bed Height on Minimum Fluidization Velocity.* **A Rao, J. S. Curtis.** 9, s.l. : AIChE Journal, 2010, Vol. 56, pp. 2304-2311.
27. *Bed Height and Material Density Effects on Minimum Fluidizaiton Velocity in a Cylindrical Fluidized Bed.* **D. Escudero, J. Heindel.** Tampa, Florida : 7th International COnference on Muliphase Flow, 2010. Paper No. 1674.
28. *Particle Size Distribution Analysis of Coarse Aggregate Using Digital Image Processing.* **C.F. Mora, A.K.H. Kwan, H.C. Chan.** 6, s.l. : Elsevier Science Ltd, 1998, Cement and Concrete Research, Vol. 28, pp. 921-932.
29. *Measurement and Geological Significance of Shape and Roundness of Sedimentary particles.* **Krumbein, W.C.** s.l. : Journal of Sedimentary Petrology, 1941, Vol. 11, pp. 64-72.
30. *Volume, Shape and Roundness of Rock Particles.* **Wadell, Hakon.** 5, Chicago : The Jornal of Geology, 1932, Vol. 40, pp. 443-451.
31. *Modellig the internal Flow Structure of Circulating Fluidized Beds.* **Franco Berruti, Nicolas Kalogerakis.** 6, s.l. : The Canadian Journal of Chemical Engineering, 1989, Vol. 67, pp. 1010-1014.
32. Dantec Dynamics. [Online] 2012. http://www.dantecdynamics.com/Default.aspx?ID=1779.
33. **Anthony J. Wheeler, Ahmad R. Ganji.** *Introduction to Engineering Experimentation.* Third Edition. s.l. : Prentice Hall, 2010. ISBN 978-0-13-174276.5.
34. Standard Deviation. *Wikipedia, the free encyclopedia.* [Online] http://en.wikipedia.org/wiki/Standard_deviation.
35. t-distribution table. *Statistics How To.* [Online] http://www.statisticshowto.com/tables/t-distribution-table/.

Appendix A: Experimental Publication

Flow Field Visualization and Drag Analysis of Particles in a Gas-Solid Fluidized Bed

Md Rashedul H Sarker,[1] A S M Raufur R Chowdhury[1], Norman Love[2], Ahsan Choudhuri[3]
Center for Space Exploration and Technology Research (cSETR)
University of Texas at El Paso, El Paso, Texas 79968

In this work particle flow behaviors inside a gas-solid fluidized bed were documented. Spherical and non-spherical particles measuring 1 mm and 0.85-1.18 mm, respectively, were used as test particles. Flow structure, particles size, particle velocity were measured with shadowgraphy a non-intrusive technology. Also presented in this work is a drag model for non-spherical particles expressed in terms of particle sphericity and Reynolds number. The drag model presented here is applicable to a range between 0.48 to 0.68.

NOMENCLATURE

$\emptyset$ = Sphericity
d = Nominal diameter of non-spherical particles (mean sieve diameter)
a = Longest particle diameter
C_D = Drag coefficient
F_D = Drag force
ρ = Fluid density
A = Projected surface area of particles
Re = Reynolds number
ρ_s = Density of particle (borosilicate glass beads)
V_t = Terminal velocity of particles
g = Gravitational force
s = Surface of sphere having same volume of particles
S = Actual surface area of particles

I. INTRODUCTION

The biggest challenge facing the US in the 21st century is to provide sufficient energy while continuing to reduce unwanted pollutant emissions. One method of achieving this is through use of coal. Gasification of coal can provide the necessary energy, since the US has large supplies of the natural resource, with reduced emissions without sacrificing performance. The U.S. Department of Energy is emphasizing the development of advanced coal gasfiers with enhanced efficiency and reliability[1]. Currently further improvement of gas-solid fluidized bed performance is needed. These types of gasifiers, however, involve multiple scales, interaction of multiple phases, and are difficult to access when operated[2]. Many efforts have been undertaken to characterize gas-solid flows, however, they are still poorly understood [3, 4]. Based on the needs of the field, the purpose of this project is to provide documentation on the translational and rotational motion of spherical and non-spherical particles inside an operational fluidized bed for future computational and experimental design efforts.

Numerous investigations have been done with high-speed imaging to better understand the flow structure in a fluidized bed. Delgado, et al[5], observed ascending bubbles and granular velocity with three different non-intrusive techniques by high speed camera in a dense 2-D fluidized bed. They characterized bubble paths by time-average concentration and bubble velocities were measured by tracking algorithm over the mass center of bubbles. This study also characterized particle velocity with particle image velocimetry (PIV). Lackermeier et al[6] used a pilot scale circulating fluidized bed to visualize flow structure in

---

[1] Graduate Research Assistant, Student Member AIAA
[2] Assistant Professor, Member AIAA
[3] Director cSETR and Professor, Senior Member AIAA

upper dilute section where cross-sectional average solids volume concentration varied from 0.1 to 1 vol. %. They used a high-speed video technique with a laser sheet technique and endoscope to guide the laser light into fluidized bed. They also developed a model to estimate how solid particle properties influence operating conditions between received and emitted light intensity. Hatano et al[7] developed a particle image scope for microscope observation of solid particles (coarse sand particles and fine sand particles) in circulating fluidized beds. With the help of image fibers and video system they were able to detect particles shape, number of particles and by adjusting the exposure time of a 35 mm camera they were also able to determine the velocity of particles. Jimenez et al[8] used digital image analysis (DIA) and PIV both in 0.005 m thickness gas-solid fluidized bed to ensure two dimensional flows. They examined the bubble hydrodynamics along with time averaged dense phase velocity of vertical and horizontal component. Laverman et al[9] experimentally investigated the hydrodynamics of freely bubbling with particle image velocimetry (PIV) along with digital image analysis (DIA) for different aspect ratios at different superficial gas velocities. They were able to get bubble behavior and emulsion phase for these two non-intrusive measuring techniques. Sathe et al[10] estimated time average flow structure and flow pattern of bubble columns using particle image velocimetry and miniature pressure sensor. They collected their data with miniature pressure sensors, PIV, shadowgraphy and LDA to propose a methodology of getting better insight of dynamics of flow structures. In our current paper when the superficial gas velocity is higher than minimum fluidization velocity an attempt has been taken to visualize particles instantaneous velocity using shadowgraphy technology along with a high-speed camera and backlit LED light source.

Another component of this study involves characterizing non-spherical particle drag behaviors. Fluidization behavior of feedstock particles, such as coal or biomass, inside gas-solid fluidized bed varies while they interact with the flowing fluid. Drag force between moving particles and the fluid plays an important role. Feedstock particles in the fluidized bed are commonly non-spherical. The behavior of these non-spherical particles can be obtained by the knowledge of drag force acting between particles and fluid and their falling velocity. The relation between drag coefficient and Reynolds number are graphically available in literature. However, available drag relationships are not accurate because of a lack of data for a wide range of particle geometries[11]. Furthermore, most of the correlations used are for spherical shaped particles falling at their terminal velocity. Little information has been found in literature for non-spherical particles. A list of different correlations is listed below in Table 1 which is summarized from studies from Khan et al[12], Haider et al[13], Syamlal et al[14] and Gadaspow et al[15]. Tran-Cong et al[16] also proposed an empirical correlation for drag coefficient from experimentally measured data of six different shapes of sphere particles. This paper will use the measured flow velocities from the shadowgraphy technique and other experimental data to develop a new drag coefficient relation for use of modeling of non-spherical particles with different sphericities.

III. EXPERIMENTAL SETUP AND METHODOLOGY

A laboratory scale fluidized bed with a 12.4 cm inner diameter was designed and constructed with a 53µm mesh which was placed in the bottom of the fluidized bed to hold the test particles in place. A blower was used to supply air through a duct to the test section. A butterfly valve was used to control the flow rate. Bed pressure drop was measured for increasing airflow rates with an insertion type flow meter and digital differential manometer. Figure 1 shows an image of laboratory scale fluidized bed. For spherical test particles 1 mm borosilicate spherical glass beads were used. For non-spherical particles 6 mm spherical borosilicate glass beads were crushed in hydraulic compressor and sieved in a sieve shaker to produce non-spherical particles. Different range sieve plates were used to accumulate non-spherical particles ranges from 20-2000 µm. Figure 2 shows hydraulic compressor and sieve shaker.

To visualize the flow field and measure particles instantaneous velocity a backlight source coupled with 500 kHz high-speed camera were used. Figure 3 shows a digital image of the shadowgraphy setup. Shadowgraphy images were taken for both spherical and non-spherical particles at a 5.5 cm bed height. The test section were images were taken was 21cm above the top of fixed bed surface at flow velocities above the minimum fluidization velocity. This area was selected because of the dilute number of particles which is required for accurate shadow imaging. Qualitative and quantitative measurements of flow-field were taken for both spherical and non-spherical particles.

Table 1: Drag correlations available in literature[12-16]

Year	Author	Correlation
1948	Dallavale	$C_D = \left(0.63 + 4.8\,\mathbf{Re}_p^{-0.5}\right)^2$
1972	Ihme et al.	$C_D = 24/\mathbf{Re}_p + 5.48\,\mathbf{Re}_p^{-0.573} + 0.36$
1978	Clift et. Al	$C_D = \frac{24}{R} + \frac{3}{16}$ $C_D = \frac{24}{R}[1 + 0.1315R^{(0.82-0.05w)}]$ $C_D = \frac{24}{R}[1 + 0.1935R^{0.6305}]$ $\log C_D = 1.6435 - 1.1242w + 0.1558w^2$ $\log C_D = -2.4571 + 2.5558w - 0.9295w^2 + 0.1049w^3$ $\log C_D = -1.9181 + 0.6370w - 0.0636w^2$ $\log C_D = -4.3390 + 1.5809w - 0.1546w^2$ where $w = \log R$
1986	Flammer and Banks	$C_D = \frac{24}{R} 10^E$ where $E = 0.261R^{0.369} - 0.105R^{0.431} - \frac{0.124}{1 + (\log R)^2}$
1986	Turton and Levenspiel	$C_D = \frac{24}{R}(1 + 0.173R^{0.657}) + \frac{0.413}{1 + 16{,}300R^{-1.09}}$
1987	Khan and Richardson	$C_D = (2.25R^{-0.31} + 0.36R^{0.06})^{3.45}$
1989	Haider and Levenspiel	For Spherical $u_* = \left(\frac{4}{3}\frac{Re}{C_D}\right)^{\frac{1}{3}} = U_T\left[\frac{\rho_f^2}{g\mu(\rho_s - \rho_f)}\right]^{\frac{1}{3}}$ $d_* = \left(\frac{4}{3}C_D Re^2\right)^{\frac{1}{3}} = d\left[\frac{g\rho_f(\rho_s - \rho_f)}{\mu^2}\right]^{\frac{1}{3}}$ $u_* = \left[\frac{18}{d_*^2} + \frac{0.5909}{d_*^{0.5}}\right]^{-1}$ $C_D = \frac{24}{Re}(1 + 0.1806Re^{0.6459}) + \frac{0.4251}{1 + \frac{6880.95}{Re}}$ For non-spherical $C_D = \frac{24}{Re}[1 + 8.1716\exp(-4.0655\,\emptyset)]Re^{0.0964 + 0.5565\emptyset} + \frac{73.69\,Re\exp(-5.748\,\emptyset)}{Re + 5.378\exp(6.2122\,\emptyset)}$
1989	Syamlal and O'brien	$F_{gs} = \frac{3\varepsilon_s\varepsilon_g\rho_g}{4U_T^2 d_p} C_{D-sphere}\lvert\vec{v_s} - \vec{v_g}\rvert$
1992	Gidaspow	$F_{gs} = \begin{cases} \frac{3}{4}C_{D-sphere}\frac{\rho_g\varepsilon_g\varepsilon_s\lvert\vec{v_s} - \vec{v_g}\rvert}{d_p}\varepsilon_g^{-2.65}, & \varepsilon_g \geq 0.8 \\ \frac{150\varepsilon_s(1 - \varepsilon_g)\mu_g}{\varepsilon_g d_p^2} + \frac{1.25\rho_g\varepsilon_s\lvert\vec{v_s} - \vec{v_g}\rvert}{d_p}, & \varepsilon_g < 0.8 \end{cases}$ Where, $C_{D-sphere} = \frac{24}{Re}(1 + 0.15Re^{0.687})$ $= 0.44$

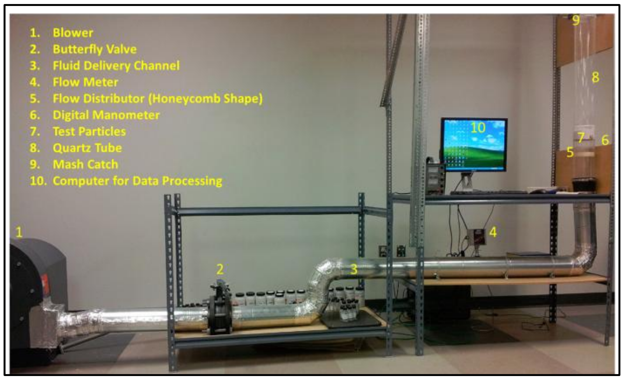

Figure 1: Laboratory scale gas-solid fluidized bed

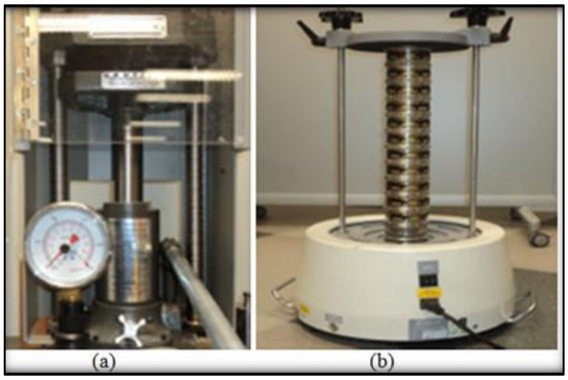

Figure 2: (a) Hydraulic press (b) Sieve shaker

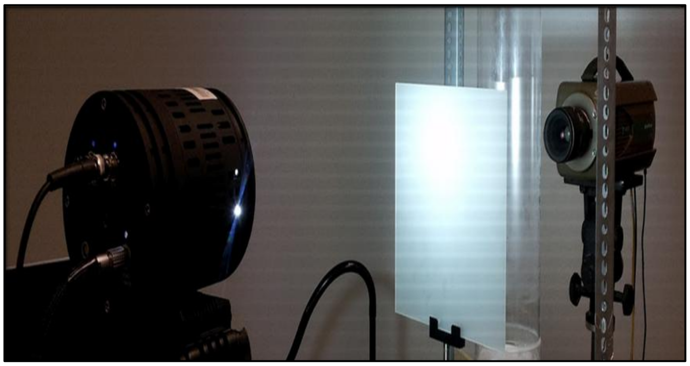

Figure 3: Shadowgraphy experimental setup

For drag correlation measurements the terminal velocity of different particle sizes and sphericities is required. Figure 4 shows schematic and digital image of the experimental setup for terminal velocity measurements. The terminal velocity of every particle size was calculated to get the required height to reach the particle in terminal velocity.

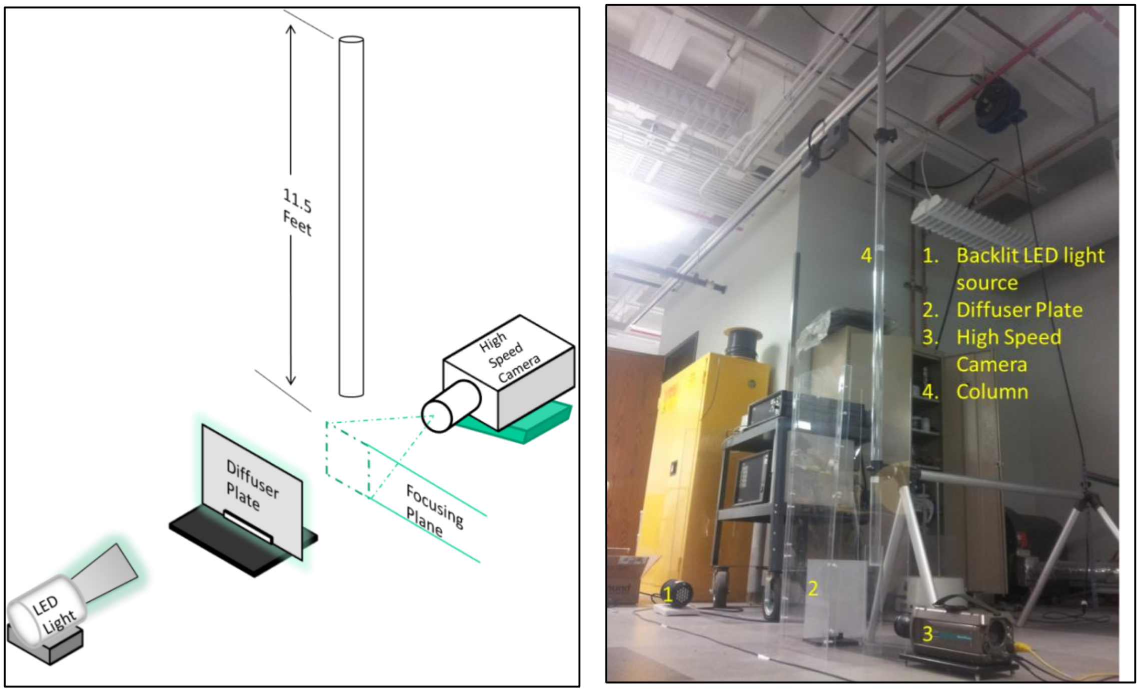

Figure 4: Schematic and real time image of experimental setup for terminal velocity measurement of particles

Particles were dropped from top of the column and allowed to free-fall through air at ambient conditions. Each particle reached its terminal velocity before passing through the camera-focusing plane. Before taking image of falling particle the focusing plane was calibrated with metric scale to convert pixels to lengths. Falling particles images were taken with the high-speed camera set at 2.229 kHz.

A. Sphericity

For particle characterization size and shape analysis is very important. Digital Image Processing (DIP) technology was used for size and shape analysis[17]. For our current application to measure sphericity of particles the digital images of particles were used to determine the largest diameter circle that circumscribed the entire particle by using a DinoLite digital microscope. W.C. Krumbein[18] describes the expression for sphericity also used by Hakon Wadell[19] . According to Wadell's definition of sphericity ($\emptyset$) is as follows,

$$\emptyset = \sqrt[3]{\frac{Volume\ of\ Particle}{Volume\ of\ the\ Circumscribe\ Sphere}} \quad (1)$$

Here from Wadell's expression, the particle volume has the same volume in terms of a sphere and the diameter is the nominal diameter of the particle (d). From this expression the basic volume of particle is $\frac{\pi}{6}d^3$. In general, the volume of circumscribed sphere has the longest diameter (a) of the particle, so the volume of circumscribed sphere is $\frac{\pi}{6}a^3$. From these values the Wadell's expression for sphericity is as follows:

$$\emptyset = \sqrt[3]{\frac{Volume\ of\ Particle}{Volume\ of\ the\ Circumscribe\ Sphere}} = \sqrt[3]{\frac{\frac{\pi}{6}d^3}{\frac{\pi}{6}a^3}} = \frac{d}{a} \quad (2)$$

Sphericity was measured for 5 different particle ranges between 500-1180µm and they are categorized with 9 different sphericity ranges between 0.45-0.90. Thirteen more particle ranges were also considered below 500 µm ranging between 53-500 µm. Sphericity of particles below 500 µm were considered as 0.58 and crushed glass particles sphericity 0.6 [20] .

B. Drag Coefficient and Terminal Velocity

The drag coefficient is a dimensionless term which refers to drag force between an object and fluid. Drag coefficient is not a constant value and depends of particle size, particles falling orientation, fluid density, and viscosity. Drag coefficients were used to define drag force exerted on an object in direction relative to the fluid flow. Most applications of settling behavior of various shaped particles has a fundamental importance and in most applications measurement of terminal velocity has interest for design, optimization of process equipment[16]. Drag coefficient is defined as follows:

$$C_D = \frac{F_D}{\frac{1}{2}\rho u^2 A} \tag{3}$$

Previous studies on drag force have mainly focused on the use of spherical particles. However, in applications of transport of particles they are mostly non-spherical. Thus it is necessary to have scrutinized information of drag force acting on non-spherical particles to simulate their motions. Many researchers collected numerous experimental information for variously shaped particles and proposed their model for different ranges of Reynolds number. Chhabra et al[21] explained some approaches of drag modeling from previous studies. Some studies involve drag expressions with fixed shapes and orientations. Haider and Levenspiel[13] developed a drag expression for spherical and non-spherical particles based on the geometry and terminal velocity of the particle[21]. The general form of the equation used in Haider and Levenspiel will also be used for the particles found in this study, Eq. (4).

$$C_D = \frac{24}{R_e}(1 + AR_e^B) + \frac{C}{1 + \frac{D}{R_e}} \tag{4}$$

Here A, B, C, and D are experimental constants found by minimizing the error from experimental and calculated values of drag coefficient. As part of this paper the experimental constants in Eq. (4) were determined based on experimentally measured free falling terminal velocity of different sphericity particles. Tentative terminal velocities were calculated for different particle sizes from following expression considering C_D for a symmetric shape and required height for each particle size at where they reach terminal velocity, Eq. (5).

$$V_t = \sqrt{\frac{4gd}{3C_d}\left(\frac{\rho_s - \rho}{\rho}\right)} \tag{5}$$

From this the required height at which particle will reach terminal velocity and experimentally determined drag acting on the particle could be determined by measuring the velocity for an individual falling particle with the high-speed camera.

IV. RESULTS AND DISCUSSION

This section presents the experimental results of high-speed flow visualization for both spherical and non-spherical particles using the shadowgraphy technique. This section also presents a drag coefficient expression based on experimental data which is a function of Reynolds number and sphericity of the non-spherical particles.

A. Spherical and Non-Spherical Particles:

1 mm spherical particles and 850-1180μm non-spherical particles were separately used as test particles at a 5.5cm bed height. The test section for high-speed imaging was taken at 21 cm above from the top surface of test particles. Calibration images were taken at same camera position, same focusing plane for both spherical and non-spherical particles. At full fluidization images were taken to visualize flow field and also to get qualitative and quantitative measurements of particles motion. Figure 5 and 6 shows three consecutive sample images of spherical and non-spherical particles.

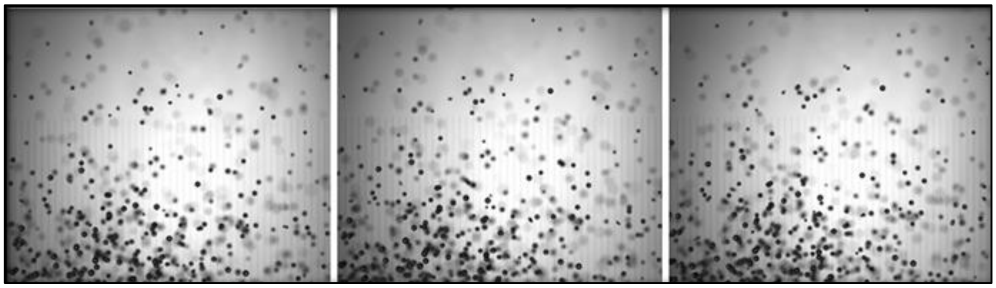

Figure 5: Shadow images for spherical particles in dilute section

Figure 6: Shadow images for non-spherical particles in dilute section

Figure 7 shows the resulting shadow processed image of one single sample image from Figures 5 and 6.

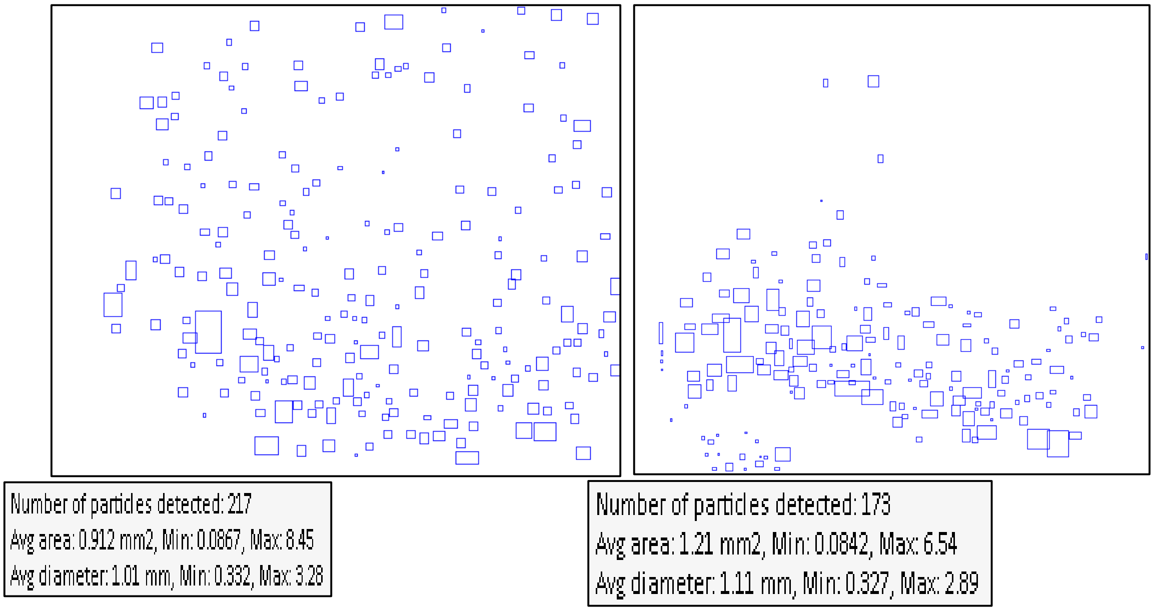

Number of particles detected: 217
Avg area: 0.912 mm2, Min: 0.0867, Max: 8.45
Avg diameter: 1.01 mm, Min: 0.332, Max: 3.28

Number of particles detected: 173
Avg area: 1.21 mm2, Min: 0.0842, Max: 6.54
Avg diameter: 1.11 mm, Min: 0.327, Max: 2.89

Figure 7: Shadow processed image of particles tracking for spherical and non-spherical particles

From two consecutive shadow images particle velocity was measured. Figure 8 shows particle velocity vectors at an instantaneous moment. Longer arrows in the image indicate higher velocities.

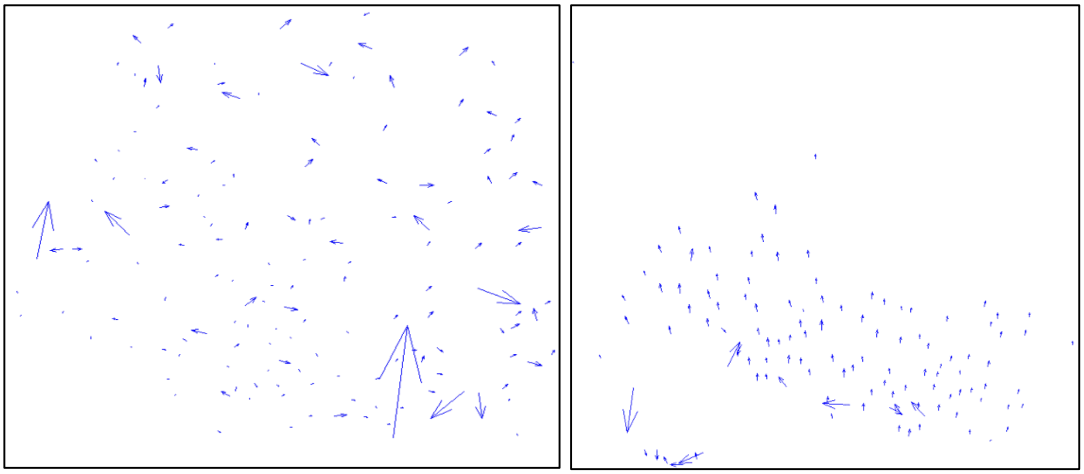

Spherical

Non-Spherical

Figure 8: Particles velocity vectors for an instantaneous moment

Superficial gas velocities were 2.11 m/s for spherical particles and the average velocity for all particles for the instantaneous moment shown was 0.26 m/s. Superficial gas velocity of non-spherical particles was 1.06 m/s and the average velocity of all non-spherical particles at that instantaneous moment was 0.88 m/s.

B. Drag Coefficient

The experimental constants A, B, C and D shown in Eq. (4) were determined by using a non-linear least square method used to fit the data. The following table shows the results from the analysis.

Table 2: Values of parameters used in Eq. (4) for different sphericities to predict C_D

ϕ	A	B	C	D
0.47	1.9484	0.0062	0.9481	-0.2085
0.53	7.5902	-0.1573	0.8352	1.5798
0.58	1.1728	0.0011	1.117	-0.3684
0.63	2.2173	-0.0017	1.0178	-0.1354
0.68	2.419	-0.0134	0.8776	0.7191

Functionality between the parameters and sphericity has been established using a polynomial equation fitting the data from Table 2. The following four equations have been determined based on this data:

$$\mathrm{A} = \exp(-142.7123 + 555.6297\emptyset - 533.0938\emptyset^2) \tag{6a}$$

$$\mathrm{B} = 0.2004\emptyset - 0.1489 \tag{6b}$$

$$\mathrm{C} = \exp(47.3143 - 258.3263\emptyset + 464.8296\emptyset^2 - 275.7239\emptyset^3) \tag{6c}$$

$$\mathrm{D} = \exp(-161.8 + 855.9\emptyset - 1502\emptyset^2 + 870.4\emptyset^3) \tag{6d}$$

By substituting these four values in Eq. (4) the expression for drag coefficient was obtained and is presented in Eq. (7):

$$\mathrm{C_D} = \frac{24}{\mathrm{R_e}}\left[1 + \exp[-142.7123 + 555.6297\emptyset - 533.0938\emptyset^2]\mathrm{R_e}^{(0.2004\emptyset - 0.1489)}\right] + \frac{\exp(47.3143 - 258.3263\emptyset + 464.829\emptyset^2 - 275.72369\emptyset^3)}{1 + \frac{\exp(-161.8 + 855.9\emptyset - 1502\emptyset^2 + 870.4\emptyset^3)}{\mathrm{R_e}}} \tag{7}$$

Equation (7) can predict drag coefficient (C_D) over various Reynolds numbers and sphericities ranging from 0.43 to 0.68. Figure 9 shows the plots of drag coefficient versus Reynolds number for different sphericities of free falling non-spherical particles. From Figure 9, it is found that the model showed the least deviation for a sphericity range of 0.47 to 0.68.

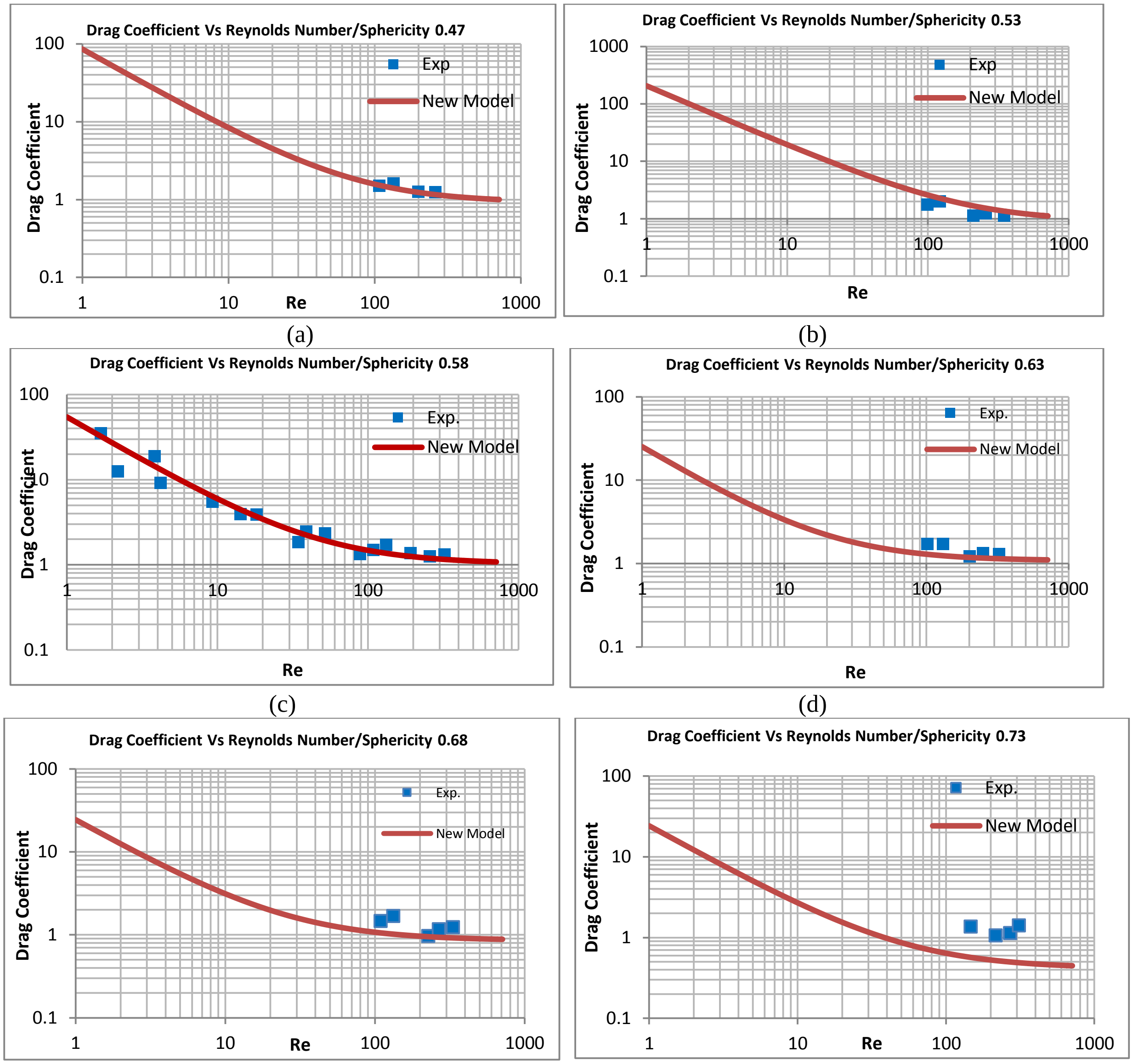

(a) (b) (c) (d) (e) (f)

Figure 9 Drag coefficient versus reynolds number for different sphericities

V. CONCLUSION

Using a shadowgraphy technique particle size and velocities were obtained from an operational fluidized bed. Velocity profiles from the fluidized bed were analyzed for both spherical and non-spherical particles at different superficial gas velocities above the particle minimum fluidization velocity. Future work includes attempts to predict particle behavior using data obtained from the second part (drag modeling) of the experiments.

The second part of the experiments involves the development of a drag model for non-spherical particles. The general expression of drag coefficient by Haider and Levenspiel was considered. Characteristic length (particle geometry) and Reynolds number were taken for particle nominal diameter and sphericity was measured as the ratio of nominal diameter and longest diameter of the particles. New developed drag expression is a function of Reynolds number and sphericity and it best suits for sphericity between 0.43 to 0.68.

ACKNOWLEDGMENTS

This research is supported by the U.S. Department of Energy, under award DE-FE0003742 (Project Manager Robie Lewis). However, any opinions, findings, conclusions, or recommendations expressed herein are those of the authors and do not necessarily reflect the views of the Department of Energy.

BIBLIOGRAPHY

[1] U.S. Department of Energy, Clean Coal Technologies-Coal Gasification R &D Website, URL: http://www.fossil.energy.gov/programs/powersystems/gasification/index.html.

[2] Sunmun L., Ativuth C., Kosol U., Yutaka T., Toshihiro K., Wiwut T., "Discrete Particle Simulation of Solids Motion in a Gas-Solid Fluidized Bed", Chemical Engineering Science, Vol. 58, Issue 6, 2003, pp. 915-921.

[3] Fariborz, T., Naoko E., and Clayton, W., “Experimental and Computational Study of Gas-Solid Fluidized Bed Hydrodynamics”, Chemical Engineering Science, Vol. 60, Issue 24, 2005, pp. 6857-6867.

[4] Berruti F., Kalogerakis N.,"Modelling the Internal Flow Structure of Circulating Fluidized Beds", the Canadian Journal of Chemical Engineering, Vol. 67, pp 1010-1014, 1989.

[5] Delgado S. S., Ibanez J. A. A., Verdugo A. S., Santana D., Rivas U. R.,"Coherent Structures and Bubble-Particle Velocity in 2-D Fluidized Bed" ISE Group, Thermal and Fluid Department, Universidad Carlos III de Madrid, Avda, de la, Spain.

[6] Lackermeier U., Rudnick C., Werther J., Bredebush A., Burkhardt H.,"Visualization of Flow Structures Inside a Circulating Fluidized Bed by Means of Laser Sheet and Image Processing" Powder Technology, Vol 114, Issues 1-3, PP 71-83, January 2001.

[7] Hatano H., Kido N.,"Microscope Visualization of solid particles in Circulating Fluidized Beds", Powder Technology, Vol 78, Issue 2, PP 115-119, February 1994.

[8] imenez F. H., Delgado S. S., Garcia A. G., Iborra A. A.,"Comparison Between Two-Fluid Model Simulations and Particle Image Analysis & Velocimetry (PIV) results for Two-Dimensional Gas-Solid Fluidized Bed" Chemical Eng. Science, Vol 66, PP 3753-3772, 2011.

[9] Laverman J.A.,Bulte M. J.T.,Annaland M.V.S.,Kuipers J.A.M,"Experimental and Computational Investigation on the Macroscopic Circulation Patterns in a Bubbling Gas-Solid Fluidzed Bed", 8th World Congress of Chemical Engineering, Aug 23-27,Montreal, Canada.

[10] Sathe M.J., Mathpati C.S., Deshpande S.S., Khan Z., Ekambara K., Joshi J.B.,"Investigation of Flow Structure and Transport Phenomena in Bubble Columns Using Particle Image Velocimetry and Miniature Pressure Sensors"Chem. Eng. Sci.,Vol.66,PP3087-3107,2011.

[11] Swamee P.K., Ojha C.S.P.,"Drag Coefficient and Fall Velocity of Nonspherical Particles", Journal of Hydraulic Engineering, Vol. 117, No.5, 1991.

[12] Khan A.R., Richardson J.F.,"The Resistance to Motion of a Solid Sphere in a Fluid", Chemical Engineering Comm., Vol 62, PP 135-150, 1987.

[13] Haider A., Levenspiel O.,"Drag Coefficient and Terminal Velocity of Spherical and Nonspherical Particles", Powder Technology, Vol. 58, PP 63-70, 1989.

[14] Syamlal M.,O'Brien T.J.,"Computer Simulation of Bubbles in Fluidized Bed", AIChE Symp. Series, Vol.85, PP-22-31, 1989.

[15] Gidaspow D., Bezburah R., Ding J.,"Hydrodynamics of Circulating Fluidized Beds, Kinetic Theory Approach in Fluidization VII, Proceedings of the 7th Engineering Foundation Conference on Fluidization, PP 75-82, 1992.

[16] Tran-Cong S.,Gay M.,Michaelides E.E.,"Drag Coefficients of Irregularly Shaped Particles", Powder Technology, Vol 139, pp 21-32, 2004.

[17] Mora C.F., Kwan A.K.H., Chan H.C.,"Particle Size Distribution Analysis of Coarse Aggregate Using Digita Image Processing" Elsevier Science Ltd, Cement and Concrete Research, Vol. 28, PP 921-932, 1998.

[18] Krumbien W.C.,"Measurement and Geological Significance of Shape and Roundness of Sedimentary Particles, Journal of Sedimentary Petrology, Vol. 11, PP 54-72, 1941.

[19] Wadell, Hakon,"Volume, Shape and Roundness of Rock Particles", Chicago: The Journal of Geology, Vol. 40, PP 443-451, 1932.

[20] Yang, Ching. W.,"Handbook of Fluidization and Fluid-Particle Systems", New York: Marcel Dekker, Inc. 2003, ISBN: 0-8247-0259-X.

[21] Chhabra R.P., Agarwal L., Sinha N.K.,"Drag on Non-Spherical Particles: An Evaluation of Available Methods", Powder Technology, Vol. 101, PP 288-295, 1999.

Appendix B: Fluent and MFIX code

The UDF code implemented in Fluent is shown below. The modified drag coefficient (fdrgs) is valid here for a sphericity of 0.9. Coefficients for particles of other sphericities can be found in reference6.

```
#include "udf.h"
#include "sg_mphase.h"
#define pi 4.*atan(1.)
#define diam2 3.e-4
DEFINE_EXCHANGE_PROPERTY(custom_drag_syam, cell, mix_thread, s_col, f_col)
{
 Thread *thread_g, *thread_s;
 real x_vel_g, x_vel_s, y_vel_g, y_vel_s, abs_v, slip_x, slip_y,
      rho_g, rho_s, mu_g, reyp, afac,
      bfac, void_g, vfac, fdrgs, taup, k_g_s;
 /* find the threads for the gas (primary) and solids (secondary phases).
These phases appear in columns 2 and 1 in the Interphase panel respectively*/
 thread_g = THREAD_SUB_THREAD(mix_thread, s_col);/*gas phase*/
 thread_s = THREAD_SUB_THREAD(mix_thread, f_col);/* solid phase*/
 /* find phase velocities and properties*/
 x_vel_g = C_U(cell, thread_g);
 y_vel_g = C_V(cell, thread_g);
 x_vel_s = C_U(cell, thread_s);
 y_vel_s = C_V(cell, thread_s);
 slip_x = x_vel_g - x_vel_s;
 slip_y = y_vel_g - y_vel_s;
 rho_g = C_R(cell, thread_g);
 rho_s = C_R(cell, thread_s);
 mu_g = C_MU_L(cell, thread_g);
 /*compute slip*/
 abs_v = sqrt(slip_x*slip_x + slip_y*slip_y);
 /*compute reynolds number*/
 reyp = rho_g*abs_v*diam2/mu_g;
 /* compute particle relaxation time */
 taup = rho_s*diam2*diam2/18./mu_g;
 void_g = C_VOF(cell, thread_g);/*gas vol frac*/
 /*compute drag and return drag coeff, k_g_s*/
 afac = pow(void_g,4.14);
 if(void_g<=0.85)
  bfac = 0.281632*pow(void_g, 1.28);
 else
  bfac = pow(void_g, 9.076960);
 vfac  = 0.5*(afac-0.06*reyp+sqrt(0.0036*reyp*reyp+0.12*reyp*(2.*bfac-afac)+afac*afac));
 fdrgs = ((void_g)*((24/reyp)*(1+(pow(4.63557417201694,-
33))*pow(reyp,0.03146))+(0.0000631424609190043/(1+(295401120441.391/reyp)))*(reyp/0.5)))/(24*(
pow(vfac,2)));
 k_g_s = (1.-void_g)*rho_s*fdrgs/taup;
 return k_g_s;
}
```

```
DEFINE_EXCHANGE_PROPERTY(custom_drag_ihme, cell, mix_thread, s_col, f_col)
{
 Thread *thread_g, *thread_s;
 real x_vel_g, x_vel_s, y_vel_g, y_vel_s, abs_v, slip_x, slip_y,
      rho_g, rho_s, mu_g, reyp, cd, eg,
      void_g, k_g_s;
 /* find the threads for the gas (primary) and solids (secondary phases).
These phases appear in columns 2 and 1 in the Interphase panel respectively*/
 thread_g = THREAD_SUB_THREAD(mix_thread, s_col);/*gas phase*/
 thread_s = THREAD_SUB_THREAD(mix_thread, f_col);/* solid phase*/

 /* find phase velocities and properties*/
 x_vel_g = C_U(cell, thread_g);
 y_vel_g = C_V(cell, thread_g);
 x_vel_s = C_U(cell, thread_s);
 y_vel_s = C_V(cell, thread_s);
 slip_x = x_vel_g - x_vel_s;
 slip_y = y_vel_g - y_vel_s;
 rho_g = C_R(cell, thread_g);
 rho_s = C_R(cell, thread_s);
 mu_g = C_MU_L(cell, thread_g);
 /*compute slip*/
 abs_v = sqrt(slip_x*slip_x + slip_y*slip_y);
 /*compute reynolds number*/
 reyp = rho_g*abs_v*diam2/mu_g;
 cd = (24./(reyp+SMALL)) + 5.48*pow((reyp+SMALL),-0.573) + 0.36;
 void_g = C_VOF(cell, thread_g);/*gas vol frac*/
 eg = pow(void_g,-2.65);
 k_g_s = (3./4.)*(cd*(1.-void_g)*abs_v*rho_g*eg)/diam2;
 return k_g_s;}
```

MFIX DAT File Example

```
#
# Fluidized Bed Simulation
#
# Mario A. Ruvalcaba 11-05-12
#
# Run time for F90 allocatable arrays on Octane -- 3.3 h
# Run-control section
#
RUN_NAME = 'Fluidized-Bed'
DESCRIPTION = 'Fluidized Bed Simulation'
RUN_TYPE = 'new'
UNITS = 'cgs'
TIME = 0.0 TSTOP = 1.0 DT = 1.0E-3 DT_MIN = 1.0E-12
NORM_G = 0.0d0 NORM_S = 0.0d0 MAX_NIT = 30
DISCRETIZE = 9*2
ENERGY_EQ = .FALSE.
```

```
SPECIES_EQ = .FALSE. .FALSE.
#
# Physical Parameters
#
UR_FAC(1) = 0.5
! Geometry Section
COORDINATES = 'cartesian'
XLENGTH = 12.0 !X length
IMAX = 160 !cells in i direction
YLENGTH = 50.0 !height
JMAX = 220 !cells in j direction
NO_K = .TRUE. !2D, no k direction
GRAVITY = 980
#
# Gas-phase Section
#
MU_g0 = 1.8E-4
MW_avg = 29.
#
# Solids-phase Section
#
DRAG_TYPE = 'SYAM_OBRIEN'
Drag_c1 = 0.26
Drag_d1 = 9.56872
RO_s = 2.23
D_p0 = 0.1
e = 0.8
Phi = 0.0
EP_star = 0.35
86
#
# Initial Conditions Section
#
! Bed Freeboard
IC_X_w = 0.0 0.0
IC_X_e = 12.0 12.0
IC_Y_s = 0.0 5.5
IC_Y_n = 5.5 50.0
IC_EP_g = 0.35 1.0
IC_U_g = 0.0 0.0
IC_V_g =@(45.8/0.45) 45.8
IC_U_s(1,1) = 0.0 0.0
IC_V_s(1,1) = 0.0 0.0
IC_P_star = 0.0 0.0
IC_T_g = 300.0 300.0
#
# Boundary Conditions Section
#
```

```
! Inlet Outlet
BC_X_w = 0.0 0.0
BC_X_e = 12.0 12.0
BC_Y_s = 0.0 50.0
BC_Y_n = 0.0 50.0
BC_TYPE = 'MI' 'PO'
BC_EP_g = 1.0
BC_U_g = 0.0
BC_V_g = 100.0
BC_P_g = 1.013E6 1.013E6
BC_T_g = 300.0
#
# Output Control
#
RES_DT = 0.01
!
! EP_g P_g U_g U_s ROP_s T_g X_g
! P_star V_g V_s T_s1 X_s Theta Scalar
! W_g W_s T_s2
SPX_DT = 0.01 0.1 0.1 0.1 100. 100. 100. 100.0 100.0
NLOG = 100
full_log = .true.
```

Appendix C: SciTech Article

Testing of a New Drag Relationship for Non-Spherical Particle Geometries Using the Two Fluid Model

A S M Raufur R Chowdhury[1], Md Rashedul H Sarker,[1] Norman Love[2], Ahsan Choudhuri[3]
Center for Space Exploration and Technology Research (cSETR)
University of Texas at El Paso, El Paso, Texas 79968

The present work presents the implementation of a newly developed drag model into computational code Fluent. The drag correlation previously developed is used to predict the behavior of a gas-solid packed bed computationally. For the comparison, bed pressure drop is plotted for different superficial velocities for three different particle sphericities 0.5, 0.65, and 0.9 and compared to experiments. The computational domain consisted of dimensions equal to the experimental setup. The experimental test facility was equipped with pressure, flow, and visualization measurement capabilities with dimensions of 12 cm diameter and 0.8m height. The newly developed drag model was implemented through the use of a user-defined-function in Fluent using the two-fluid model. Results showed that the maximum difference between computational and experimental values were 11.8% which is within experimental uncertainty. Hence implementation of this drag model may help researchers using the two-fluid model to more accurately predict hydrodynamic behaviors in a gas-solid packed bed.

Nomenclature

μ_g = Shear viscosity of fluid
μ_S = Shear viscosity of solid
$\emptyset$ = Sphericity
ρ_s = Phase volume fraction of solid
ρ_g = Phase volume fraction of fluid
a = Longest particle diameter
C_D = Drag coefficient
$C_{D,nonsph}$ = Drag coefficient equation for non-spherical particle
d = Nominal Diameter of non-spherical particles (mean sieve diameter)
F_D = Drag force
f = Drag function
Re_s = Reynolds number
v_t = Terminal velocity
v_s = Solids velocity
v_l = Fluid velocity

I. Introduction

Due to abundant resources of coal in the United States, the U.S. Department of Energy has emphasized the development of advanced coal gasifiers with enhanced efficiency and reliability[1]. One type of gasifier is a gas-solid packed bed which when fluidized involves multiple scales and interactions of phases which are difficult to measure in real-time[2]. To help resolve this issue computational methods have been developed to analyze these types of flows. Usually these types of flows are resolved using either the two fluid model or the discrete element method with the latter requiring significantly more computational power than the former. In either model there are many

---

[1] Graduate Research Assistant, Student Member AIAA
[2] Assistant Professor, Member AIAA
[3] Director cSETR and Professor, AIAA Associate Fellow

difficulties associated with predicting the behaviors of multiphase flows. Numerous investigations have been conducted to observe the importance of multiphase flow with their complicated flow structures[3]. For the two-fluid model, which requires less computational power to resolve the flowfield, the particle behaviors usually use specified particle drag models to estimate the momentum exchange between the fluid and solid phases. In many studies up until recently it has been convenient to model both spherical and non-spherical particles using spherical empirical and theoretical models. This assumption leads to some significant discrepancies between computational and experimental results.

Since in most practical applications the particles used are non-spherical it is more accurate to express the governing equations taking into account the particle shape. Consideration of sphericity, the roundness of a three dimensional object, in drag model is necessary to accurately predict the behavior of the gas-solid bed. Some other authors have studied similar flows such as Sau et al.[4] which determined that the total pressure drop increases with the increase of superficial gas velocity. Escudero et al.[5] proposed that the minimum fluidization velocity is influenced by the changes in particle density. Authors have also developed different correlations based on particle shape[6] such as studies by Khan and Richardson[8], Haider and Levenspiel[9], Syamlal and O'Brien[10] and Gadaspow et al[11].

In this paper the authors have used a similar approach to those in previous studies[8-11]. However, in the present investigation the presentation of the drag relationship for non-spherical particles is accompanied by results after implementing the new drag relationship into a computational code Fluent two-fluid model. This type of approach is not seen in literature. Results presented here include the pressure drop vs. superficial velocity curves compared with the experimental results.

II. Experimental Methodology

A. Gas-Solid Experimental Setup

Figure 1 shows a laboratory scale packed fluidized bed with its basic components. The bed is comprised of a quartz tube with a 12 cm outer and 0.5 cm wall thickness. Air is used as the gas introduced to fluidized bed fed through a 12.7 cm diameter sheet metal pipe from a 3730 kW blower with a maximum 34 m^3/min flow rate. A butterfly valve is used to control flow rate which was measured with a thermal mass flow meter. For uniform distribution of air to the bed a honeycomb shape distributor with 2.54 cm in length was placed 8 cm below the bed. To hold the particles in the bed a mesh made from brass screen with a 53 µm nominal diameter was installed. This same type of mesh catch was installed at the top of the bed. For pressure measurements a digital manometer capable of measuring up to 13.8 kPa was connected to a tygon tube inserted into a small port at the bottom of the packed section, readings from this device were taken at 0.1 Hz.

Borosilicate glass beads with density 2230 kg/m^3 were selected for the non-spherical test particles, Geldart Group B and D. To produce non-spherical particles, a hydraulic press, Fig. 2a, was used to crush 6mm particles into smaller pieces. The crushed particles contained different sized particles ranging from a few microns to 6mm nominal diameter. To categorize these crushed particles a sieve shaker, Fig. 2b, was used with different sieve sizes ranging from 500-1180 µm.

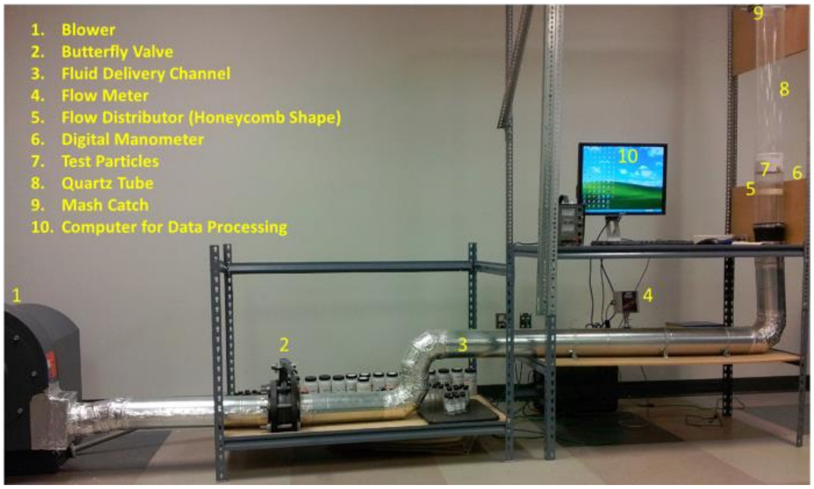

Figure 1: Laboratory scale gas-solid fluidized bed

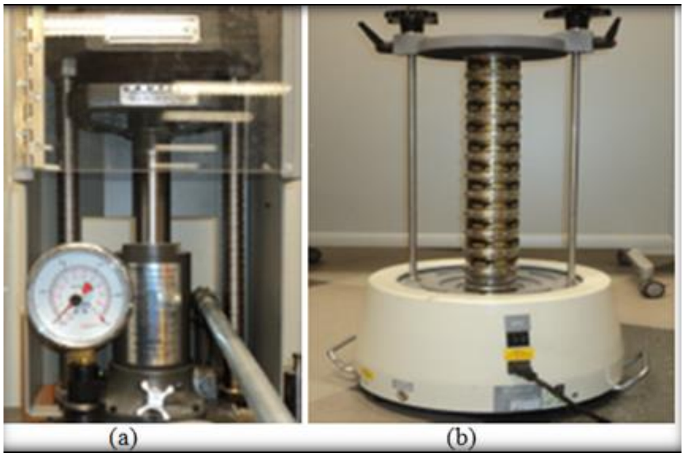

Figure 2: a) Hydraulic press (b) Sieve shaker

B. Particle Shape Categorization

After particle characterization was done using the sieve shaker a DinoLite microscope camera was used to measure the dimensions of each particle used in the gas-solid bed. Using these dimensions the particles were then categorized according to their sphericity defined by Wadell[13] and shown in Eq. (1):

$$\emptyset = \sqrt[3]{\frac{Volume\ of\ Particle}{Volume\ of\ the\ Circumscribe\ Sphere}} \tag{1}$$

C. Drag Model Experimental Setup and Previous Results

The drag correlation obtained and used in the computational model was from a setup that measured velocities for single and multiple free falling particles. Particles were dropped from the top of the column and allowed to free-fall through air at ambient conditions. The terminal velocity of each particle was estimated based on particle surface area and velocity measurement taken at a distance of 1.5 times below the calculated location to ensure that terminal velocity was reached. Each particle velocity measurement was taken with a high-speed camera, set at a rate of 2000 frames per second, and Dantec Dynamics Shadow Sizing software. For these experiments the camera was oriented opposite to a backlit light source and synchronized through a timer box. More information on this setup can be found in Reference [6]. Using data for each particle, a drag coefficient could be determined for each particle shape and size from the relationship given in Eq. (2):

$$C_D = \frac{F_D}{\frac{1}{2}\rho_g A V_t^2} \tag{2}$$

Where F_D is the drag force which is assumed to be equal to the difference between the weight and buoyant force acting on the particle at the terminal velocity, A is the particle area, and V_t is the terminal velocity.

The newly developed drag model, Eq. (3), was then implemented through a user-defined function (UDF) in Fluent. In Eq. (3) the drag coefficient of the particles is expressed in terms of sphericity and Reynolds number. This equation is valid for sphericities between 0.5 to 0.9 and Reynolds numbers from 1 to 1000.

$$C_{D,nonsph} = \frac{24}{Re_s}\left[1 + \exp[-142.7123 + 555.6297\emptyset - 533.0938\emptyset^2]Re_s^{(0.2004\emptyset - 0.1489)}\right] + \frac{\exp(47.3143 - 258.3263\emptyset + 464.829\emptyset^2 - 275.72369\emptyset^3)}{1 + \frac{\exp(-161.8 + 855.9\emptyset - 1502\emptyset^2 + 870.4\emptyset^3)}{Re_s}} \tag{3}$$

III. Computational Model

A. Model Assumptions

In order to simplify the complexities involved in the solution process the following assumptions are made. For the two-fluid model, an Eulerian-Eulerian approach was taken, the fluid and the solid phase are both considered as a fluid for the simulation. For the Fluent simulation the viscosity of the solid was assumed as 1.7894e-05.

Governing Equations

The fluid-solid momentum equations and constitutive components are presented in Eqs. (4-7)[3]:

$$\begin{aligned}\frac{\partial}{\partial t}(\alpha_s\rho_s\vec{v}_s) + \nabla.(\alpha_s\rho_s\vec{v}_s\vec{v}_s) \\ = -\alpha_s \nabla p - \nabla p_s + \nabla.\bar{\bar{\tau}}_s + \alpha_s\rho_s\vec{g} + \sum_{l=1}^{n}\big((\vec{v}_l - \vec{v}_s)\big) + \dot{m}_{ls}\vec{v}_{ls} - \dot{m}_{sl}\vec{v}_{sl} \\ + \big(\vec{F}_s + \vec{F}_{lift,s} + \vec{F}_{vm,s}\big) \\ + K_{sl}\end{aligned} \tag{4}$$

Fluid-solid exchange coefficient is given as:

$$K_{sl} = \frac{\alpha_s\rho_s f}{\tau_s} \tag{5}$$

Where, f is a drag function and defined differently for the different exchange-coefficient models.

The particulate relaxation time is:

$$\tau_s = \frac{\rho_s {d_s}^2}{18\,\mu_l} \tag{6}$$

In the present paper the variable f was taken as shown below in Eq. (7). This equation was then modified to incorporate the variation of C_D using Eq. (3) for non-spherical particles.

$$f = \frac{C_D Re_s \alpha_l}{24\, {v_{r,s}}^2} \tag{7}$$

B. Computational Domain

The mesh for the bed was generated using ANSYS Workbench 13.0 and had the same dimensions of the actual bed. Since most of the computational area of interest is located near the bottom of the domain; the height of the grid was modified to be 0.5 m instead of 0.8 m. Figure 3 is the schematic of the fluidized bed reactor and Fig. 4 is the 2D geometry of the reactor with the mesh. Figure 5 shows a zoomed section of the bottom of the mesh. The left and right side of the bed was considered the wall, the bottom was the velocity inlet and the top is the pressure outlet. The top is considered pressure outlet.

Table 1: Boundary Conditions

Bottom	Velocity inlet
Left side	Wall
Right side	Wall
Top	Pressure outlet

Table 2: Configuration of the Computational Domain

Particle diameter	1 mm
Glass beads density	2300 kg/m^3
Air density	1.225 kg/m^3
Air viscosity	1.7894e-05
Bed height	0.05 m
Bed diameter	0.127 m

The simulations were used to compare the computational results with the experimental work. This simulation is done using commercial software package ANSYS Fluent 13.0 with the Eulerian multiphase model. Standard k-ε viscous model is used with disperse turbulence multiphase model. Existing drag models are used and the drag model developed from the experiment is used for different sphericities to compare the results. The coefficient of restitutions used is 0.81. The phase-coupled SIMPLE algorithm, which is an extension of SIMPLE algorithm to multiphase flows, is applied for the pressure velocity coupling[14]. Time step size is set to 0.001 s and maximum number of iterations per time steps is 2000.

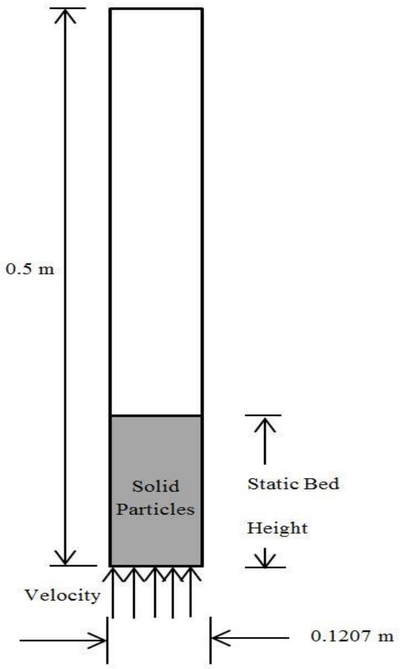

Figure 3: 2D geometry of the bed

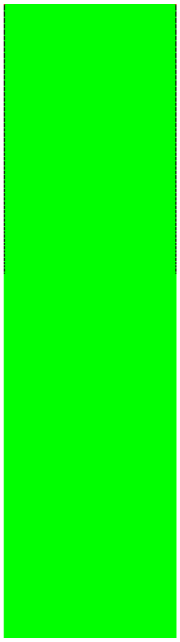

Figure 4: Mesh of the 2D bed

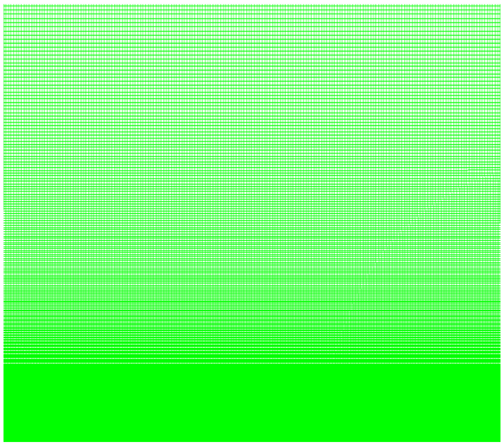

Figure 5: Zoomed section of the mesh

IV. Results and Discussion

A. Computational Results

Computational results found from the simulation are used to compare with the experimental results. In the experiment pressure drop is measured 2 cm above the bed height. The static bed height considered for the results were for those with 5 cm height. The simulation was run in 2D and found that the global physics behavior of a 2D and 3D simulation were very similar[15]. The following sections compare the experiment and the computational results to determine the accuracy of the computational fluid dynamics model predictions. The simulations were run for the drag model developed from the experiment using three different sphericities.

Figures 6 to 8 show the results of the pressure drop vs. superficial velocity using the drag model developed from the experimental results using sphericities of 0.50, 0.65 and 0.90, respectively. Overall, when the drag model was implemented into Fluent, a good agreement between the calculated and experimental results was obtained.

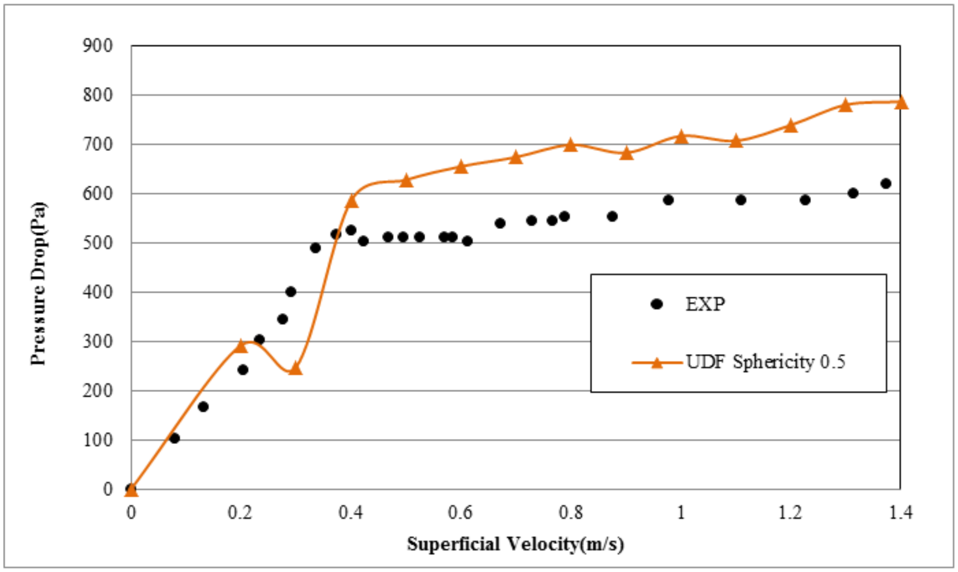

Figure 6: Pressure drop vs. superficial velocity using newly developed model with sphericity 0.50

Table 3: Percent deviation in pressure drop at minimum fluidization using the new drag model

Sphericity (-)	Computational Result (Pa)	Experimental Results (Pa)	Percent of Deviation from the Experimental Results
0.50	585.95	523.99	11.82%
0.65	583.69	523.99	11.39%
0.90	575.10	523.99	9.75%

From Table 3 we can see that the percent of deviation for the new drag relationship to experimental values. The newly developed drag model provides considerably good results within predicted experimental uncertainties. This suggests that the newly developed drag model can help to improve predictions using the two-fluid model in Fluent when operating using particle sphericities between 0.5 and 0.9.

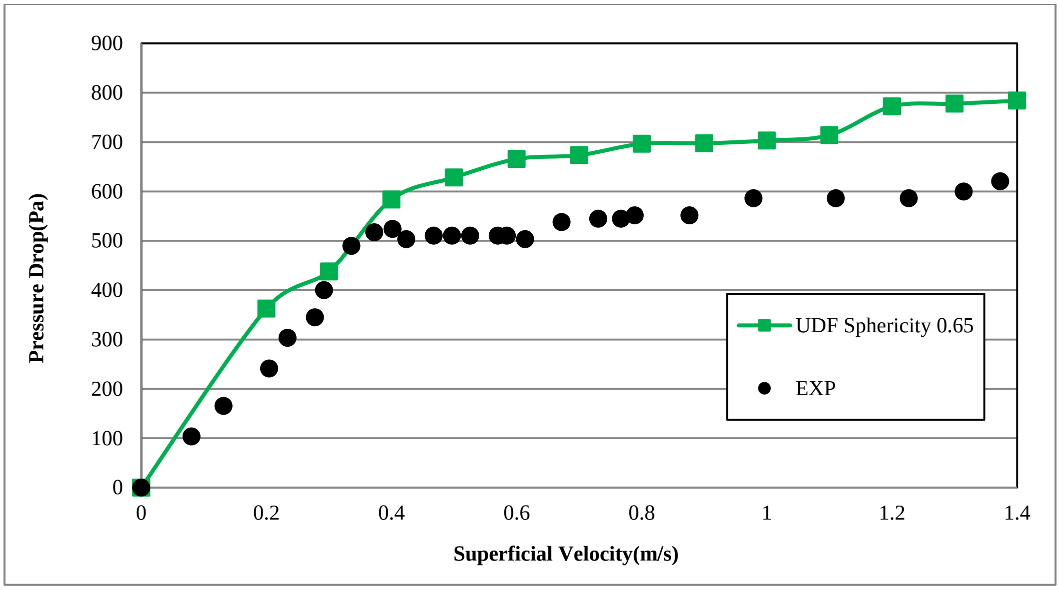

Figure 7: Pressure drop vs. superficial velocity using newly developed model with sphericity 0.65

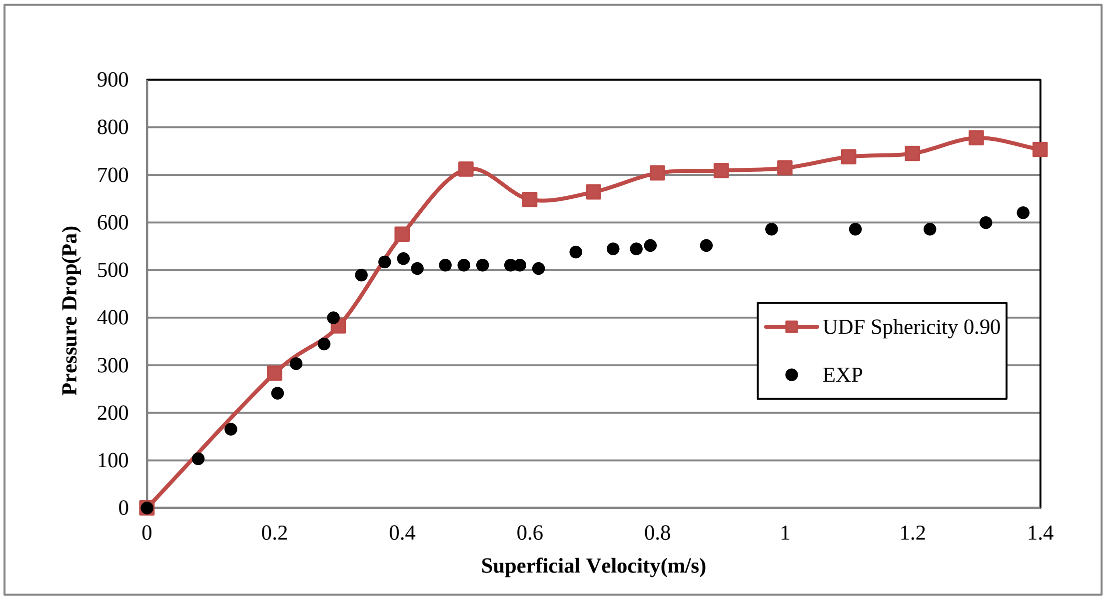

Figure 8: Pressure drop vs. superficial velocity using newly developed drag model with sphericity 0.90

V. Summary and Conclusion

A newly developed drag model was tested for the non-spherical particles in Fluent. The drag model modified the drag coefficient used to calculate the gas-solid momentum transfer coefficient and is based on the particle geometry and Reynolds number, further details of the model can be found in [6]. The drag relationship was implemented through a user defined function in ANSYS Fluent 13.0 and results compared to experimental data. Results show that the drag model when implemented in Fluent to predict pressure drop results within experimental uncertainties which may allow users who do not have access to computationally expensive models to implement this drag correlation and obtain accurate results.

Appendix

The UDF code implemented is shown below. The modified drag coefficient (fdrgs) is valid here for a sphericity of 0.9. Coefficients for particles of other sphericities can be found in reference[6].

```
#include "udf.h"
#include "sg_mphase.h"
#define pi 4.*atan(1.)
#define diam2 3.e-4
DEFINE_EXCHANGE_PROPERTY(custom_drag_syam, cell, mix_thread, s_col, f_col)
{
 Thread *thread_g, *thread_s;
 real x_vel_g, x_vel_s, y_vel_g, y_vel_s, abs_v, slip_x, slip_y,
      rho_g, rho_s, mu_g, reyp, afac,
      bfac, void_g, vfac, fdrgs, taup, k_g_s;
 /* find the threads for the gas (primary) and solids (secondary phases).
These phases appear in columns 2 and 1 in the Interphase panel respectively*/
 thread_g = THREAD_SUB_THREAD(mix_thread, s_col);/*gas phase*/
 thread_s = THREAD_SUB_THREAD(mix_thread, f_col);/* solid phase*/
 /* find phase velocities and properties*/
 x_vel_g = C_U(cell, thread_g);
 y_vel_g = C_V(cell, thread_g);
 x_vel_s = C_U(cell, thread_s);
 y_vel_s = C_V(cell, thread_s);
 slip_x = x_vel_g - x_vel_s;
 slip_y = y_vel_g - y_vel_s;
 rho_g = C_R(cell, thread_g);
 rho_s = C_R(cell, thread_s);
 mu_g = C_MU_L(cell, thread_g);
 /*compute slip*/
 abs_v = sqrt(slip_x*slip_x + slip_y*slip_y);
 /*compute reynolds number*/
 reyp = rho_g*abs_v*diam2/mu_g;
 /* compute particle relaxation time */
 taup = rho_s*diam2*diam2/18./mu_g;
 void_g = C_VOF(cell, thread_g);/*gas vol frac*/
 /*compute drag and return drag coeff, k_g_s*/
 afac = pow(void_g,4.14);
 if(void_g<=0.85)
  bfac = 0.281632*pow(void_g, 1.28);
 else
  bfac = pow(void_g, 9.076960);
 vfac  = 0.5*(afac-0.06*reyp+sqrt(0.0036*reyp*reyp+0.12*reyp*(2.*bfac-afac)+afac*afac));
 fdrgs = ((void_g)*((24/reyp)*(1+(pow(4.63557417201694,-
33))*pow(reyp,0.03146))+(0.0000631424609190043/(1+(295401120441.391/reyp)))*(reyp/0.5)))/
(24*(pow(vfac,2)));
 k_g_s = (1.-void_g)*rho_s*fdrgs/taup;
 return k_g_s;
}
DEFINE_EXCHANGE_PROPERTY(custom_drag_ihme, cell, mix_thread, s_col, f_col)
{
 Thread *thread_g, *thread_s;
 real x_vel_g, x_vel_s, y_vel_g, y_vel_s, abs_v, slip_x, slip_y,
      rho_g, rho_s, mu_g, reyp, cd, eg,
      void_g, k_g_s;
 /* find the threads for the gas (primary) and solids (secondary phases).
These phases appear in columns 2 and 1 in the Interphase panel respectively*/
 thread_g = THREAD_SUB_THREAD(mix_thread, s_col);/*gas phase*/
```

```
thread_s = THREAD_SUB_THREAD(mix_thread, f_col);/* solid phase*/

/* find phase velocities and properties*/
x_vel_g = C_U(cell, thread_g);
y_vel_g = C_V(cell, thread_g);
x_vel_s = C_U(cell, thread_s);
y_vel_s = C_V(cell, thread_s);
slip_x = x_vel_g - x_vel_s;
slip_y = y_vel_g - y_vel_s;
rho_g = C_R(cell, thread_g);
rho_s = C_R(cell, thread_s);
mu_g = C_MU_L(cell, thread_g);
/*compute slip*/
abs_v = sqrt(slip_x*slip_x + slip_y*slip_y);
/*compute reynolds number*/
reyp = rho_g*abs_v*diam2/mu_g;
cd = (24./(reyp+SMALL)) + 5.48*pow((reyp+SMALL),-0.573) + 0.36;
void_g = C_VOF(cell, thread_g);/*gas vol frac*/
eg = pow(void_g,-2.65);
k_g_s = (3./4.)*(cd*(1.-void_g)*abs_v*rho_g*eg)/diam2;
return k_g_s;}
```

Acknowledgments

This research is supported by the U.S. Department of Energy, under awards DE-FE-0003742 (Project Manager Robie Lewis). However, any opinions, findings, conclusions, or recommendations expressed herein are those of the authors and do not necessarily reflect the views of the Department of Energy. The authors would also like to acknowledge the work of Mr. Christian Rodarte and Mr. Salvador Sandoval for their assistance in the project.

References

[1]U.S. Department of Energy, Clean Coal Technologies-Coal Gasification R &D Website, URL: http://www.fossil.energy.gov/programs/powersystems/gasification/index.html.

[2]Sunmun L., Ativuth C., Kosol U., Yutaka T., Toshihiro K., and Wiwut T., "Discrete Particle Simulation of Solids Motion in a Gas-Solid Fluidized Bed", Chemical Engineering Science, Vol. 58, Issue 6, 2003, pp. 915-921.

[3]Berruti F., and Kalogerakis N.,"Modelling the Internal Flow Structure of Circulating Fluidized Beds", Canadian Journal of Chemical Engineering, Vol. 67, 1989, pp 1010-1014,.

[4]Sau, D.C., Mohanty, S., and Biswal, K., “Minimum Fluidization Velocities and Maximum Bed Pressure Drops for Gas–Solid Tapered Fluidized Beds” Chemical Engineering, Vol. 132, 2007, pp. 151-157.

[5]Escudero, D., and Heindel, T., "Bed Height and Material Density Effects on Minimum Fluidization Velocity in a Cylindrical Fluidized Bed", 7th International Conference on Multiphase Flow, Tampa, FL, USA, May 30- June 4, 2010.

[6]Sarker, Md, Chowdhury, R., Love, N., and Choudhuri, A., “Flow Field Visualization and Drag Analysis of Particles in a Gas-Solid Fluidized Bed Using a Non-Intrusive Optical Technique” American Institute of Aeronautics and Astronautics Aerospace Science Meeting, Dallas, Texas, January 7-10, 2013.

[7]Swamee, P.K., and Ojha C.S.P.,"Drag Coefficient and Fall Velocity of Nonspherical Particles", Journal of Hydraulic Engineering, Vol. 117, No.5, 1991, pp. 660-667.

[8] Khan A.R., and Richardson J.F.,"The Resistance to Motion of a Solid Sphere in a Fluid", Chemical Engineering Comm., Vol 62, 1987, pp. 135-150.

[9]Haider A., and Levenspiel O.,"Drag Coefficient and Terminal Velocity of Spherical and Nonspherical Particles", Powder Technology, Vol. 58, 1989, pp. 63-70.

[10]Syamlal M., and O'Brien T.J.,"Computer Simulation of Bubbles in Fluidized Bed", AIChE Symp. Series, Vol.85, 1989, pp. 22-31.

[11]Gidaspow D., Bezburah R., and Ding J.,"Hydrodynamics of Circulating Fluidized Beds, Kinetic Theory Approach in Fluidization”, Proceedings of the 7th Engineering Foundation Conference on Fluidization, 1992, pp. 75-82.

[12] Mora C.F., Kwan A.K.H., and Chan H.C.,"Particle Size Distribution Analysis of Coarse Aggregate Using Digital Image Processing" Cement and Concrete Research, Vol. 28, 1998, pp. 921-932.

[13] Wadell, H.,"Volume, Shape and Roundness of Rock Particles", Journal of Geology, Vol. 40, 1932, pp. 443-451.

[14] Taghipour, F., Ellis, N., and Wong, C., "Experimental and Computational Study of Gas-Solid Fluidized Bed Hydrodynamics", Chemical Engineering Science, Vol. 60, 2005, pp. 6857-6867.

[15] Hulme, I., Clavelle, E., and Lee, L., "CFD Modeling and Validation of Bubble Properties for a Bubbling Fluidized Bed", Industrial and Chemical Engineering Research, Vol. 44, 2005, pp. 4254-4254.